

May 2018

# Characterizing the Geochemical Changes Across a Strain Gradient in the Beja-Acebuches Metabasites Due to Retrograde Metamorphism and Fluid Flow Along the Southern Iberian Shear Zone

Sheryl Stephenson

*University of Wisconsin-Milwaukee*

Follow this and additional works at: <https://dc.uwm.edu/etd>

 Part of the [Geology Commons](#)

---

## Recommended Citation

Stephenson, Sheryl, "Characterizing the Geochemical Changes Across a Strain Gradient in the Beja-Acebuches Metabasites Due to Retrograde Metamorphism and Fluid Flow Along the Southern Iberian Shear Zone" (2018). *Theses and Dissertations*. 1926.  
<https://dc.uwm.edu/etd/1926>

This Thesis is brought to you for free and open access by UWM Digital Commons. It has been accepted for inclusion in Theses and Dissertations by an authorized administrator of UWM Digital Commons. For more information, please contact [open-access@uwm.edu](mailto:open-access@uwm.edu).

CHARACTERIZING THE GEOCHEMICAL CHANGES ACROSS A  
STRAIN GRADIENT IN THE BEJA-ACEBUCHES METABASITES  
DUE TO RETROGRADE METAMORPHISM AND FLUID FLOW  
ALONG THE SOUTHERN IBERIAN SHEAR ZONE

by

Sheryl Isabella Stephenson

A Thesis Submitted in  
Partial Fulfillment of the  
Requirements for the Degree of  
Master of Science  
in Geosciences

at

The University of Wisconsin-Milwaukee

May 2018

# CHARACTERIZING THE GEOCHEMICAL CHANGES ACROSS A STRAIN GRADIENT IN THE BEJA-ACEBUCHES METABASITES DUE TO RETROGRADE METAMORPHISM AND FLUID FLOW ALONG THE SOUTHERN IBERIAN SHEAR ZONE

by

Sheryl Isabella Stephenson

University of Wisconsin-Milwaukee, 2018  
Under Supervision of Dr. Dyanna Czeck

The Southern Iberian Shear Zone (SISZ), SW Spain, provides an ideal location to study the effects of syntectonic fluid on rock chemistry, deformation, and metamorphism. The SISZ is a 60km long, 300-500m wide shear zone, striking 115 and dipping approximately 50 degrees to the NNE, that follows the contact between metamorphosed MORB-derived Acebuches metabasites (AB) of the Ossa-Morena zone and the metamorphosed Pulo do Lobo (PdL) accretionary prism. Both units underwent two deformational events: 1) a HT/LP event that reached amphibolite facies and significantly dehydrated the rocks, and 2) a retrograde metamorphic event from amphibolite-greenschist facies that required the addition of H<sub>2</sub>O. Major element geochemical characterization of the AB was

undertaken using x-ray fluorescence to enable a better understanding of fluid-rock interaction. These geochemical data from the shear zone indicate enrichments in  $K_2O$ ,  $CaO$ , and  $Al_2O_3$  with a depletion in  $SiO_2$ . Element vs distance from shear zone plots demonstrate that the movement of  $CaO$ ,  $Al_2O_3$ , and  $SiO_2$  is related to the retrograde metamorphic event because the enrichments ( $CaO$ ,  $Al_2O_3$ ) and depletion ( $SiO_2$ ) is greater with increasing retrograde metamorphism. However, sporadic and variable  $K_2O$  enrichment is documented throughout the shear zone, even in lithologies furthest from the shear zone. The movement of  $CaO$ ,  $Al_2O_3$ , and  $SiO_2$  within the lithologies closest to the shear zone support the Conduit-Barrier Fluid Flow model for parallel fluid flow. The sporadic enrichment of  $K_2O$  in samples away from the shear zone suggests that fluid migrated outward in localized pathways through brittle fractures.

## TABLES OF CONTENTS

List of Figures.....	vi
List of Tables .....	ix
Acknowledgements .....	x
Introduction.....	1
Objective .....	1
Fluid-rock interaction in shear zones .....	1
Geologic Background .....	10
Methods.....	22
Field methods .....	22
Geochemical methods .....	29
Results .....	35
Geochemistry vs. distance from the top of the structure .....	35
Isocon analysis .....	56
Discussion .....	76
Evaluating isocon methods.....	76
Elemental trends.....	80

Data limitations .....	87
Major element changes and metamorphic reactions, structural fabrics, and distance from shear zone.....	89
Fluid composition .....	91
Fluid pathways .....	92
Conclusion .....	96
References .....	100
Appendices .....	107
A. XRF data for transect 1 .....	108
B. XRF data for transect 2 .....	109
C. XRF data for transect 3 .....	110
D. XRF data for transect 5 .....	111
E. XRF data for transect 6 .....	111
F. XRF data for transect 8 .....	112

## LIST OF FIGURES

Figure	Page No.
1. Map depicting the Southern Iberian Shear Zone, formed by the contact between the South Portuguese Zone (SPZ) and the Ossa Morena Zone (OMZ) during the collision between Laurentia-Baltica and Gondwana .....	11
2. Map of the central portion of the Southern Iberian Shear zone with contact between Acebuches Metabasites and Pulo do Lobo Terrane.....	13
3. Map showing the extent of Southern Iberian Shear zone between the towns of Aroche and Aracena .....	14
4. The four rock domains of the Acebuches Metabasites .....	21
5. Relative position of the sampled transects across the length of the shear zone .....	23
6. Google earth image of each transect and the sample locations .....	26
7. Element vs Distance from top of structure for Transect 1	
a. SiO <sub>2</sub> , Al <sub>2</sub> O <sub>3</sub> , Na <sub>2</sub> O, CaO .....	38
b. MgO, Fe <sub>2</sub> O <sub>3</sub> , MnO, TiO <sub>2</sub> .....	39
c. K <sub>2</sub> O, P <sub>2</sub> O <sub>5</sub> , color key .....	40
8. Element vs Distance from top of structure for Transect 2	
a. SiO <sub>2</sub> , Al <sub>2</sub> O <sub>3</sub> , Na <sub>2</sub> O, CaO .....	41
b. MgO, Fe <sub>2</sub> O <sub>3</sub> , MnO, TiO <sub>2</sub> .....	42
c. K <sub>2</sub> O, P <sub>2</sub> O <sub>5</sub> , color key .....	43
9. Element vs Distance from top of structure for Transect 3	

a.	SiO <sub>2</sub> , Al <sub>2</sub> O <sub>3</sub> , Na <sub>2</sub> O, CaO .....	44
b.	MgO, Fe <sub>2</sub> O <sub>3</sub> , MnO, TiO <sub>2</sub> .....	45
c.	K <sub>2</sub> O, P <sub>2</sub> O <sub>5</sub> , color key .....	46
10.Element vs Distance from top of structure for Transect 5		
a.	SiO <sub>2</sub> , Al <sub>2</sub> O <sub>3</sub> , Na <sub>2</sub> O, CaO .....	47
b.	MgO, Fe <sub>2</sub> O <sub>3</sub> , MnO, TiO <sub>2</sub> .....	48
c.	K <sub>2</sub> O, P <sub>2</sub> O <sub>5</sub> , color key .....	49
11.Element vs Distance from top of structure for Transect 6		
a.	SiO <sub>2</sub> , Al <sub>2</sub> O <sub>3</sub> , Na <sub>2</sub> O, CaO .....	50
b.	MgO, Fe <sub>2</sub> O <sub>3</sub> , MnO, TiO <sub>2</sub> .....	51
c.	K <sub>2</sub> O, P <sub>2</sub> O <sub>5</sub> , color key .....	52
12.Element vs Distance from top of structure for Transect 8		
a.	SiO <sub>2</sub> , Al <sub>2</sub> O <sub>3</sub> , Na <sub>2</sub> O, CaO .....	53
b.	MgO, Fe <sub>2</sub> O <sub>3</sub> , MnO, TiO <sub>2</sub> .....	54
c.	K <sub>2</sub> O, P <sub>2</sub> O <sub>5</sub> , color key .....	55
13. Variation in protolith geochemistry across each transect; variation in K <sub>2</sub> O (top), SiO <sub>2</sub> (middle), TiO <sub>2</sub> , (bottom) .....		
		62
14. Isocon plots for transect 1; method 1 (top), method 2 (middle) and method 3 (bottom) .....		
		70
15. Isocon plots for transect 2; method 1 (top), method 2 (middle) and method 3 (bottom) .....		
		71
16. Isocon plots for transect 3; method 1 (top), method 2 (middle) and method 3 (bottom) .....		
		72

17.Isocon plots for transect 5; method 1 (top), method 2 (middle) and method 3 (bottom) .....	73
18.Isocon plots for transect 6; method 1 (top), method 2 (middle) and method 3 (bottom) .....	74
19.Isocon plots for transect 8; method 1 (top), method 2 (middle) and method 3 (bottom) .....	75
20. Conduit-Barrier Fluid Flow model .....	94

## LIST OF TABLES

Tables	Page No.
1. Summary table for the results of isocon method 1; Enrichments/depletions of elements across the length of the shear zone .....	59
2. Summary table for the results of isocon method 2; Enrichments/depletions of elements across the length of the shear zone .....	65
3. Average protolith compositions before and after standard deviation correction .....	67
4. Summary table for the results of isocon method 3; Enrichments/depletions of elements across the length of the shear zone .....	69
5. Geochemistry data tables for all samples across transects 1,2,3, 5,6, and 8 .....	107

## ACKNOWLEDGMENTS

First and foremost, I would like to thank my thesis advisor, Dr. Dyanna Czeck, for the endless support and dedication with regards to both the analysis and writing aspects of my project. Dyanna's patience and non-judgmental nature allowed me to approach her for help without hesitation. Dyanna's dedication to her students' understanding and growth is commendable. She offers a balance of constructive criticism and encouragement, which made me feel continuously pushed and challenged, yet capable and confident. Finally, Dyanna's help in the field and funding for our field work does not go unnoticed. I would also like to give thanks to Carlos Fernandez and Manuel Diaz-Azpiroz for their guidance and hospitality in the field, as well as their contribution of figures and supplemental direction when needed. Carlos and Manuel's previous publications and vast knowledge of the field area aided my research project tremendously. Throughout my research project they were always available even through communication and time-zone barriers and offered invaluable input. I would like to thank Nancy Duque and Dulce Hernandez Blanchard for dedicating their time and effort to help with sample preparation. Finally, I want to express my deepest gratitude to my parents who were an unremitting source of support and encouragement during my Master's work and will remain so indefinitely.

Field work was funded by a University of Wisconsin-Milwaukee RACAS grant to Dyanna Czeck. The geochemical analysis portion of this project was made possible by the Geological Society of America Graduate Research Award.

# 1. INTRODUCTION

## *1.1 Objective of research*

This research will test the hypothesis that the retrograde metamorphism in the Southern Iberian Shear Zone (SISZ) was accompanied by fluid interaction that resulted in geochemical alteration, strain softening, and enhanced deformation localization. By testing this hypothesis, we aim to better understand how syn-deformational water may affect geochemistry, metamorphism, and microstructure within shear zones.

## *1.2 Fluid-rock interaction in shear zones*

Fluid-rock interaction and the subsequent effects on rock chemistry, deformation, and metamorphism have been studied extensively (Carter et al. 1990, Newman and Mitra, Kisters et al. 2000, Yonkee et al. 2013). Fluid can accumulate within the crust from a variety of sources. The changing temperature and pressure along with continuous and discontinuous reactions within metamorphic belts, release volatile-bearing fluids into the surrounding rocks. Due to the instability of porosity structures within deforming rocks, compaction of porous, fluid-containing media will drive expulsion of fluids into the surrounding rocks. Finally, high-temperature metamorphism promotes dehydration reactions, which extract water from the on-going reactions and release it into surrounding rocks (Holness, 1997,

Carter et al., 1990). The rocks do not have the ability to maintain this water and it is quickly dispersed within the system. The water is dispersed by a variety of flow-mechanisms, such as thermal convection, advection (infiltration), and surface and intracrystalline diffusion. The distance of flow varies from grain scale to hundreds of kilometers (Carter et al., 1990).

When this fluid interacts with surrounding rocks, it has significant effects on deformation mechanisms and thus affects deformation processes such as folding, faulting, and shear-development. It also exerts partial control on rock strength, deformation heterogeneity, and strain localization (Carter et al., 1990). Rock strength can be altered in one of two ways; 1) chemical change via mineral reactions along fluid pathways and 2) mechanical change via fluid pressure and associated stress (Cox, 2002). Therefore, fluid-rock interaction can affect whether rock accommodates stress by brittle or ductile deformation (e.g. Wawrzyniec et al., 1999). If the fluid pressure rapidly exceeds rock strength, the rock will undergo brittle deformation and fracture, which plays a large role in faulting (Axen et al., 2001). Conversely, fluid-rock interaction can promote ductility within high-strain zones. Two of the critical mechanisms during deformation are: 1) movement of dislocations, which is grain size dependent and, 2) diffusion across grain boundaries, which is inversely proportional to the cube of the grain size (Beach, 1980). Due to this relationship between grain size and deformation mechanisms,

the initial stages of deformation may be dominated by dislocation mechanisms, which eventually produces smaller sub-grains or recrystallized grains, which in turn favors diffusion mechanisms over dislocation.

The relationship between deformation and metamorphism within shear zones is closely related and can be demonstrated in the fact that shear zones typically show a metamorphism that is not recorded in the undeformed rocks outside of the shear boundary (Beach, 1980). Many authors have studied this observation and recognized that certain metamorphic fabrics, associated textures, and assemblages were confined to shear zones (Ramsay and Graham 1970, Beach 1976).

During metamorphic reactions, mineral solution, nucleation, and growth occur. Metamorphic products typically exhibit grain-size reduction with unbound and disorganized grain boundaries, which promote grain boundary diffusion mechanisms and subsequent fast strain rates during the initial reaction stage. As minerals grow and the reactions cease, deformation by dislocation will dominate and often overprint earlier diffusion-dominated mechanism (White and Knipe, 1978).

Water is a common feature within many shear zones (Kerrich et al., 1980, McCaig, 1984, Knipe and Wintsch 1985, Sinha et al., 1986, O'Hara 1988,

Silverstone et al., 1991, Marquer et al., 1994), and water is responsible for promoting many retrograde metamorphic reactions that enhance the grain-size reduction and subsequent diffusion mechanisms. In this sense, fluid-rock interaction and the subsequent effects on metamorphism can be seen as a catalyst for strain-softening and enhancement of ductility within shear zones. It can also promote dislocation glide by phyllosilicate production (Sinha et al., 1986, Wintsch et al., 1995). This strain-softening plays a large role in folding mechanisms of rocks and the development of shear zones (Wintsch and Yi, 2002).

The positive feedback between deformation, fluid, and metamorphism also promotes strain localization (Carter et al. 1990, Barnes et al., 2004). Although deformation heterogeneity is largely a function of rock heterogeneity and contrasting rheologies, fluids can also affect deformation heterogeneity by promoting strain localization. Abnormal pore pressure caused by fluid infiltration and dynamic recrystallization during deformation often leads to an increase in rock permeability and porosity, which in turn creates favorable pathways for fluid flow. Alternatively if fluid pressure exceeds rock strength it will result in brittle fractures, which are also considered favorable pathways for flow (Axen et al., 2001). As more water passes through these favorable paths, it may chemically alter the rocks due to element mobility, which can control metamorphic reactions. Metamorphic effects, such as grain size reduction and production of weaker,

schistose minerals, create zones of weakness that can more easily accommodate strain compared to surrounding rock (White et al., 1980). For example, in Mg-rich mafic rocks, in shallow meteoric H<sub>2</sub>O-dominated environments, it is typical for weaker phyllosilicates, such as chlorite or biotite, to replace stronger framework and chain silicates. With increasing phyllosilicate content and the subsequent preferred orientation, these areas of phyllosilicate-replacements are weaker than the feldspar-rich protolith (Wintsch et al. 1995, O'Hara, 1988). Phyllosilicates that are shortened at 45° to (001) are orders of magnitude weaker than quartz and feldspars (Kronenberg et al., 1990). When these phyllosilicates are aligned, they can deform by dislocation glide even at low temperature and pressure (Wintsch et al., 1995).

There are two end-member systems considered when it comes to fluid-rock interaction in magnesium-rich rocks; water-dominated and rock-dominated (Wintsch et al. 1995). Water-dominated systems are shallow (<15km) and the fluid/rock ratio is high. This high fluid/rock ratio means that there is more fluid present relative to the reacting rock and therefore the fluid composition remains unchanged by the interaction. It is in these systems that muscovite mica is expected to precipitate. Rock-dominated systems are deeper (~10-15km) and the fluid/rock ratio is low. Consequently in rock-dominated systems the chemistry of the fluid is

affected by the rock with which it interacts. In these systems chlorite (<11km) or biotite (>10km) may precipitate. Chlorite replacement may lead to volume loss and a subsequent increase in porosity with reaction progress. This weakening of rocks due to phyllosilicate replacement is more significant in Mg-rich rocks than Mg-poor rocks and for this reason, strain softening is more likely to occur in mafic rocks (Wintsch et al. 1995).

When a fluid interacts with a rock under solid conditions and changes it chemically, it is termed “metasomatism.” The definition of metasomatism according to the IUGS Subcommittee on the Systematics of Metamorphic Rocks (SSMR), is a “metamorphic process by which the chemical composition of a rock or a rock portion is altered in a pervasive manner and which involves the introduction and/or removal of chemical components as a result of the interaction of the rock with aqueous fluids (solutions). During metasomatism the rock remains in a solid state.” There are two types of metasomatism, 1) modal or patient metasomatism, which involves the introduction of new minerals and 2) cryptic metasomatism, which describes compositional changes of pre-existing minerals without the formation of new phases (Harlov and Austerheim, 2013). The process occurs when a fluid migrates into a host rock and creates a state of chemical disequilibrium, prompting re-equilibrium reactions to occur (Harlov and Austerheim, 2013). These re-equilibrium reactions cannot occur without the

transport of chemical elements. Fluids are the catalysts for these reactions, by dissolving and transporting these elements either by removing mobile elements from the rock, or introducing mobile elements from elsewhere. These changes are typically identified by unusual enrichments of certain elements that are not naturally found in the rock or enrichment of immobile elements (e.g.  $\text{TiO}_2$ ) due to the depletion of mobile elements (e.g.  $\text{SiO}_2$ ).

Although fluid is abundant within the lithosphere (Carter et al. 1990) and massive fluid transport is thought to occur in collisional boundaries (Fyfe and Kerrich, 1985), its transient nature makes it impractical to study its effects directly in the mid-low crust. Therefore fluid is best studied through evidence of ancient fluid flow such as geochemical/structural indicators including certain metamorphic reactions (Wintsch and Yi, 2002) and alignment of minerals to form fabrics (Ault and Selverstone, 2008), both of which weaken the rock through strain softening. Geochemical indicators in the rock may remain after fluid flow, such as depletion of mobile element and enrichment of immobile elements. Such studies are common (Kerrich et al., 1980, McCaig, 1984, Knipe and Wintsch 1985, Sinha et al., 1986, O'Hara 1988, Selverstone et al., 1991, Newman and Mitra, 1993, Marquer et al., 1994), however, they are typically performed in granitic complexes or metasedimentary rocks where the starting chemistry is often heterogeneous.

Shear zones are particularly important when studying fluid-rock interaction because the increased permeability relative to wall rocks, related to shear fabric development, provides favorable large-scale channels for flow through the crust (Holness, 1997). Fluid flow through shear zones is thought to be an important part of the crustal fluid-flow budget (Fyfe et al., 1978). Axen et al. (2001) argue that the ductile-to-brittle transition of two shear zones was a function of fluid-pressure and associated strain rather than a function of temperature and pressure.

Understanding shear zone dynamics and the effects of fluid-rock interaction is important for a variety of reasons. Since fluids can greatly alter the strength and deformation character of rocks, they exert control on the location of the brittle-ductile transition and therefore exert partial control over crustal strength, earthquake nucleation, orogenesis, and continental dynamics (Axen et al. 2001). In addition, understanding fluid-rock interaction during deformation proves invaluable in the exploration industry. Shear zones have been associated with significant fluid-related mineral deposits (Gater, 1991, Kolb et al. 2004, Micklethwaite et al. 2010) and may provide insight into the conditions preferable for mineral deposition. For example, gold-bearing quartz veins often occur in steeply dipping shear zones (Sibson, 1988). Additionally, abrupt drops in fluid pressure caused by shear failure within faults, which can be caused by fluid-

interaction, is also thought to play an important role in gold-bearing quartz vein deposition (Sibson, 1988).

This research will study the fluid-rock interaction along one prominent shear zone, the Southern Iberian Shear Zone in southwest Spain. This ancient shear zone is well-exposed and provides an ideal natural setting to study the effects of fluid interaction during shear zone deformation. The shear zone separates two units, the Acebuches Metabasites (AB) and the Pulo do Lobo metasedimentary rocks (PdL). This research focuses primarily on the AB because: 1) the SISZ has a wider effect on the AB compared to the PdL, and 2) the relatively simple starting geochemistry will make identifying alteration easier than in more heterogeneous rocks (Yonkee et al., 2013). The AB metabasites were the main reason the SISZ was chosen for this research, however, other factors include: well exposed transects across the shear zone strain gradient, previous evidence for fluid in retrograde reactions (actinolite alteration to chlorite), and well-understood kinematics (Díaz-Azpiroz and Fernández, 2005, Díaz-Azpiroz et al., 2006, Fernández et al., 2013).

## **2. GEOLOGIC BACKGROUND**

During the Carboniferous period, about 300 million years ago, the majority of Iberia was assembled during the tectonic collision between the Laurentia-Baltica and Gondwana continents. During this collision a solo microplate, now known as the South Portuguese zone, collided and attached to the edge of Gondwana, now known as the Ossa-Morena zone, forming the Variscan Iberian Massif (Crespo-Blanc and Orozco, 1988). The suture between these two terranes, the Ossa-Morena Zone and the South Portuguese zone, is the Aracena metamorphic belt (fig. 1).

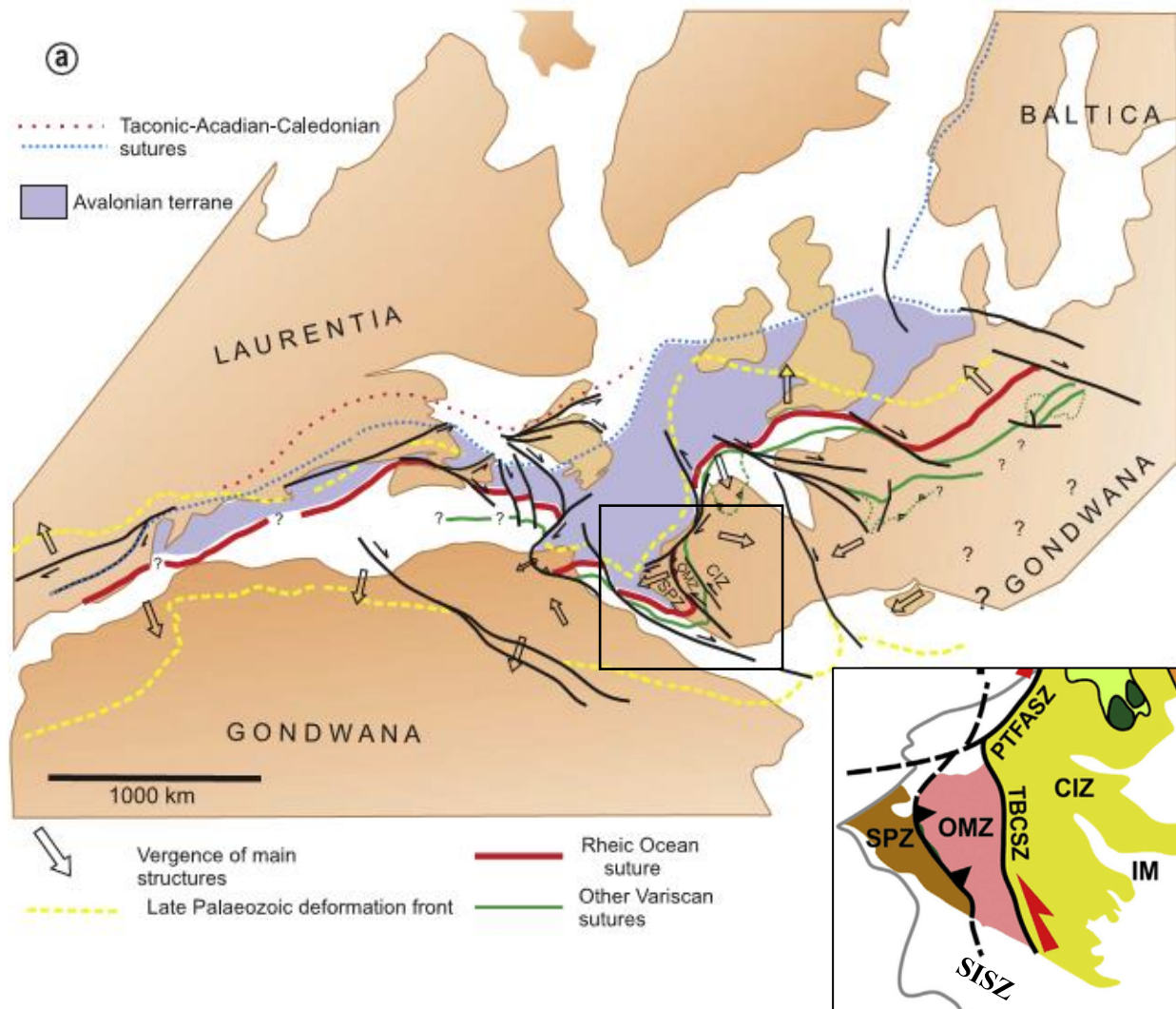
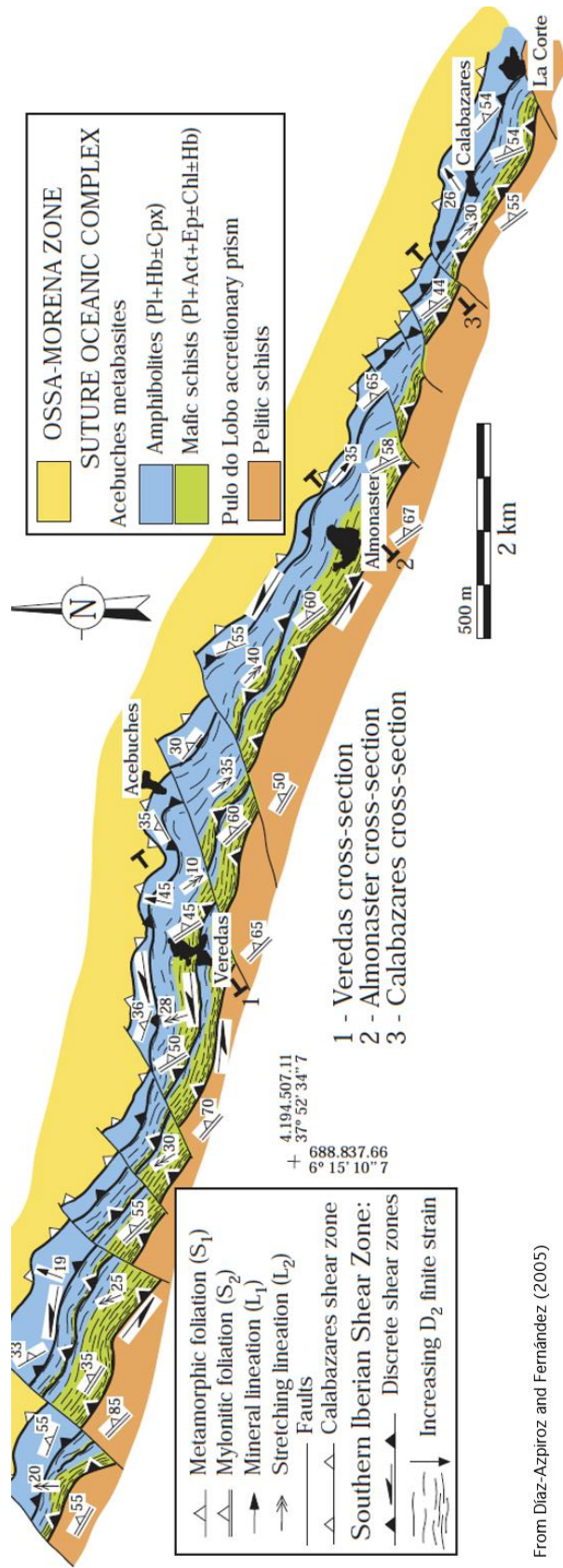


Figure 1. Ancient collision between Laurentia-Baltica and Gondwana created the Variscan Belt of Western Europe. The area of study is the Southern Iberian Shear Zone (SISZ), which forms the contact between the South Portuguese Zone (SPZ) and the "Para-autochthonous and allochthonous units" of the Ossa Morena Zone (OMZ). From Azor et al., 2008, Dias et al., 2016 (inset).

This metamorphic belt, which stretches 100 km long and is tens of kilometers wide, is separated into two domains: 1) a continental domain to the north, which primarily contains high-grade pelitic gneisses and calc-silicate rocks and 2) an oceanic domain to the south (Castro et al., 1999). This research focusses

on the southern oceanic domain, which can be further subdivided into two groups of rocks that are separated by the Southern Iberian Shear Zone (SISZ).

The SISZ follows the contact between metamorphosed MORB-derived (Bard and Moine, 1979) Acebuches metabasites (AB) of the Ossa-Morena zone to the north and schists of the metamorphosed Pulo do Lobo (PdL) accretionary prism to the south, part of the South Portuguese Zone (Castro et al., 1999, fig. 2). The shear contact extends at least 60 km in length between the Spanish towns of Aracena and Aroche and is 300-500 m wide (fig 3).



From Díaz-Azpiroz and Fernández (2005)

Figure 2. Map of the central portion of the SISZ showing the Acebuches Metabasites (amphibolites and mafic schists) in shear contact with the Pulo do Lobo terrane (pelitic schists). Transect lines 1-3 are shown. From Díaz-Azpiroz and Fernández, 2005.

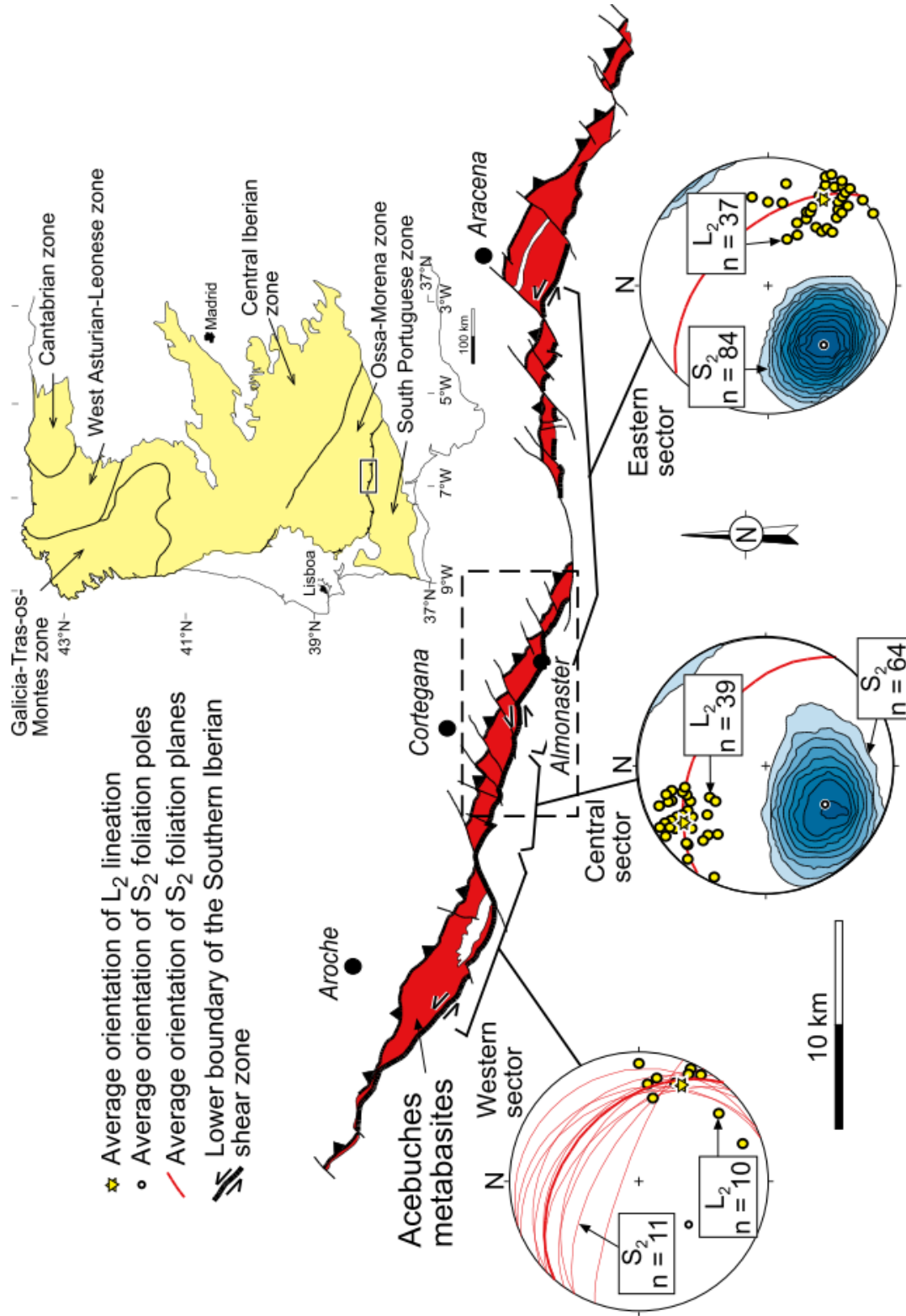


Figure 3. Transects T1-T8 and structural data from the SISZ. The location of Fig. 1 is shown by the outlined box. From Fernandez et al., 2013.

Shear fabrics extend broadly into the Acebuches metabasites and only locally affect the schists of the Pulo Do Lobo domain (Díaz-Azpiroz and Fernández, 2005). Both the AB and PdL underwent two deformational events; first a high temperature, low pressure (HT/LP) event related to collision in the AB (Castro et al., 1996) while the PdL underwent low-grade metamorphism and folding (Onezime et al., 2002) and second a retrograde metamorphic event. The first HT/LP metamorphic event (M1), related to the Variscan orogeny, reached the transition between amphibolite/granulite facies. Within the AB, M1 is characterized by the development of two, NW-SE sub-parallel foliations with a steep NE dip defined by the orientation of amphibole crystals. These rocks also developed a metamorphic, grain-size banding of alternating plagioclase and amphibole-rich layers. Lineation shows a high rake/pitch with a NE-E plunge and is composed of a preferred orientation of long axes of amphibole prisms. The metamorphic grade increases toward the top of the structure, evident by an increase in metamorphic banding and the introduction of clinopyroxene (Díaz-Azpiroz and Fernández, 2005). The rocks affected by D1 only can be separated into two domains: coarse-grained banded amphibolites containing clinopyroxene at the top of the unit and medium grained amphibolites without clinopyroxenes below. The following paragraph discusses the mineral assemblages and uses these abbreviations: Plagioclase (Pl), hornblende (Hbl), Clinopyroxene (Cpx), Titanite

(Ttn), ilmenite (Ilm), magnetite (Mgt), apatite (Ap), quartz (Qtz), edenite-pargasite (Ed-Prg), chlorite (Chl), epidote (Ep), actinolite (Act), albite (Ab), and calcite (Cal). The assemblages of these two domains are characterized by Diaz-Azpiroz (2000) as follows:

1) Coarse-grained (2 mm) banded amphibolites with clinopyroxene (highest grade) (Banded cpx)

a. Pl + Hbl + Cpx + Ttn + Ilm + Mgt ± Ap

b. Pl + Hbl + Qtz + Ttn + Ilm + Mgt ± Ap (rare quartz-rich lithology)

2) Medium grained (1-2 mm) banded amphibolites without clinopyroxene:

(Banded w/o cpx)

a. Pl + Hbl + Ttn ± Ilm ± Mgt ± Ap

b. Pl + Hbl + Qtz + Ttn ± Ilm ± Mgt ± Ap (rare quartz-rich lithology)

Diaz-Azpiroz (2000) studied the minerals via microprobe and determined the following detailed mineralogy. The plagioclase in the upper banded amphibolite domain (with cpx) is characterized by Andesine-labradorite (An30-An60). Lower in the structural column, the banded amphibolites without clinopyroxene become more sodic and are characterized by Oligoclase-Andesine (An20-An40). The amphiboles in both of these domains are dominated by

magnesiohornblendes in which a combination of edenite and pargasite substitution dominates, in addition to Ti-tschermakite substitution by introducing Ti from the consumption of titanite in these upper levels of the banded amphibolites. Titanite within the banded amphibolites with cpx is included within magnetite and ilmenite or forms a reaction rim around them. The composition of the titanite remains relatively constant throughout all domains.

The structural top (north) of the Achebuches metabasites preserved this D1/M1 metamorphism while the base (south) of the metabasites underwent the second deformation event, related to the thrusting of the metabasites onto the Pulo do Lobo terrane and subsequent development of the SISZ, the focus of this research. This second deformation event (D2) produced amphibolite-greenschist retrograde metamorphism (M2). Diaz-Azpiroz (2000) described the following mineralogy in the two units that were affected by both D1 and D2.

1) Sheared amphibolites (<1mm) (SA)



2) Mafic schists (MCS) (<0.5mm)



Díaz-Azpiroz (2000) studied the phases using microprobe and determined the following detailed mineralogy. The plagioclase in these D2-affected domains ranges between An 15-An 45. There is often some zonation with an andesine nucleus (An37-An41) and oligoclase border (An17-An32). Albite (An3-An7) appears in the structurally lowest part of the MCS. There are also labradorite-bytownite (An62-An80) crystals in the MCS domain, which are interpreted to most likely be relicts from D1-deformation or igneous relicts. The amphiboles within these domains are much more heterogeneous and actinolite, hornblende, edenite, pargasite, and hastingsite coexist. Here, the most important substitution is pargasite, which is accompanied by minor edenite, tschermakite, Fe- and Ti-tschermakite substitutions. All of these amphiboles, except actinolite, are relicts of D1. Chlorite and epidote also appear together in these D2-affected domains, with chlorite confined to the MCS domain. Both chlorite and epidote show no real variation in composition. Díaz-Azpiroz (2000) suggests that the Mg # (mean=0.64) of chlorite corresponds to a composition between clinocllore and chamosite. Epidote, which appears in both D2 domains but is more abundant in the MCS, occurs within pressure shadows of porphyroclasts or is concentrated within epidote-rich bands. The epidote is determined to belong to the clinozoisite-epidote series, with a high proportion of the Pistacite molecule (Ps65-Ps98). The titanite in the SA and MCS appears together with magnetite, which forms “trains” that follow

foliation. The composition remains constant as determined by a 0.86-1.13 Ti/Ca ratio. Al does not replace  $\text{Fe}^{3+}$  in the tetrahedral sites. Díaz-Azpiroz (2000) also documents very sporadic K-feldspar grains throughout D2 rocks.

D2 also produced mylonitic shear fabrics oriented  $115^\circ$  and dipping  $50^\circ$  to the NNE (D2) (Castro et al., 1996, Díaz-Azpiroz and Fernández, 2005, Fernández et al., 2013). The stretching lineation (L2), evident from plagioclase ribbons, fluctuates from a SE plunge in the east and west to a NW plunge in the center of the shear zone and is always oblique relative to the strong strike orientation of the shear zone (Díaz-Azpiroz and Fernández, 2005)

The boundary of this D2 deformation is represented by the folding of the D1 banded amphibolites without clinopyroxene. These folds eventually become so tight and isoclinal that the rocks grade into sheared amphibolites (pl-hbl assemblages). At the shear contact, the rocks are chlorite-rich mafic schists. The retrograde M1 is marked with actinolite, epidote and chlorite assemblages as well as pl-hbl near the base of the AB and the SISZ contact.

Díaz-Azpiroz and Fernández (2005) characterize the SISZ as having a listric shape with several shear zones deviating from a main basal shear zone, evident by shear anastomosing of mafic schists around amphibolite lenses. Based on these varying L2 stretching lineations that juxtapose a stable WNW-ESE strike, Díaz-

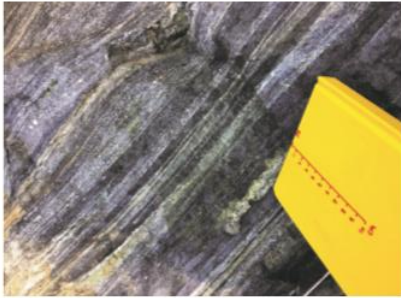
Azpiroz and Fernández (2005) interpret that the SISZ was formed via triclinic transpression with oblique extrusion (further modeled by Fernández et al., 2013).

The four rock domains analyzed in this research, starting from the top of the metabasites structure are: 1) coarse-grained banded amphibolites containing clinopyroxene, 2) medium-grained banded amphibolites without clinopyroxene, 3) folded and eventually sheared amphibolites, and finally 4) mafic chlorite schists. (Castro et al., 1996; Díaz-Azpiroz and Fernández, 2005) (fig. 4).

Coarse-grained banded amphibolites with pyroxene



Medium-grained banded amphibolites without pyroxene



Folded amphibolites representing outer shear boundary



Sheared amphibolites (folds become attenuated and obscured)



Mafic chlorite schists



Shear contact

Preserves D1, M1

Retrograde metamorphism

Figure 4. The four rock domains from top of structure (left) toward the shear contact (right). Folded amphibolites are included here to show the outer boundary of the shear zone.

### 3. METHODS

#### *3.1 Field methods*

Fieldwork and subsequent data collection took place starting in January 2017. Six transects (1,2,3,5,6,8 corresponding with numbering used by Díaz-Azpiroz and Fernández, 2005) within the AB between Aracena and Aroche were densely sampled across the strain gradient, starting from outside the shear boundary through the shear contact and slightly into the PdL (fig. 5).

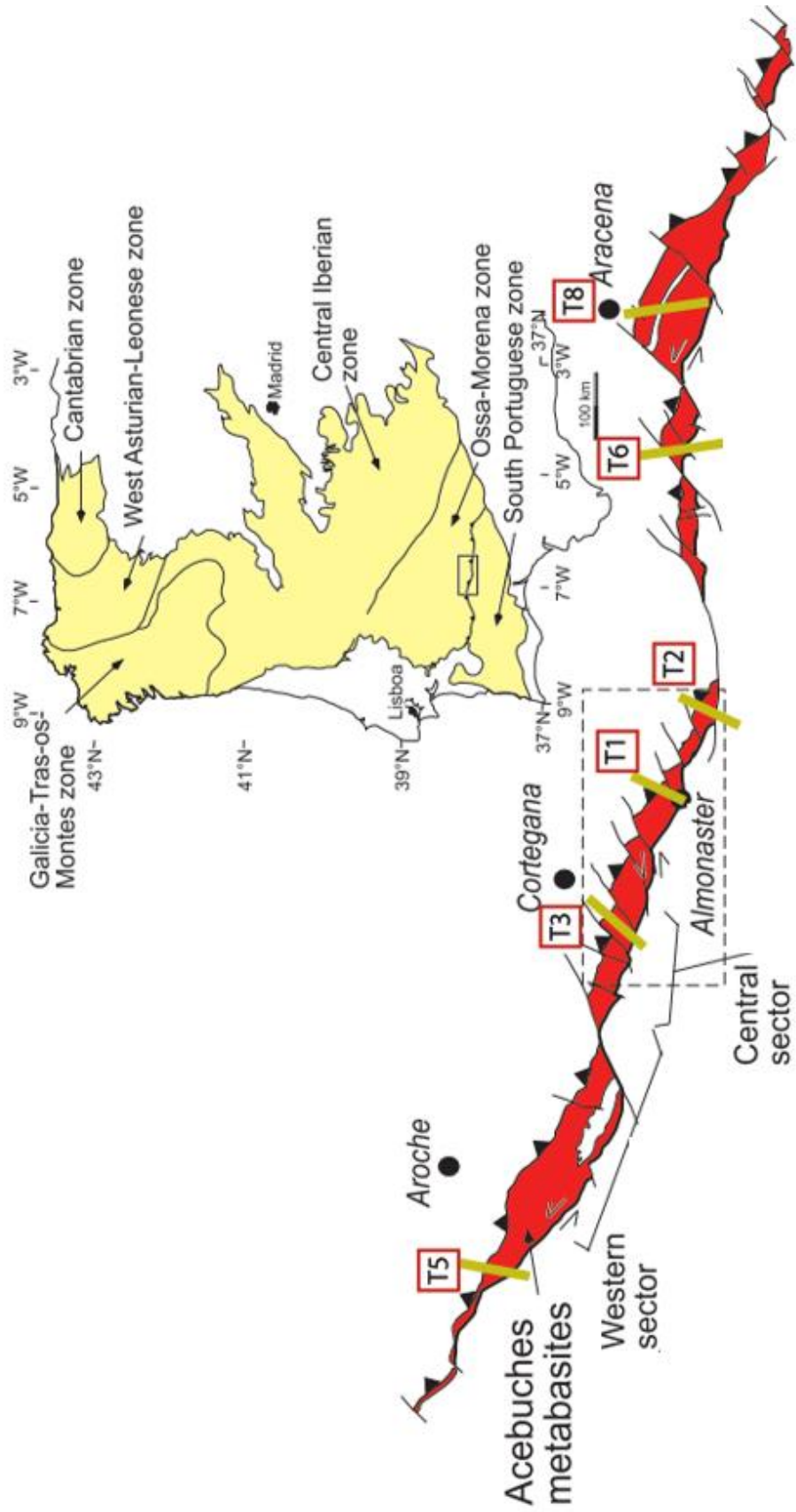


Figure 5. Shows the relative location of each sampled transect, with numbering corresponding to those used by Díaz-Azpiroz and Fernández, 2005. Figure is adapted from Fernández et al., 2013.

Most of the samples were collected along public roadways where the outcrops were large and relatively fresh, and the most continuous sections of AB could be found (fig. 6). All samples and outcrops were located using a map and a hand-held GPS.

The number of samples collected across the six transects totals to 92, 78 from the MB, and the remaining 14 from the PdL. Breakdown of sample collection is as follows: Transect 1: 16 MB, 6 PdL, Transect 2: 21 MB, 4 PdL, Transect 3: 17 MB, 1 PdL, Transect 5: 4 MB, 1 PdL, Transect 6: 7 MB, 2 PdL, Transect 8: 13 MB, 0 PdL. The metabasites were sampled across the four rock domains discussed previously. The PdL samples, not discussed further here, will be analyzed by other members of our research team. At each location, we collected two separate samples: one for this geochemical study and another for a complimentary microstructural study to be completed by other members of the research group.

When possible, the top of the structure was identified by locating calc-silicate rocks, belonging to the northern continental domain (Castro et al., 1996). The first metabasite outcrop below these calc-silicate rocks was sampled as our top of structure and this lithology was the first of four rock domains; coarse-grained, banded amphibolites containing clinopyroxene. When calc-silicate rocks were not available for reference, top of structure was deemed as the uppermost outcrop matching rock domain 1. A reduction in grain size and a loss of clinopyroxene

marks rock domain 2; medium-grained, banded amphibolites without clinopyroxene. These top two domains are apparently unaffected by the D2 retrograde metamorphism and are simply collected as the “unaltered samples” for geochemical comparison. Towards the shear zone, these medium-grained amphibolites become folded, which marks the outermost boundary of the shear zone and subsequently leads into rock domain three; sheared amphibolites (pl-hbl assemblages). Rock domain 4 is found nearest to the shear zone contact and consists of chlorite mafic schist, which is identified by the alteration of actinolite to chlorite. Pinpointing the transitions between these rock domains relied on availability of outcrop.

At each outcrop, orientations of foliation and lineation (when present) were measured and the associated strength of each was noted (strong vs weak). Where folds were present in the rocks, trend and plunge of the hinge were measured. Structural information was noted to identify rock domains, such as identification of folds for locating the outer boundary of the shear zone, but the geochemically-dominated nature of this project meant that our focus was on sample collection within rock domains. Much of the structural data was previously collected by our field companions Diaz-Azpiroz and Fernandez (Diaz-Azpiroz and Fernandez, 2005, Diaz-Azpiroz et al., 2006, Diaz-Azpiroz et al., 2007).

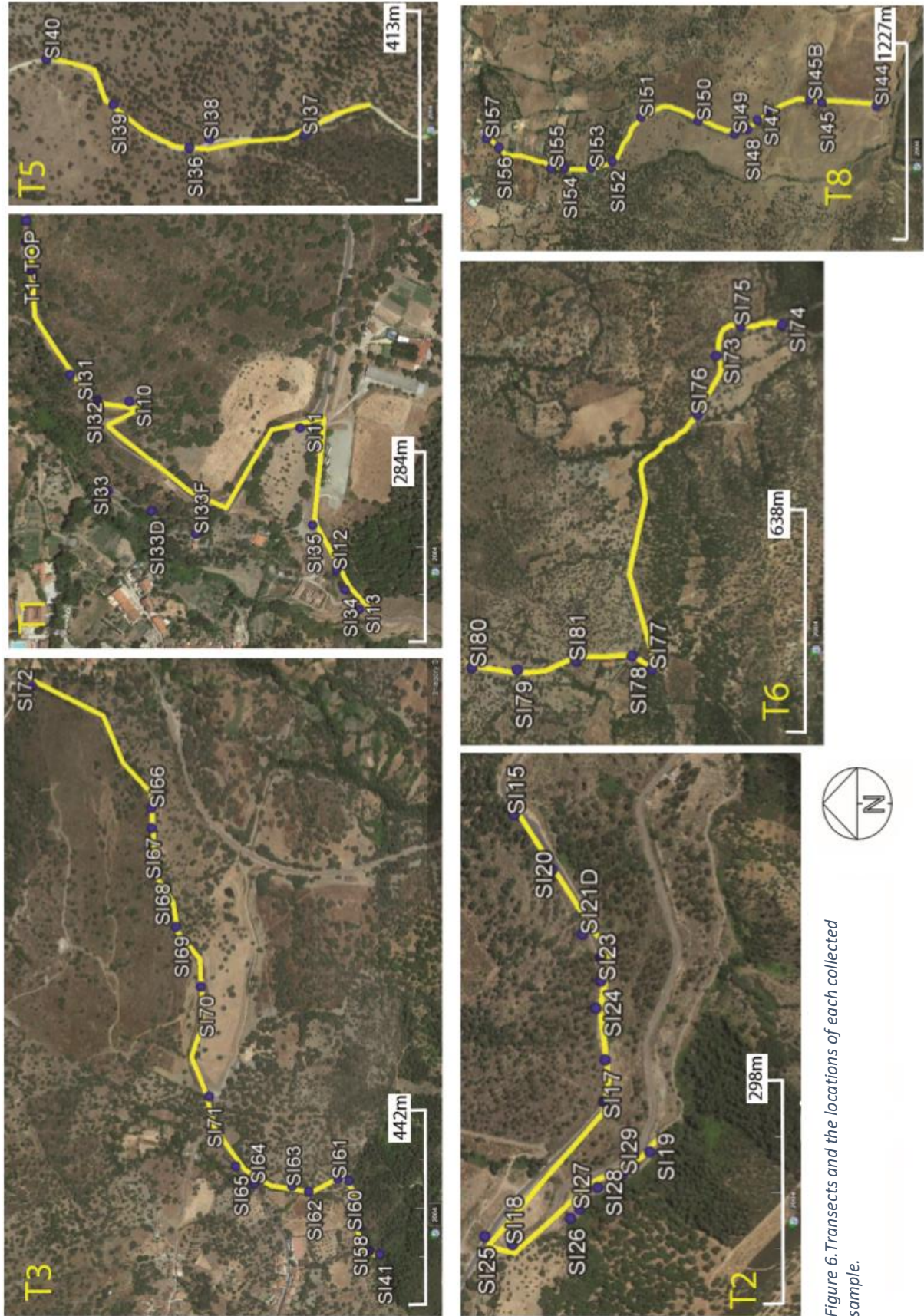


Figure 6. Transects and the locations of each collected sample.

Sampling was conducted primarily along roadways that cut across structure, but normally the roads are not perpendicular to structural layering. Therefore, a series of calculations were performed to transform roadside distance ( $D_m$ ) to the distance ( $D$ ) from the structural top of the metabasites (AB). Starting from the structural top of the series, at each sample location, the following were recorded: distance from the previous location using a tape measure along the roadside ( $dm$ ), the azimuth of this measurement ( $\mu$ ), and the azimuth ( $\alpha$ ) and dip ( $\beta$ ) of the foliation. The angle ( $\eta$ ) between road azimuth ( $\mu$ ) and the normal to foliation ( $\nu$ ) is determined (eq. 2). The horizontal distance between samples located perpendicular to foliation ( $dh$ ) equals the horizontal distance along the road ( $dm$ ) times the cosine of  $\eta$  (eq. 3).

The sine of the foliation dip ( $\beta$ ) multiplied by the horizontal distance between samples located perpendicular to foliation ( $dh$ ) give us the true distance across the foliation from the previous point (eq. 4). This value is then added to the value obtained from the previous point to give the real distance across the main structure measured from the uppermost structural boundary ( $d$ ) (eq. 5).

The relevant calculations are described below:

*$D_m$  = distance measured along the road from the upper structural*

*boundary of the AB*

$dm$  = distance measured from previous point along the road

$\mu$  = azimuth of the distance measured from the previous point along the road

$\alpha$  = azimuth of foliation

$v$  = azimuth of trace normal to structure

$\eta$  = angle between distance from previous point along the road

and horizontal distance normal to structure

$dh$  = horizontal distance between samples located perpendicular to foliation ( $dh$ )

$\beta$  = Foliation dip

$d$  = Real distance across the structure from the previous point

$D$  = Real distance across the structure measured from the upper  
structural boundary of the AB

To find the azimuth of trace normal to structure ( $v$ ):

$$(1) v = \alpha - 90$$

To find the angle between the distance measured from previous point along the road and the horizontal distance normal to the structure azimuth ( $\eta$ ) (angle between  $dm$  and  $dh$ ):

$$(2) \eta = 180 - (\mu - v) \text{ (if } \mu > 180^\circ)$$

$$\eta = \mu - v \text{ (if } \mu \leq 180^\circ)$$

To find horizontal distance between samples located perpendicular to foliation (dh):

$$(3) dh = dm \cos \eta$$

The dip is measured at each outcrop and converted to radians as discussed above.

To find the real distance across the main structure, which is the distance used in the distance vs major element plots:

$$(4) d = dh \sin \beta$$

$$(5) D = \sum d_i \quad i: \text{number of sample locations}$$

## ***3.2 Geochemical Methods***

### ***3.2.1 Sample preparation***

Major element geochemistry was determined by x-ray fluorescence (XRF), using the Bruker S4 Pioneer XRF at the Department of Geosciences at the University of Wisconsin-Milwaukee. To prepare a sample for XRF analysis, each rock sample was broken into small, fresh fragments using a 4lb hammer. These fresh, unweathered fragments were crushed into a powder using a Rocklabs shatterbox mill for 4 minutes. Once the rock was powdered, the sample was transferred into a glass vial and labeled. Each vial was placed in a low temperature oven (105°C) for a period of 8-10 hours to dry. Samples were cooled in a glass desiccator.

To calculate Loss On Ignition (LOI) for each sample, four empty crucibles were pre-ignited for 5 minutes in a high temperature oven (1050°C) to burn off any residual material, and then cooled in a desiccator. Each crucible was placed on a balance and tared, and approximately 0.5g of sample was added. The sample weight was recorded and the crucible and sample were weighed together and recorded. Four crucibles at a time containing samples were placed into the high temperature oven for 15 minutes. After 15 minutes each crucible was placed in the desiccator until cool to the touch. The sample and crucible were then weighed and recorded. The weight of the sample and crucible after heating was subtracted from the weight of the sample and crucible before heating to measure the mass lost. This mass lost was divided by the original mass of sample in the crucible and multiplied by 100 to get an LOI percentage. This was entered into the XRF software before analysis of the prepared samples.

To prepare glass beads for XRF analysis, we mixed 1g of powdered rock sample with 1g of ammonium nitrate and 10 grams of a 50/50 lithium tetraborate/lithium metaborate flux with an integrated LiBr non-wetting agent. The flux and sample measurements need to be accurate to 0.0003g. This mixture was transferred into a platinum crucible and fused in a Claisse M4 fluxer for ~21 minutes using a pre-programmed routine designed for silicate rocks. Each bead was then analyzed for major, minor, and some trace elements using the Bruker S4 Pioneer XRF.

Concentrations were calculated using a calibration based on 11 USGS rock standards (detailed methods of McHenry, 2009; Byers et al., 2017). For data quality, the following standards are applied: 1) Elemental values should be more than twice the lower limit of detection (LLD) and if not then they should be eliminated, and 2) elements with more than 12% error should be eliminated. No element analyzed in this data failed these standards and therefore no samples were omitted.

### *3.2.2 Data plots*

To visualize our elemental concentrations, two different plots are used; 1) Geochemistry vs. distance from top of structure and 2) Isocon plot comparison. The first plots demonstrate how major elements change across each transect with distance from the top of the structure. Each graph is color-coded by rock domain as follows: 1) Coarse-grained banded amphibolites containing clinopyroxene; dark green shading, 2) Medium-grained banded amphibolites with no clinopyroxene; bright green shading, 3) Sheared amphibolites; pale green shading and 4) Chlorite mafic schists; pale blue shading. Areas of folds/microfolds are represented as a zig-zag/ wavy symbol in the scale bar below each graph. The color-coding of the graphs allows identification of major element trends as we move through the four rock domains, from the top of the structure toward to the shear contact. This will

allow chemical characterization of the shear zone and possibly relate chemical changes with metamorphism patterns.

The second analytical approach involves isocon plots, which are used frequently in geochemical research (Webb and Golding, 1998, Whitbread and Moore, 2004, Marsh et al., 2011). Isocon plots allow comparison of an altered sample against its unaltered protolith to see which elements were lost or gained during alteration of the system. For this research, a number of “protoliths” were chosen to which the samples were compared. First, the samples were compared to the unaltered protolith of each transect, which is a sample from domain one, the coarse-grained banded amphibolites with pyroxene which were only affected by D1 (figs. 14-19 top). This domain signifies the top of transect and the furthest from the shear contact and therefore the most undeformed of the rocks sampled. These rocks preserve the D1 deformation and, by using this rock as the unaltered comparison, we can see which elements were gained or lost to the system as a product of the retrograde metamorphism (D2). When comparing transects, it became clear that there are differences in elemental composition between “protolith” samples, so next the samples were compared to a “protolith” of average MORB composition from Gale et al. (2013; figs 14-19 middle). A comparison to MORB is reasonable because previous work (Bard 1969, Bard and Moine 1979, Dupuy et al., 1979) determined that the AB had a MORB affinity. These isocon

plots contain all samples collected from each transect, so all samples (those that experienced only D1 and those that experienced both D1 and D2) are compared to the “protolith” for this analysis. A third method compared the samples of each transect to an averaged, representative protolith. The protolith is an average composition of the upper banded amphibolite domains across all transects (domain 1 and domain 2) that were unaffected by D2 and therefore preserve D1. A standard deviation calculation was then performed on these values to obtain an upper and lower range. Any samples with values outside of this field were omitted and a new average was calculated (figs 14-19 bottom).

For all isocon plots, mass-balance considerations were ignored and the slope is assumed to be 1:1 with no change in bulk composition. The 1:1 line is calculated by joining all of the major element compositions within the unaltered protolith, so any enrichments or depletions of elements will fall above or below this line, respectively. In order to fit all of the major elements appropriately on one graph, the weight percent of each element was adjusted using the following ratios:

SiO<sub>2</sub>: 1:0.5

Al<sub>2</sub>O<sub>3</sub>: 1:1

Fe<sub>2</sub>O<sub>3</sub>: 1:1.75

TiO<sub>2</sub>: 1:10

Na<sub>2</sub>O: 1:1

CaO: 1:1

MgO: 1:1

MnO: 1:30

P<sub>2</sub>O<sub>5</sub>: 1:5

K<sub>2</sub>O: 1:20

These adjustments were arbitrarily chosen to fit all of the elements evenly spaced on the same graph to be readable without overlaps. These adjustments are consistent throughout each transect. While scaling may affect the slope line and yield misleading results (Mukherjee and Gupta, 2008), this is not the case for our plots as all samples are compared against one value for each element within the unaltered protolith. The isocon plots were color coded by each domain as well as symbol-coded in areas of folding. The color coding is as follows: 1) Coarse-grained banded amphibolites containing clinopyroxene (protolith); dark green circle, 2) Medium-grained banded amphibolites with no clinopyroxene; bright green circle, 3) Sheared amphibolites; pale green circle and 4) chlorite mafic schists; pale blue circle. Samples collected in areas of obvious folding are represented by the triangle symbol and colored according to the rock domain to which they belong.

## 4. RESULTS

### *4.1 Geochemistry vs. distance from the top of the structure*

#### **Transect 1:** (figs. 7a-c)

The 300 m mark, which approximately coincides with the sheared amphibolite/mafic chlorite schist transition boundary, marks a decrease in  $\text{Fe}_2\text{O}_3$ ,  $\text{TiO}_2$ , and  $\text{MnO}$ , and an increase in  $\text{Al}_2\text{O}_3$ . Within 100 m of the shear zone boundary a sharp increase in  $\text{MgO}$  coincides with a decrease in  $\text{SiO}_2$  and  $\text{Na}_2\text{O}$ .  $\text{P}_2\text{O}_5$  and  $\text{CaO}$  show varying trends of enrichment and depletion.

#### **Transect 2:** (figs. 8a-c)

The sheared amphibolite/mafic chlorite schist transition boundary is approximately 200 m from the top of the structure. However, strain is not as uniformly gradational as in transect 1 and sheared amphibolite appears again at approximately the 250 m mark for about 70 m after the initial mafic chlorite schist transition. The first sheared amphibolite/mafic-chlorite schist transition is marked with a decrease in  $\text{Fe}_2\text{O}_3$ ,  $\text{TiO}_2$ ,  $\text{SiO}_2$ , and  $\text{P}_2\text{O}_5$ .  $\text{Na}_2\text{O}$  decreases toward the shear boundary.  $\text{K}_2\text{O}$ ,  $\text{MnO}$ ,  $\text{CaO}$ ,  $\text{MgO}$ , and  $\text{Al}_2\text{O}_3$  show varying trends of enrichment and depletion. Unlike the patterns seen in transect 1, there are no obvious changes immediately adjacent to the shear zone.

**Transect 3:** (*figs. 9a-c*)

Few of the elements display prominent patterns with distance from the shear boundary in transect 3.  $\text{Al}_2\text{O}_3$  trends are relatively stable before showing chaotic patterns after the sheared amphibolite/mafic chlorite schist transition. MgO shows an increase immediately before the shear boundary.  $\text{SiO}_2$  and  $\text{Na}_2\text{O}$  decrease at the sheared amphibolite/mafic chlorite schist transition before increasing again toward the shear boundary.

**Transect 5:** (*figs. 10a-c*)

Unfortunately, transect 5 had limited outcrops and thus limited samples. The four samples collected only cover two domains; the medium-grained banded amphibolite without pyroxene (domain 2) and the sheared-amphibolites (domain 3). The plots show an increase in  $\text{SiO}_2$  and  $\text{Na}_2\text{O}$  from domain 2 to 3. All other elements show no discernable trends.

**Transect 6:** (*figs. 11a-c*)

Transect 6 is another transect with relatively little outcrop and contained no domain 2 (medium-grained banded amphibolites without clinopyroxenes), which was likely covered. However, the most important units of the two retrograde domains and the protolith were all sampled in this transect. The plots show a

steady decrease in SiO<sub>2</sub>, MgO, and K<sub>2</sub>O toward the shear contact. Na<sub>2</sub>O increases at the banded amphibolite/sheared amphibolite boundary and then steadily decreases towards the shear zone. Conversely, CaO decreases at the banded amphibolite/sheared amphibolite boundary and then steadily increases towards the shear zone with some variability in the chlorite schists.

**Transect 8:** (*figs. 12a-c*)

In transect 8, the banded amphibolite without cpx and the sheared-amphibolite transition boundary is approximately 500 m from the top of the structure and is marked by a decrease followed by an increase in Fe<sub>2</sub>O<sub>3</sub>, MnO, TiO<sub>2</sub>, and P<sub>2</sub>O<sub>5</sub>. K<sub>2</sub>O, Al<sub>2</sub>O<sub>3</sub>, MgO increase slightly across the shear zone. All other elements show no discernable patterns.

Overall, the element vs. distance plots depict variable geochemical changes, most prominently at the mafic chlorite schist transition or within the domain itself. Some of these trends are clearer than others, such as transect 1, which shows a clear increase in Al<sub>2</sub>O<sub>3</sub> with a decrease in MnO, TiO<sub>2</sub>, and Fe<sub>2</sub>O<sub>3</sub> following the mafic chlorite schist boundary. Al<sub>2</sub>O<sub>3</sub> displays chaotic geochemical patterns in the mafic chlorite schist domain compared to the structurally higher domains, as evident in transects 2 and 3. Each transect displays its own unique chemical signature and therefore trends are particularly clear. Isocon analysis provides a clearer insight to geochemistry of the SISZ.

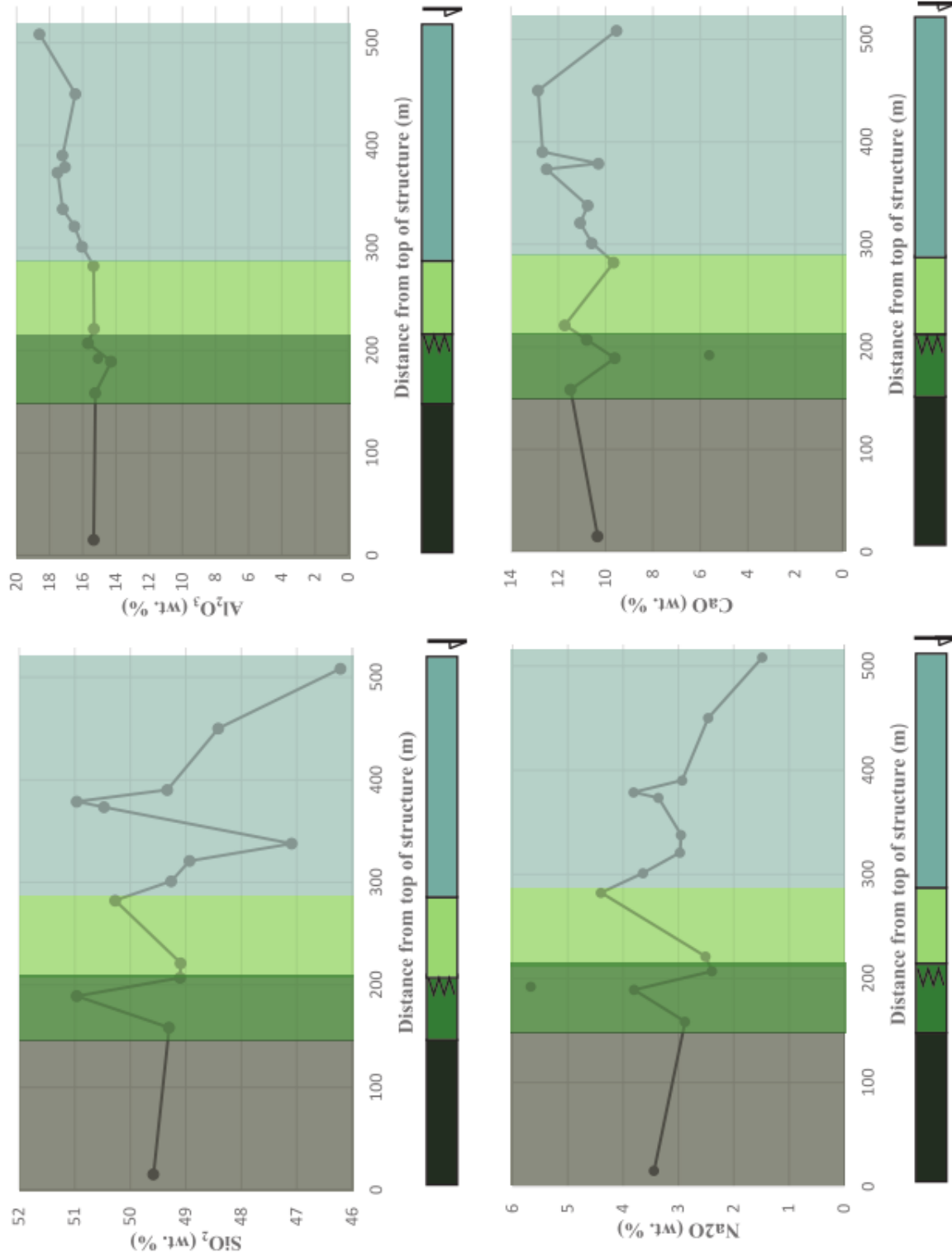


Figure 7a. Transect 1: SiO<sub>2</sub>, Al<sub>2</sub>O<sub>3</sub>, Na<sub>2</sub>O, and CaO variation with distance from top of structure (m).

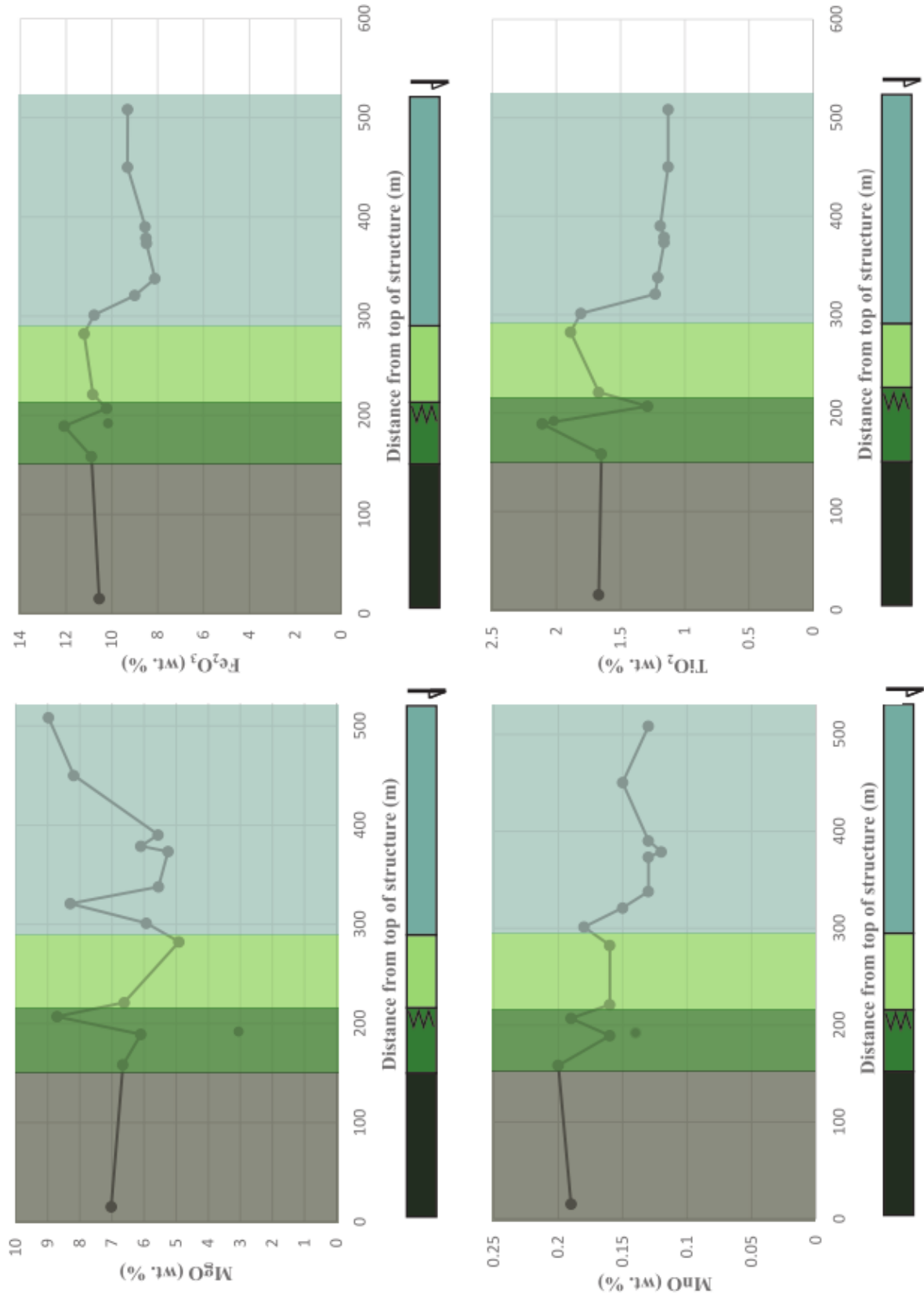


Figure 7b. Transect 1: MgO, Fe<sub>2</sub>O<sub>3</sub>, MnO, and TiO<sub>2</sub> variation with distance from top of structure (m).

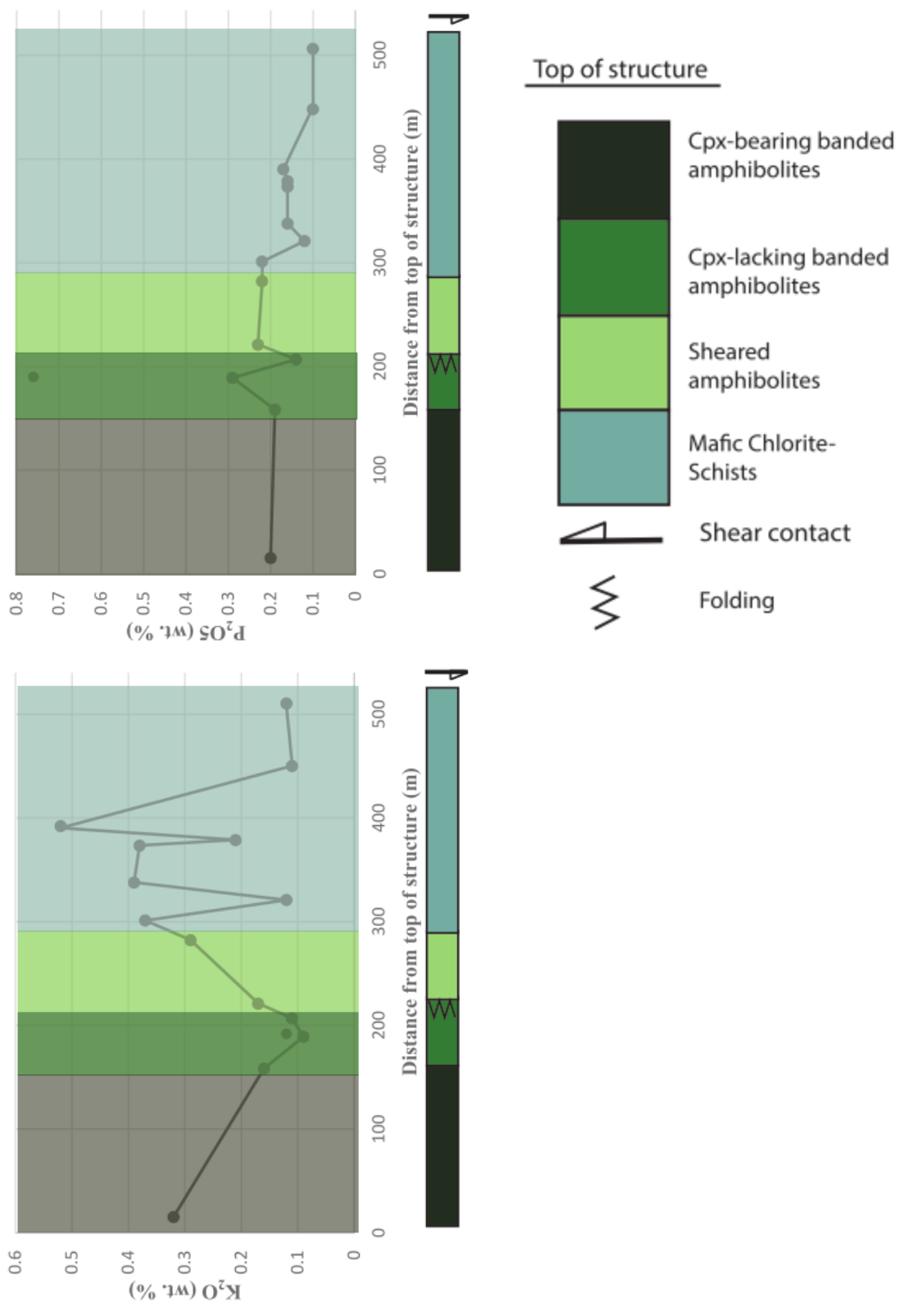


Figure 7c. Transect 1: K<sub>2</sub>O and P<sub>2</sub>O<sub>5</sub> variation with distance from top of structure (m).

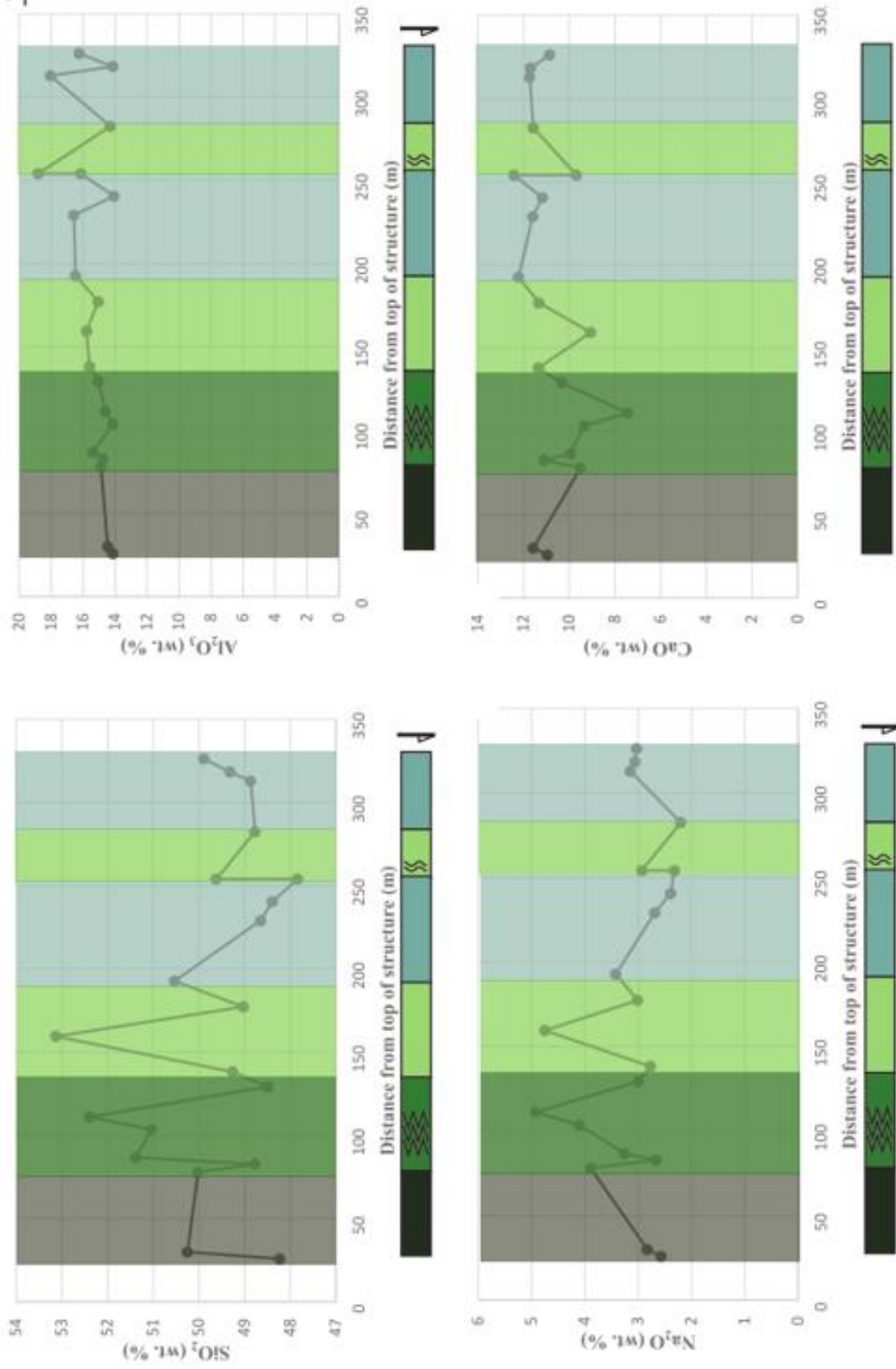


Figure 8a. Transect 2: SiO<sub>2</sub>, Al<sub>2</sub>O<sub>3</sub>, Na<sub>2</sub>O, and CaO variation with distance from top of structure (m).

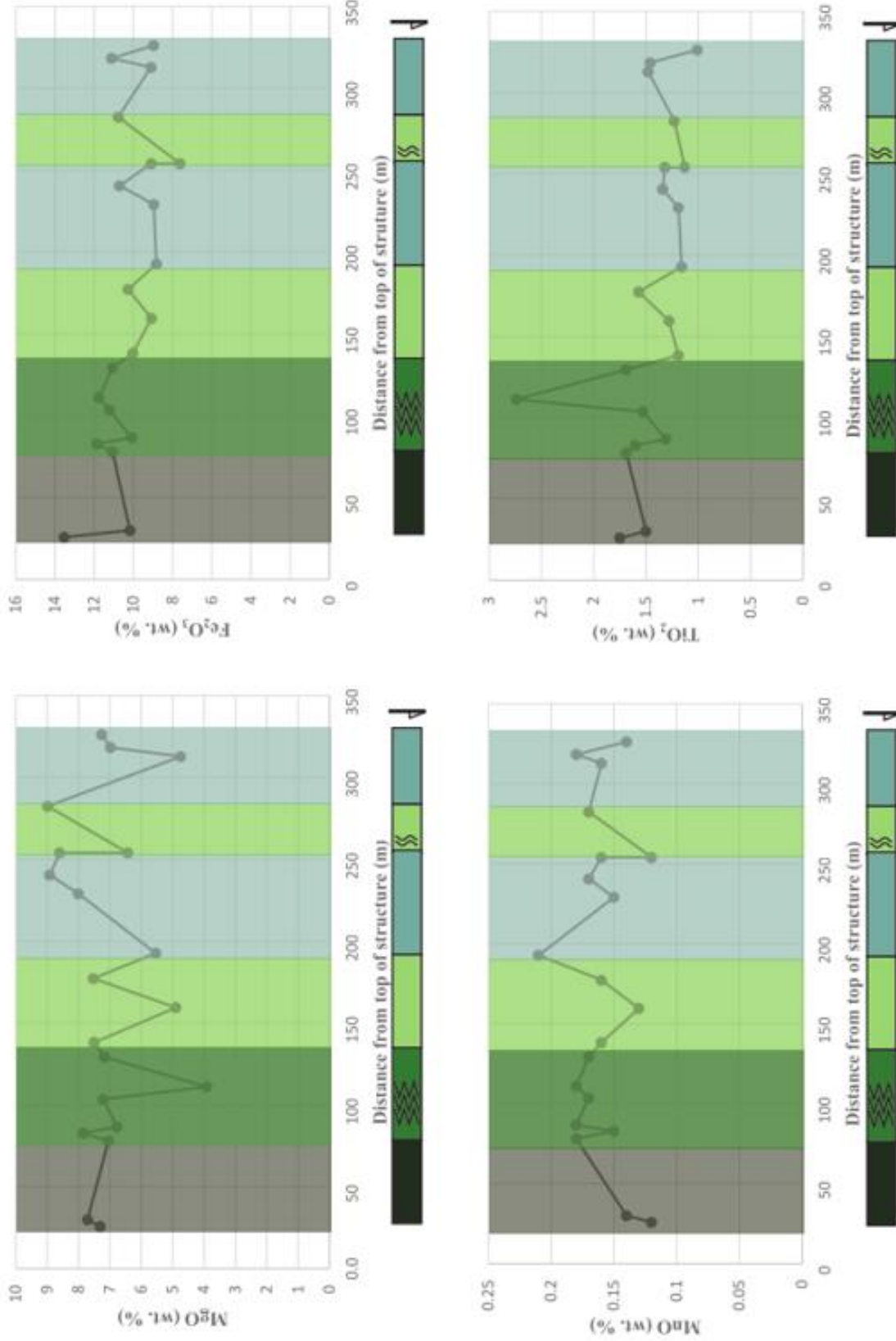


Figure 8b. Transect 2: MgO, Fe<sub>2</sub>O<sub>3</sub>, MnO, and TiO<sub>2</sub> variation with distance from top of structure (m).

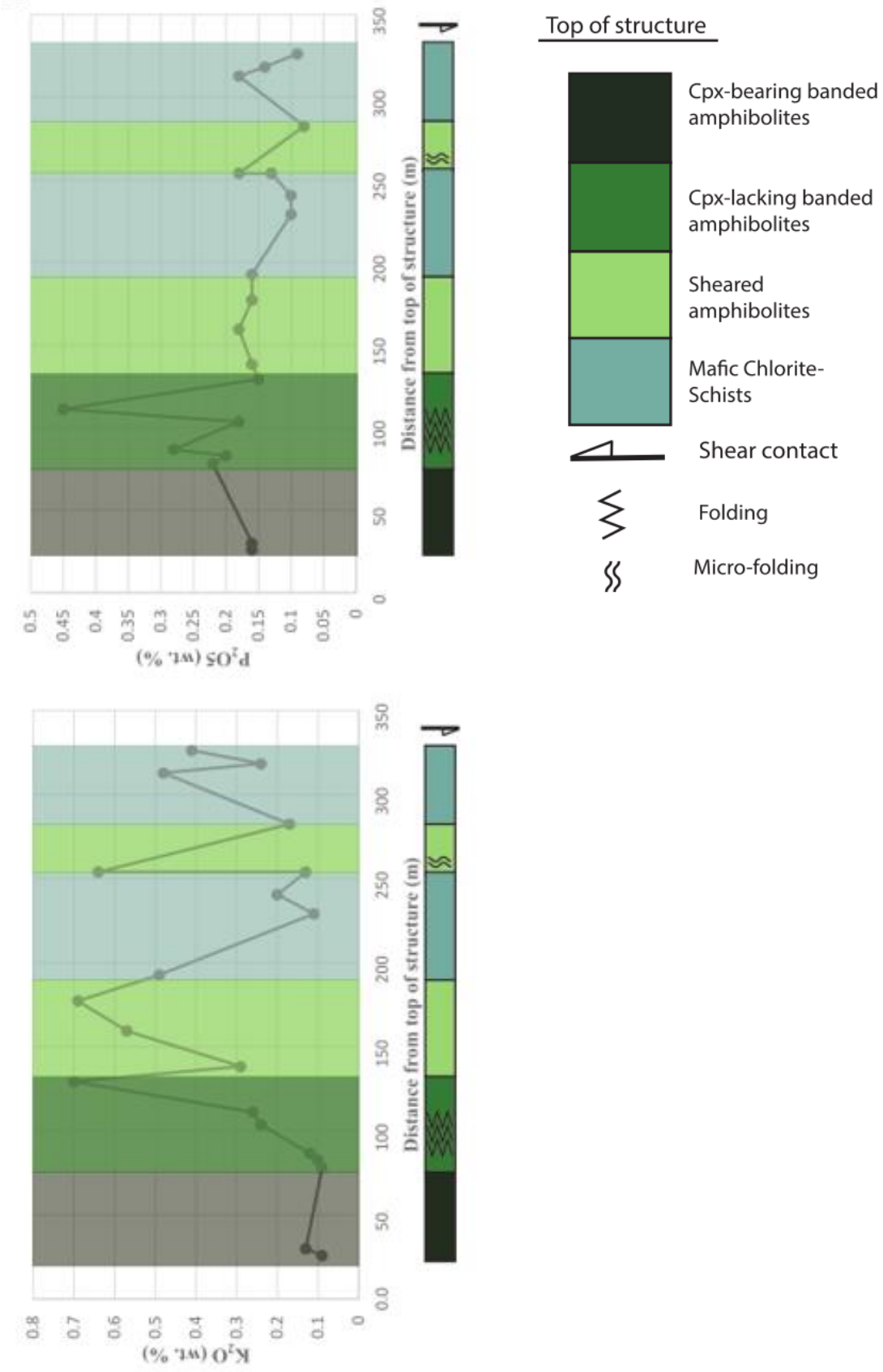


Figure 8c. Transect 2: K<sub>2</sub>O and P<sub>2</sub>O<sub>5</sub> variation with distance from top of structure (m).

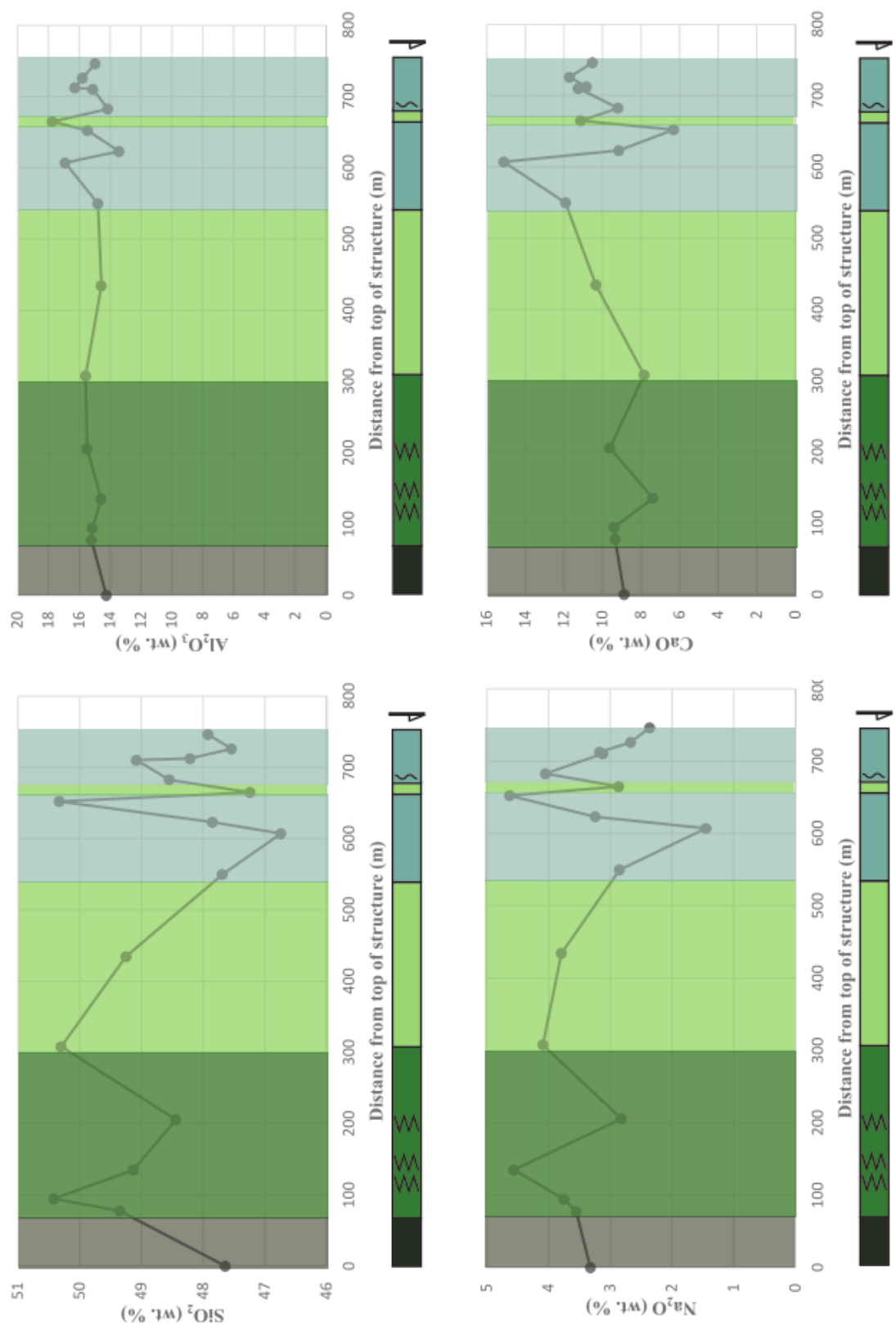


Figure 9a. Transect 3: SiO<sub>2</sub>, Al<sub>2</sub>O<sub>3</sub>, Na<sub>2</sub>O, and CaO variation with distance from top of structure (m).

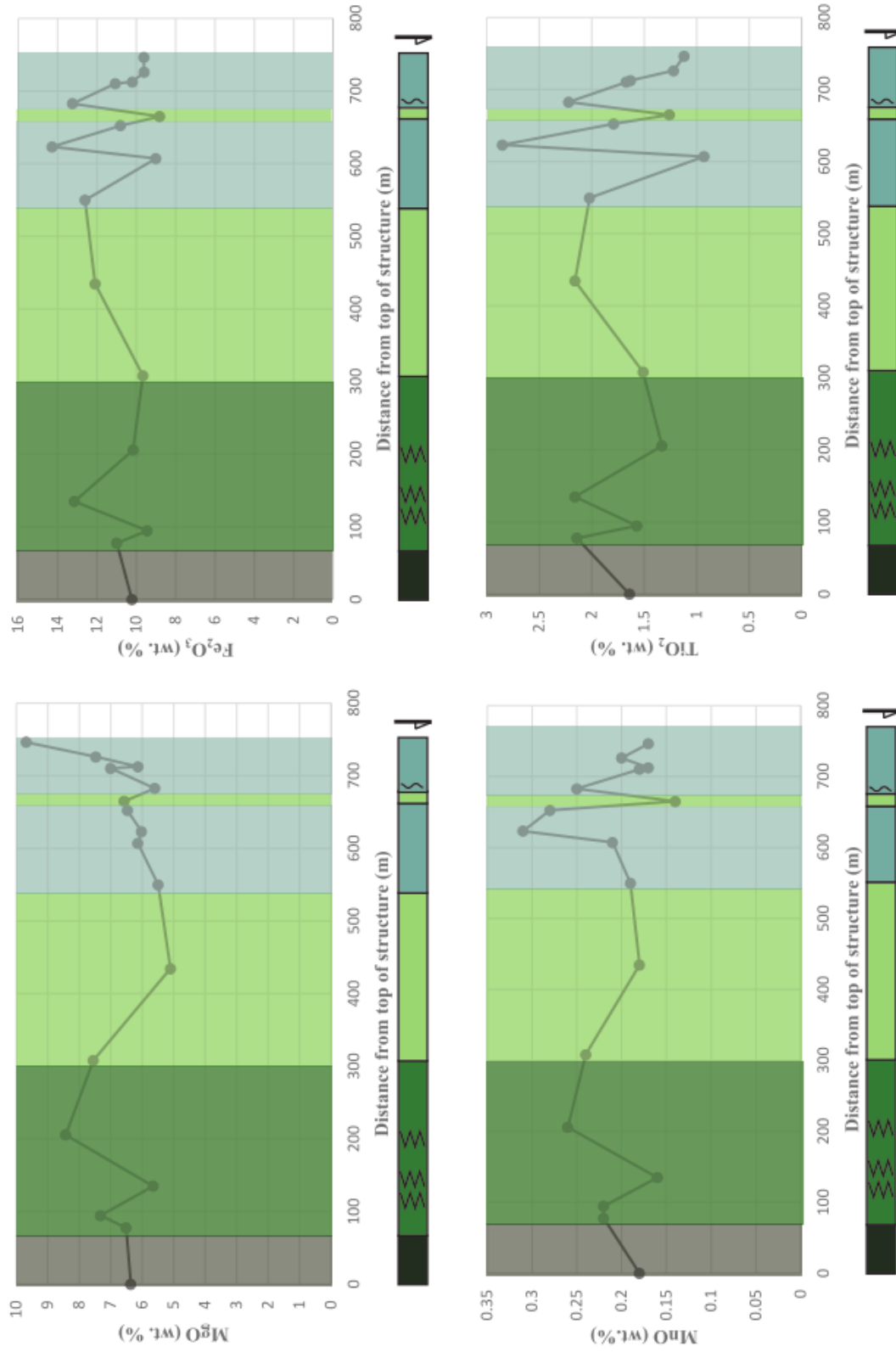
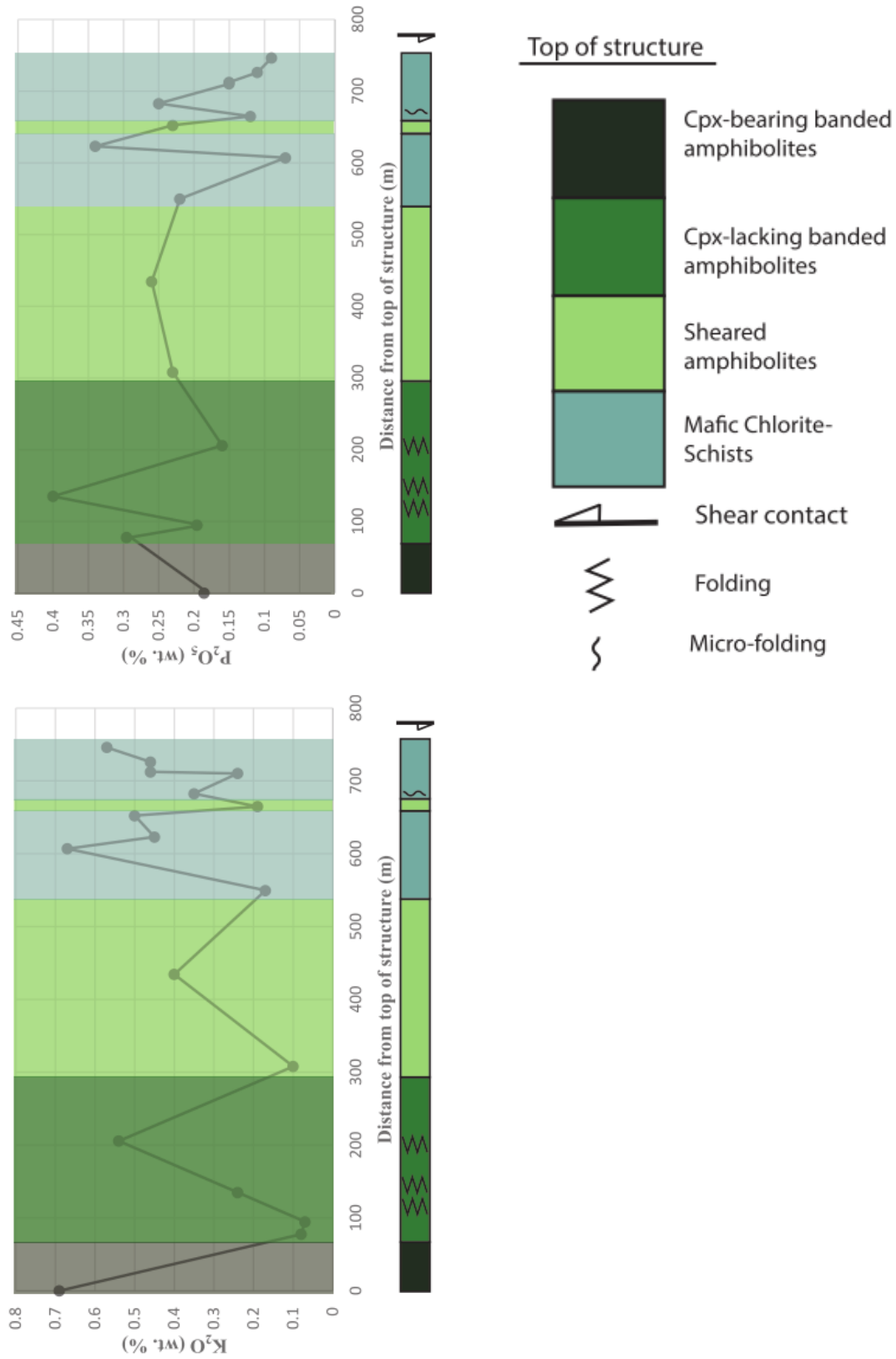


Figure 9b. Transect 3: MgO, Fe<sub>2</sub>O<sub>3</sub>, MnO, and TiO<sub>2</sub> variation with distance from top of structure (m).



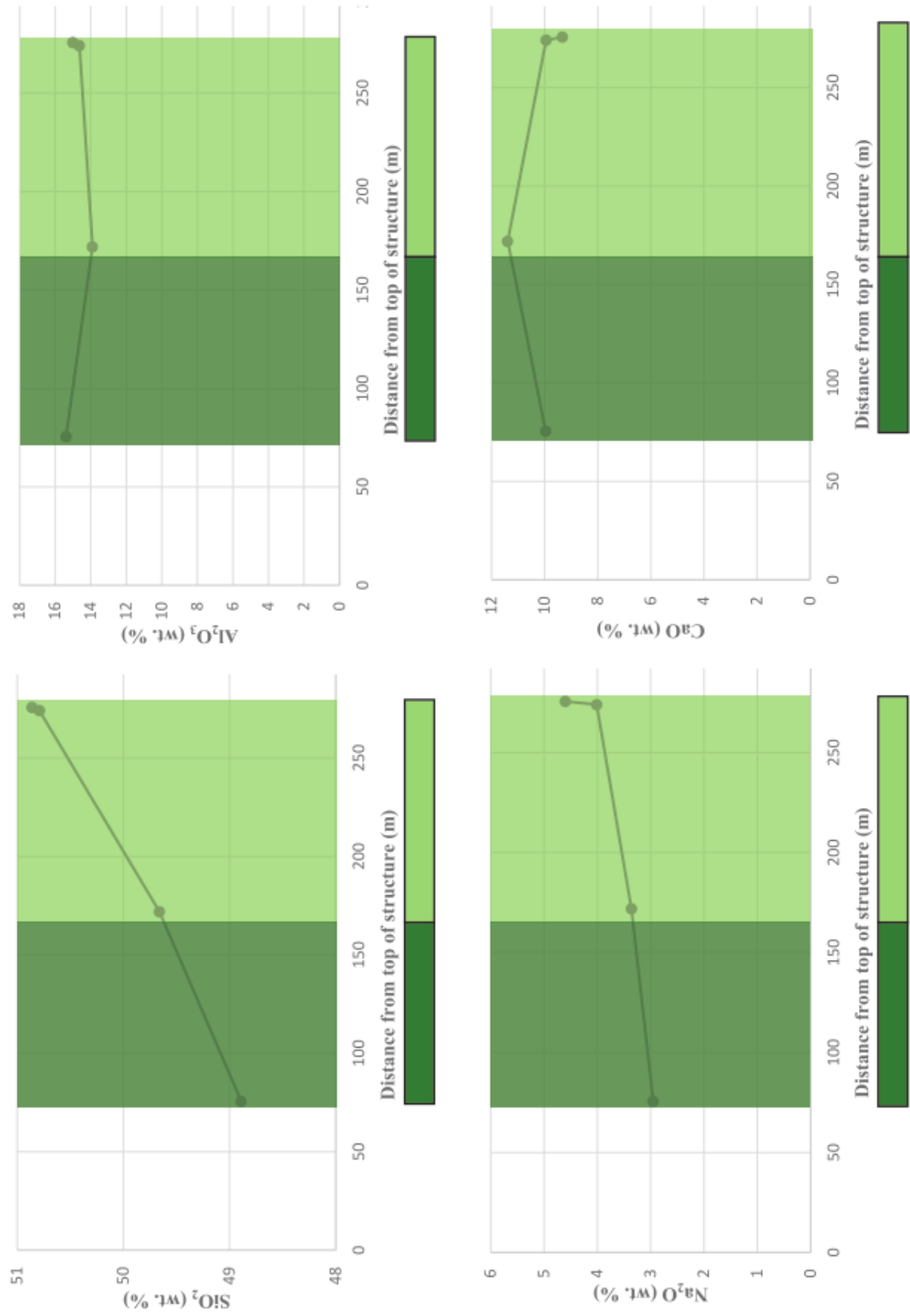


Figure 10a. Transect 5: SiO<sub>2</sub> and Al<sub>2</sub>O<sub>3</sub>, Na<sub>2</sub>O and CaO variation with distance from top of structure (m).

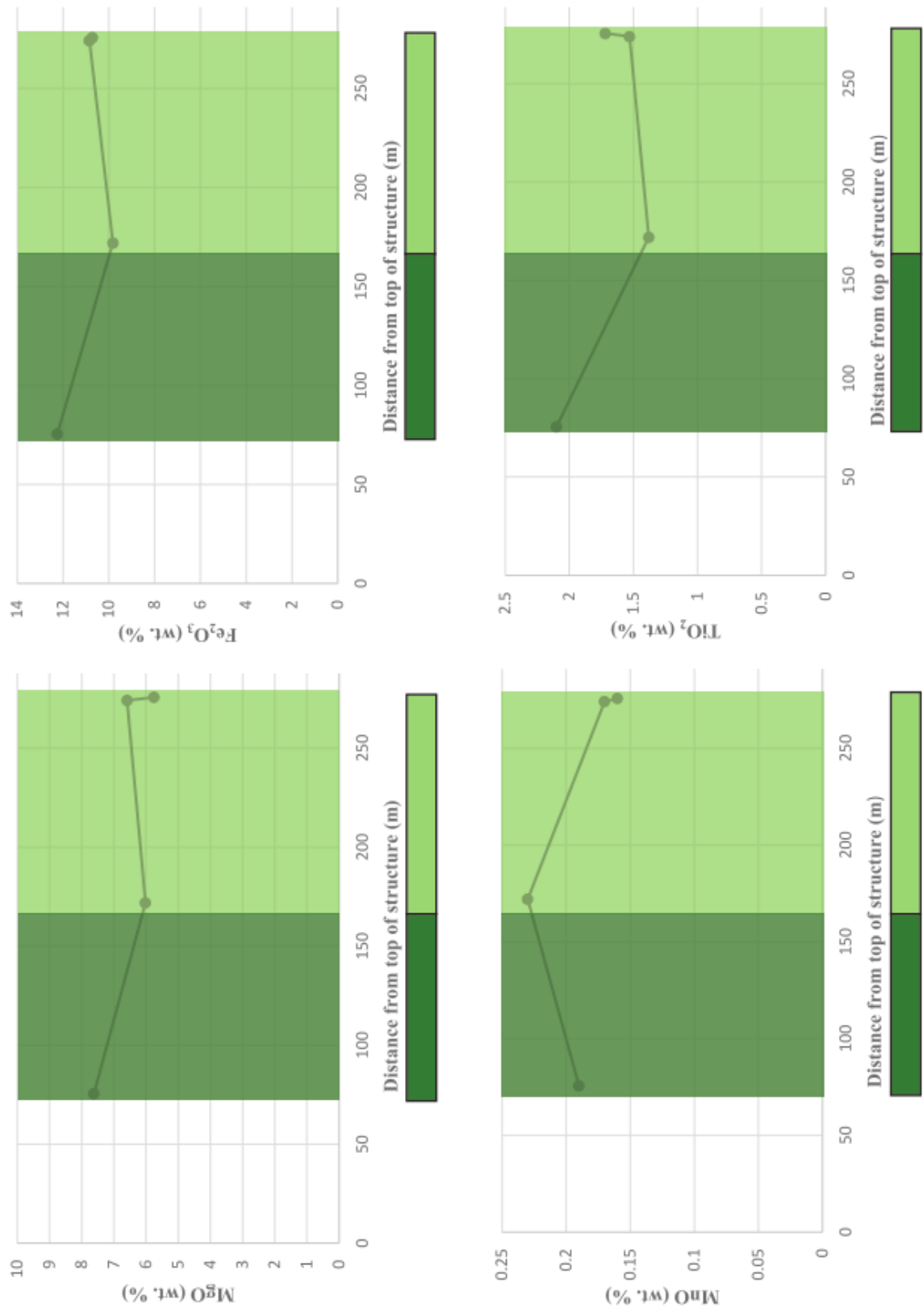


Figure 10b. Transect 5: MgO, Fe<sub>2</sub>O<sub>3</sub>, MnO, and TiO<sub>2</sub> variation with distance from top of structure (m).

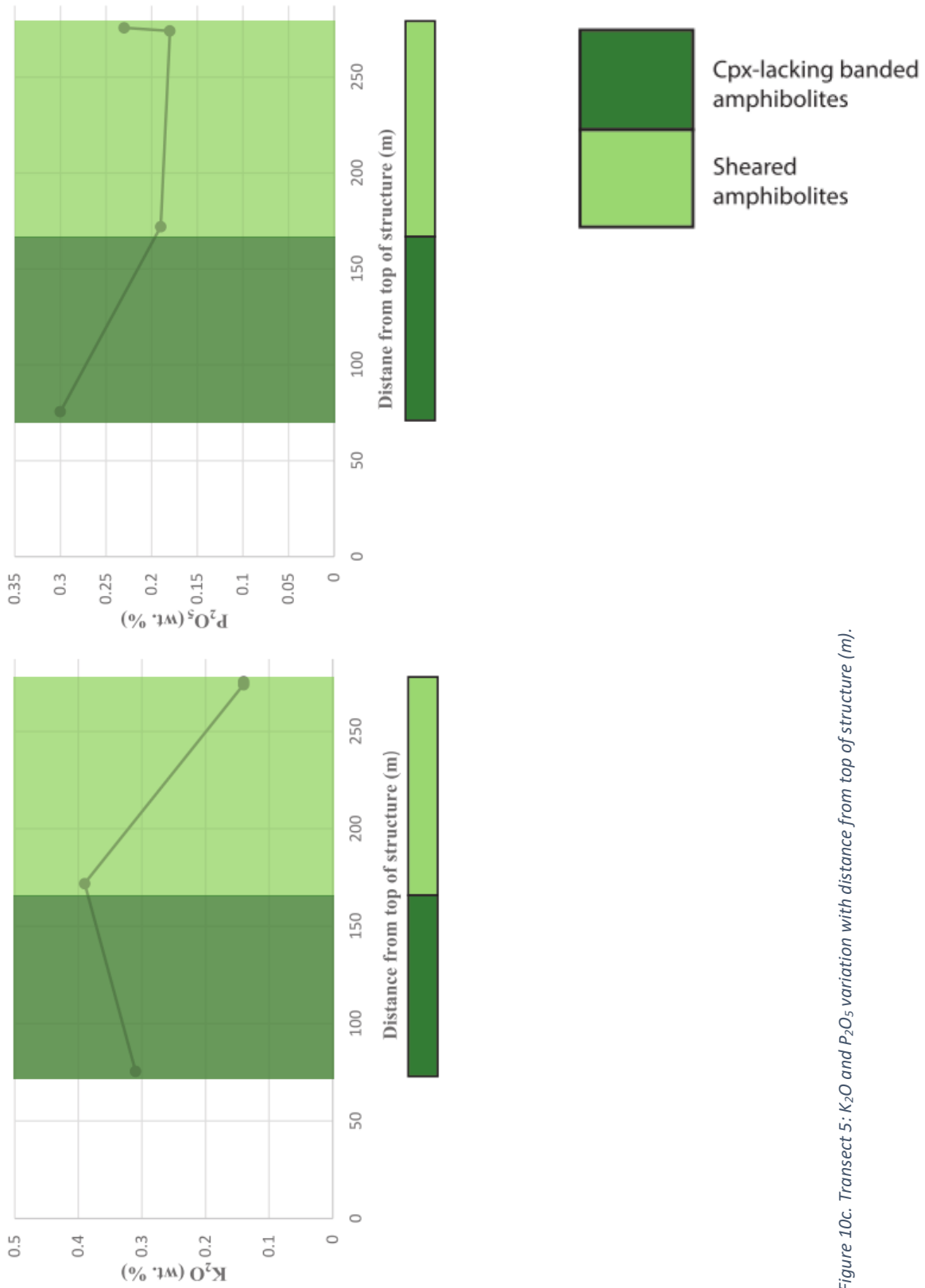


Figure 10c. Transect 5: K<sub>2</sub>O and P<sub>2</sub>O<sub>5</sub> variation with distance from top of structure (m).

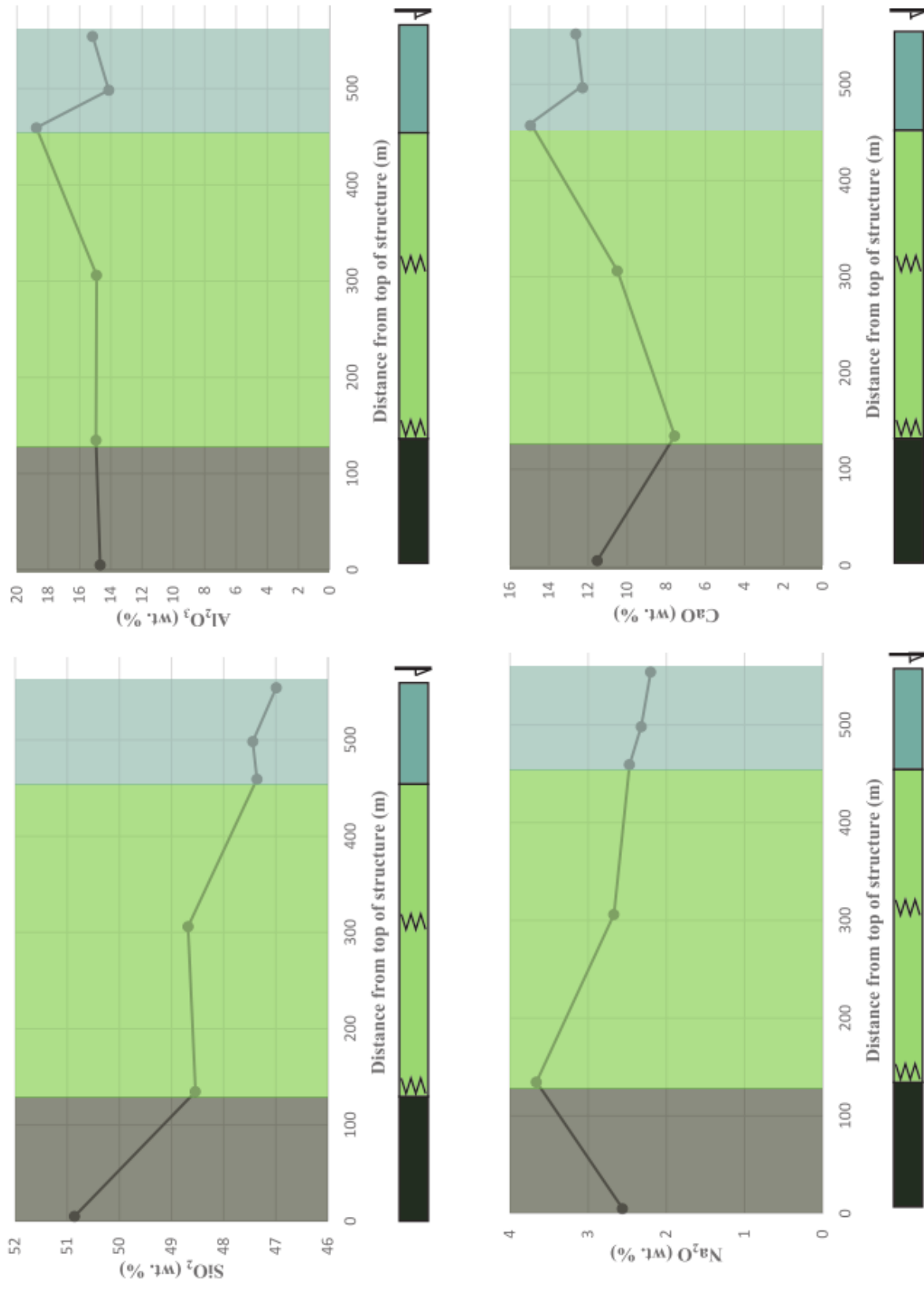


Figure 11a. Transect 6: SiO<sub>2</sub> and Al<sub>2</sub>O<sub>3</sub>, Na<sub>2</sub>O and CaO variation with distance from top of structure (m).

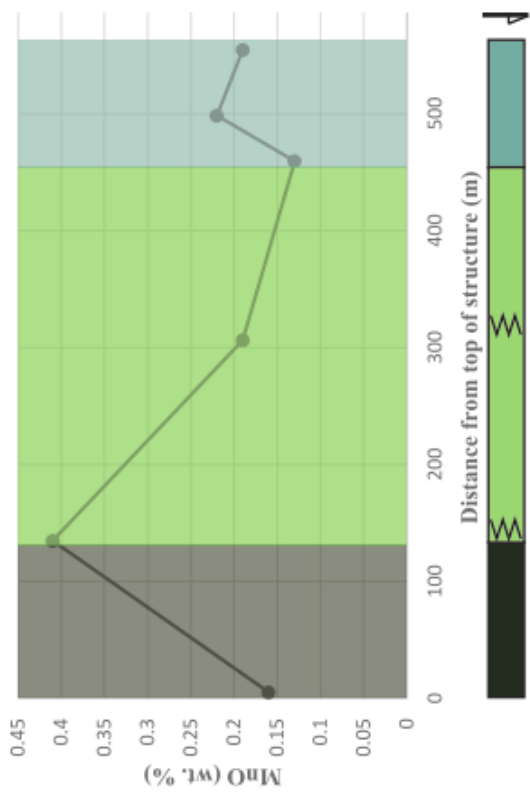
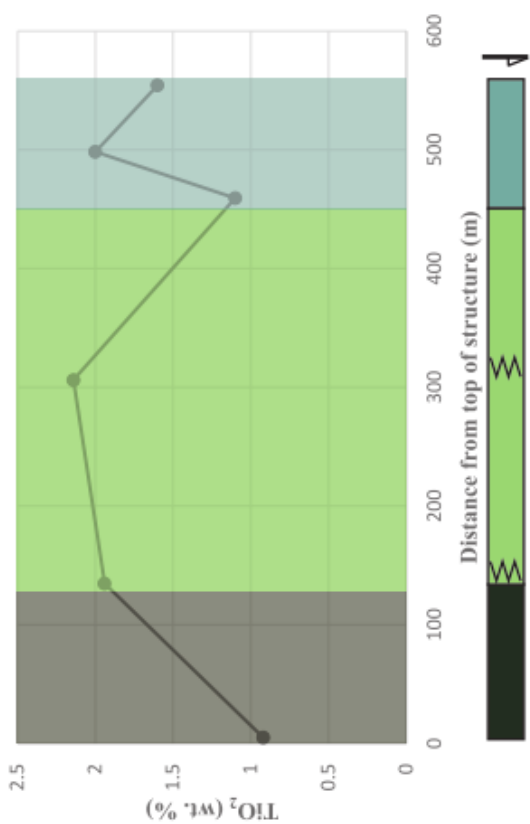
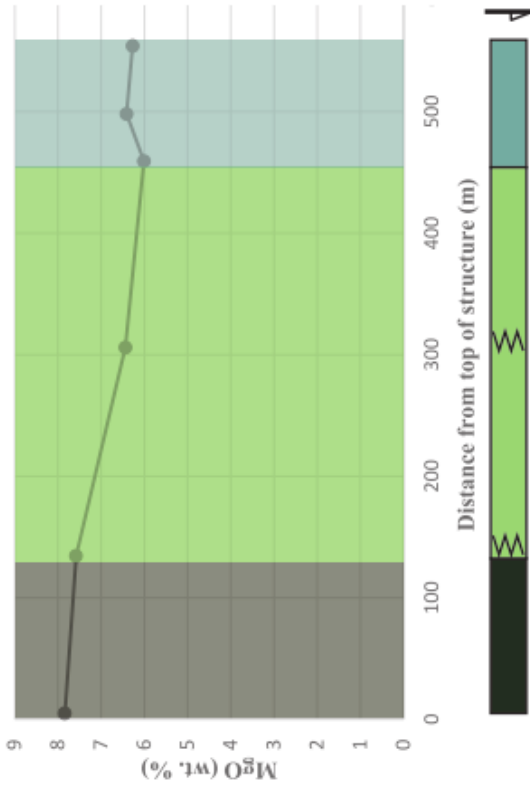
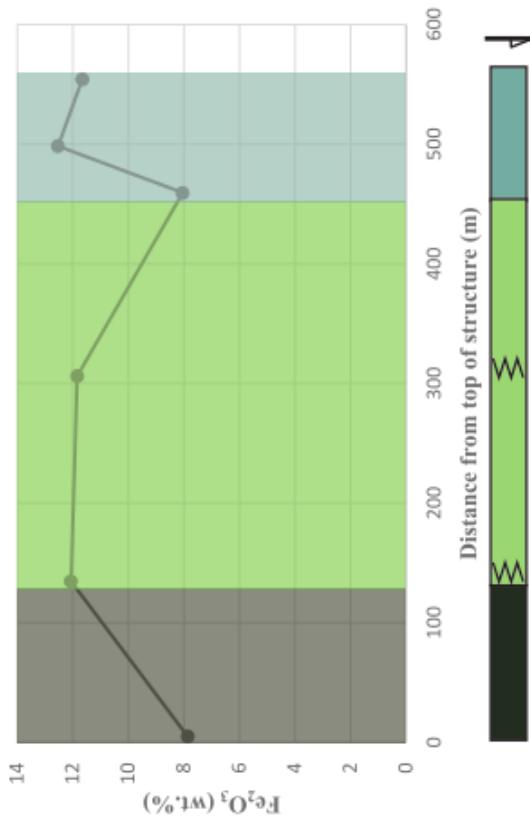


Figure 11b. Transect 6: MgO, Fe<sub>2</sub>O<sub>3</sub>, MnO, and TiO<sub>2</sub> variation with distance from top of structure (m).

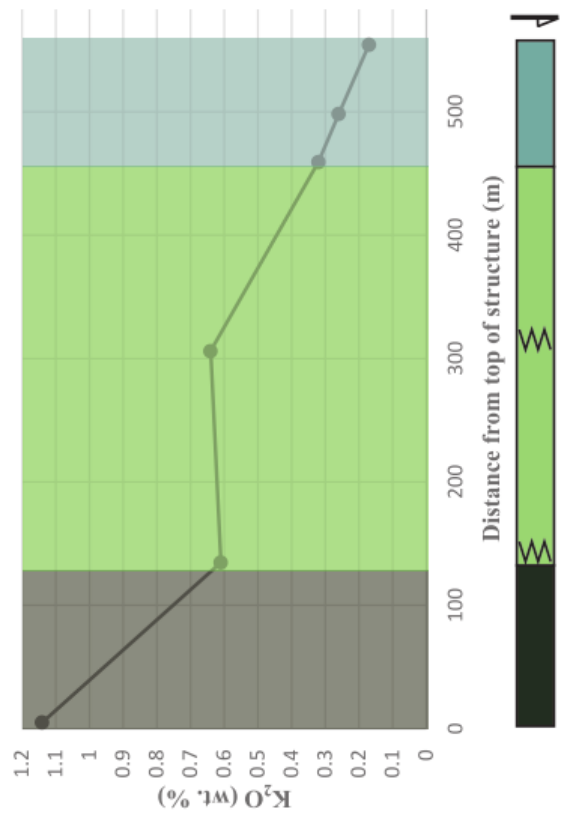
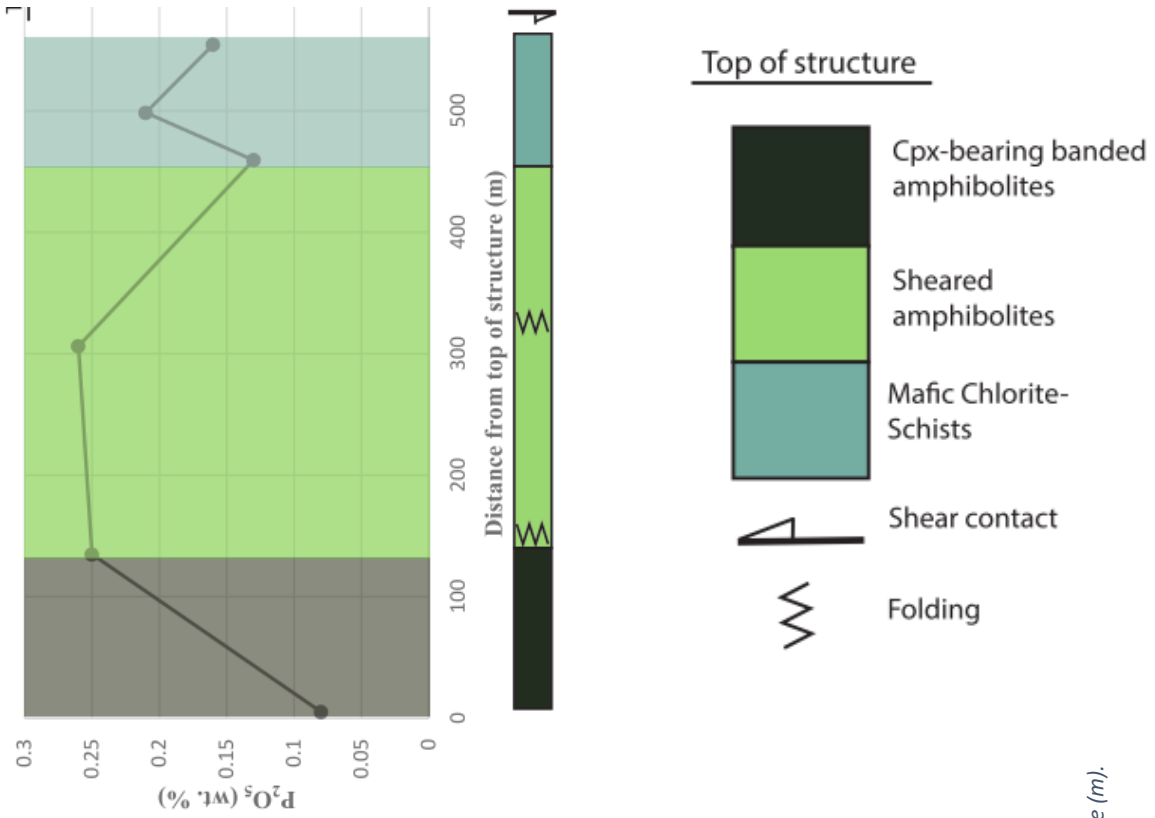


Figure 11c. Transect 6: K<sub>2</sub>O and P<sub>2</sub>O<sub>5</sub> variation with distance from top of structure (m).

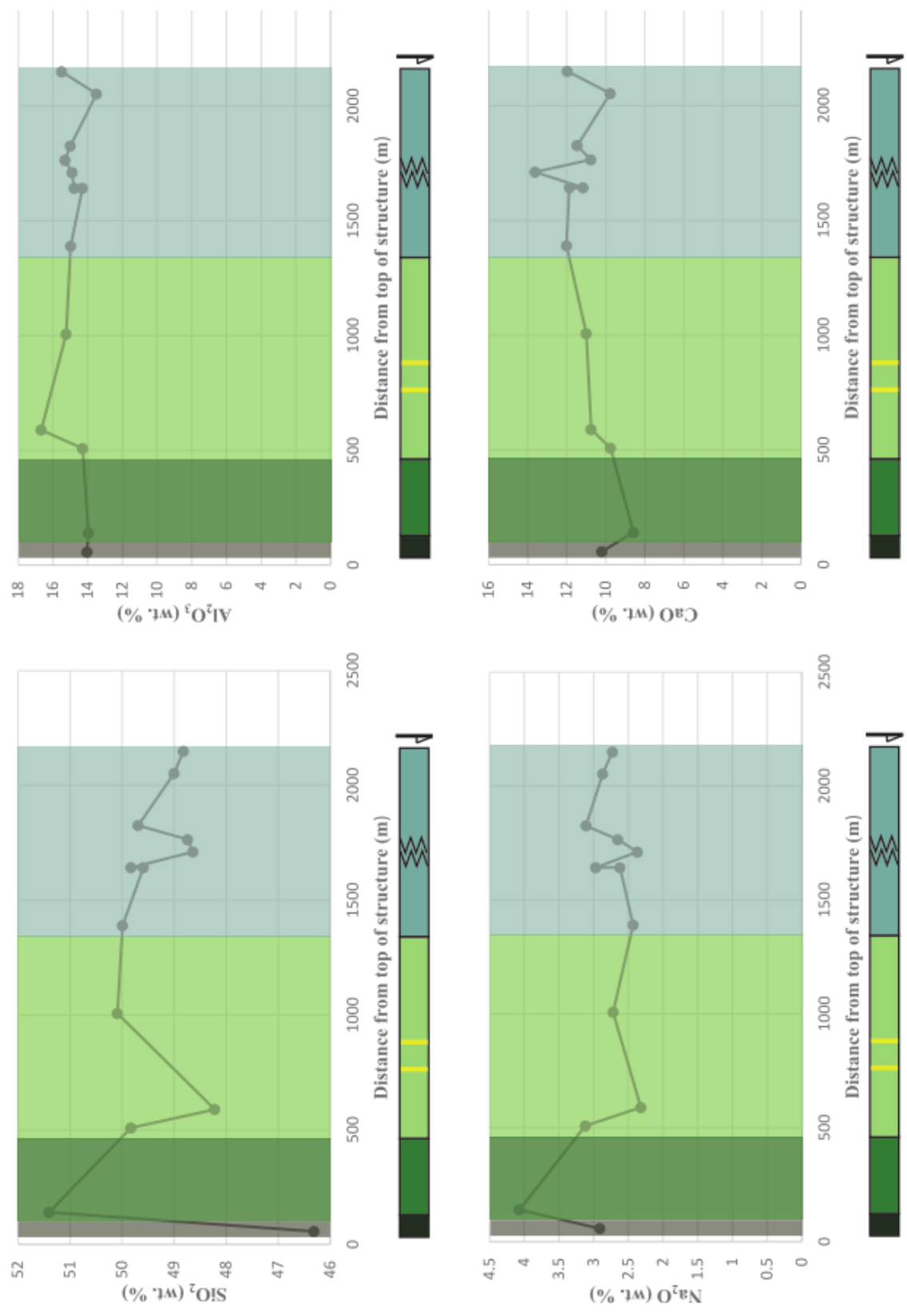


Figure 12a. Transect 8:  $\text{SiO}_2$  and  $\text{Al}_2\text{O}_3$ ,  $\text{Na}_2\text{O}$  and  $\text{CaO}$  variation with distance from top of structure (m).

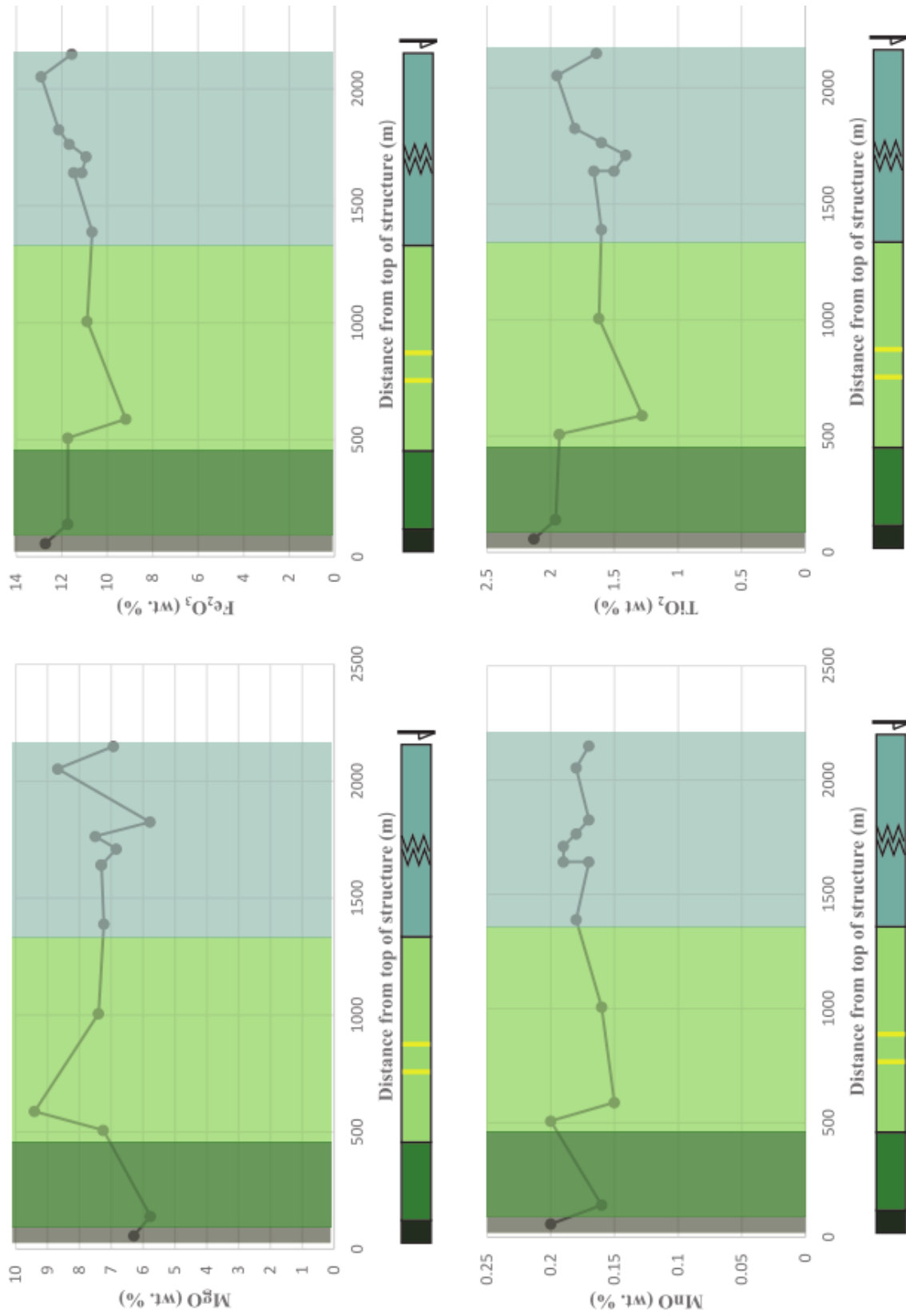


Figure 12b. Transect 8: MgO, Fe<sub>2</sub>O<sub>3</sub>, MnO, and TiO<sub>2</sub> variation with distance from top of structure (m).

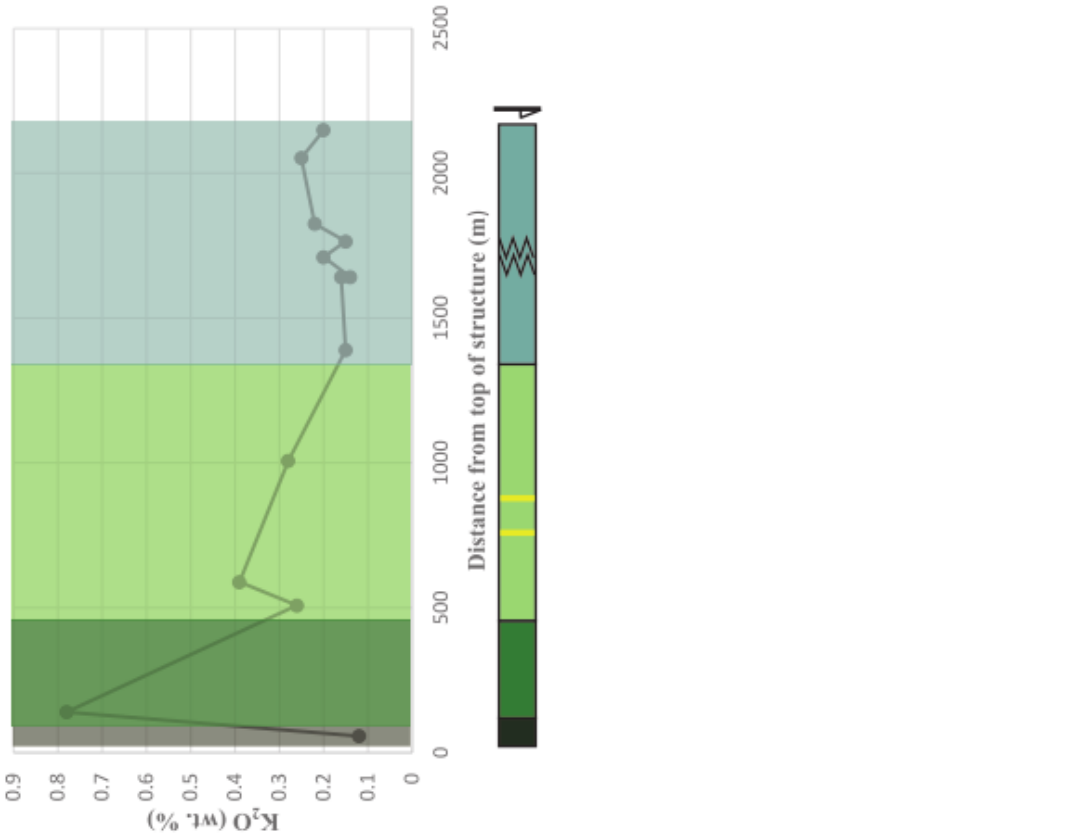
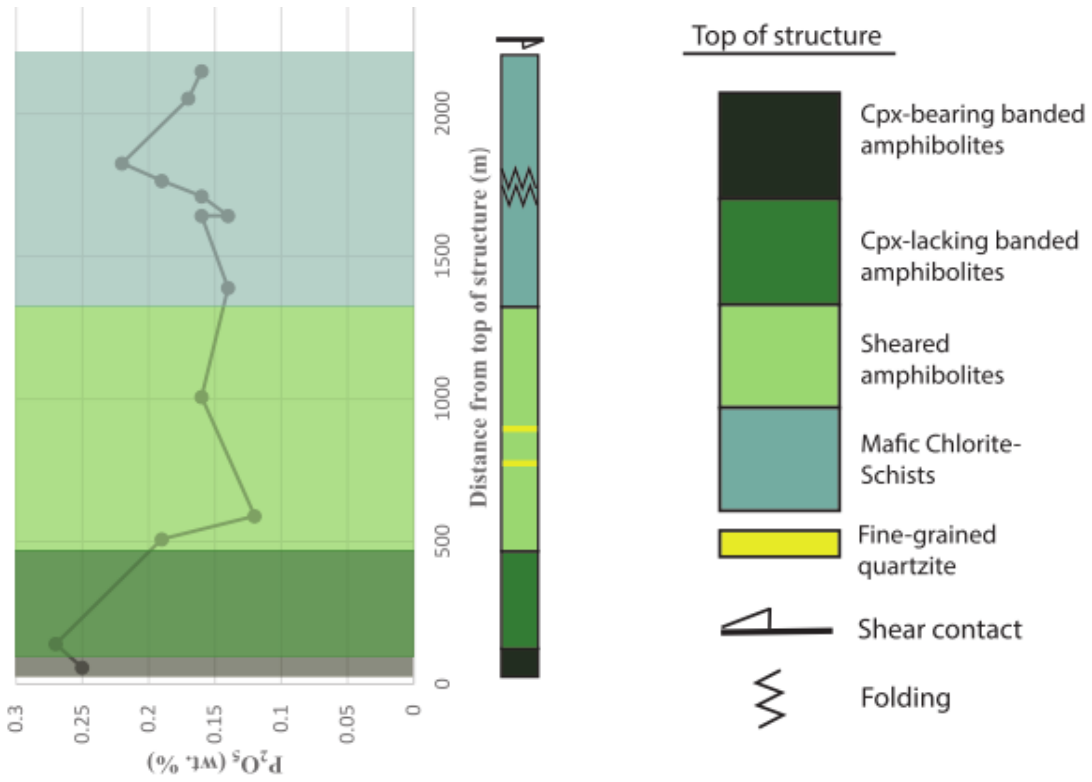


Figure 12c. Transect 8: K<sub>2</sub>O and P<sub>2</sub>O<sub>5</sub> variation with distance from top of structure (m).

## *4.2 Isocon analysis*

Isocon plots were also used to assess major element changes across the four domains. This method follows Grant (1986) and uses immobile elements, which do not typically move during fluid rock interaction, to define a line, which also goes through the origin. In this analysis we are comparing a range of samples to a protolith sample and thus the line is defined by the composition of the protolith. Data points that plot above this line represent samples that are enriched in a particular element relative to the protolith. Data points that plot below this line represent samples that are depleted in a particular element relative to the protolith. These do not quantitatively show mass loss or gain, but rather a comparison of samples closer to the shear zone with their protolith. For this analysis, three different methods of isocon plots were used, each comparing the samples of each transect to a different protolith each time. The first method compared the samples of each transect to the furthest rock outside of the shear boundary in the associated transect belonging to the banded amphibolite with cpx domain. This method subsequently had different protoliths for each transect. The second method compared the samples of each transect to a standardized protolith, the average MORB-composition (Gale et al., 2013). The third method uses the average protolith to determine a representative protolith. All of the upper banded amphibolite domains across all transects (domain 1 and domain 2) that were

unaffected by D2 and therefore preserve D1, were compiled and averaged, regardless on their position in the upper structures, and regardless of whether they were folded. A standard deviation calculation was then performed on these values to get an upper and lower range. Any samples with values outside of this field were omitted and a new average was calculated. This third method is preferred because of contrasting geochemical signatures among the protoliths of each transect, and therefore comparing all samples to the same, averaged protolith composition yielded more reliable results. Each transect has three isocon plots total depicting the results of each method. All elements are shown on each isocon plot. The results of each transect are as follows:

**Transect 1:** *(fig. 14 top)*

Within transect 1 there are no major elements that, when compared with the unaltered protolith, show depletion or enrichment for all of the altered samples. However, if we consider the mafic chlorite schists separately against the protolith because of their proximity to the shear contact, all samples of this domain are enriched in  $\text{Al}_2\text{O}_3$  and  $\text{CaO}$  and depleted in  $\text{Na}_2\text{O}$ ,  $\text{TiO}_2$ ,  $\text{MnO}$ ,  $\text{Fe}_2\text{O}_3$ , and  $\text{SiO}_2$ .  $\text{MgO}$ ,  $\text{K}_2\text{O}$  and  $\text{P}_2\text{O}_5$  are neither enriched nor depleted.

**Transect 2:** *(fig. 15 top)*

The isocon plots for transect 2 show a strong trend of K<sub>2</sub>O enrichment. Most of the samples show enrichment of Al<sub>2</sub>O<sub>3</sub> and MnO with depletion in SiO<sub>2</sub>. Na<sub>2</sub>O, Fe<sub>2</sub>O<sub>3</sub>, TiO<sub>2</sub>, P<sub>2</sub>O<sub>5</sub>, MgO, and CaO show varying trends of enrichment and depletion.

**Transect 3:** (*fig. 16 top*)

Contrary to trends in transect 2, the isocon plots for transect 3 show strong depletion of K<sub>2</sub>O accompanied by an enrichment of SiO<sub>2</sub> and Al<sub>2</sub>O<sub>3</sub>. Fe<sub>2</sub>O<sub>3</sub>, TiO<sub>2</sub>, P<sub>2</sub>O<sub>5</sub>, Na<sub>2</sub>O, MnO, MgO, and CaO show varying trends of enrichment and depletion.

**Transect 5:** (*fig. 17 top*)

Because of the limited domains represented in transect 5, the “protolith” used in this isocon plot is from rock domain 2, the medium grained banded amphibolite without pyroxene. This is not the same domain as the other protoliths, however, it is the closest to the structural top of the metabasites for this transect. The isocon plot shows a depletion of P<sub>2</sub>O<sub>5</sub>, MgO, Al<sub>2</sub>O<sub>3</sub>, TiO<sub>2</sub> and Fe<sub>2</sub>O<sub>3</sub> with an enrichment in Na<sub>2</sub>O and SiO<sub>2</sub>. CaO, MnO and K<sub>2</sub>O show varying trends of enrichment and depletion.

**Transect 6:** (*fig. 18 top*)

Because of the lack of banded amphibolites without clinopyroxene samples, only sheared amphibolites and mafic schists are compared to the unaltered

protolith. The plot shows depletion of  $K_2O$ ,  $SiO_2$  and  $MgO$  along with an enrichment in  $TiO_2$ ,  $Fe_2O_3$ ,  $P_2O_5$ , and  $MnO$ .  $Na_2O$ ,  $CaO$ , and  $Al_2O_3$  show varying trends of enrichment and depletion.

**Transect 8:** (fig. 19 top)

The isocon plots for transect 8 show enrichment of  $K_2O$ ,  $MgO$ ,  $Al_2O_3$ , and  $SiO_2$  with depletion of  $P_2O_5$ ,  $MnO$ ,  $Fe_2O_3$ , and  $TiO_2$ .  $Na_2O$  and  $CaO$  show no discernable trends.

The general trends for each element across each transect within the shear zone, starting at the most western transect (T5) and moving east (T6) are summarized below. The table indicates E if the majority of the samples are showing enrichment, D if the majority of the samples are showing depletion and N/A if the samples show no discernable trend of enrichment or depletion.

Element	T5	T3	T1	T2	T6	T8
$K_2O$	N/A	D	N/A	E	D	E
$Al_2O_3$	D	E	E	E	N/A	E
$SiO_2$	E	E	D	D	D	E
$TiO_2$	D	N/A	D*	D	E	D
$Fe_2O_3$	D	N/A	D*	N/A	E	D
$P_2O_5$	D	N/A	N/A	N/A	E	D
$Na_2O$	E	N/A	N/A	N/A	N/A	N/A
$MnO$	N/A	N/A	D	E	E	D
$MgO$	D	N/A	N/A	N/A	D	E
$CaO$	N/A	N/A	E	N/A	N/A	N/A

Table 1. Table showing enrichments/depletions of elements as compared to each transect's protolith across each transect.

E=enriched

D=depleted

N/A=no trend

\*in MCS samples only

In summary, as evident in Table 1, the results of method 1 show very contrasting trends across each transect and fail to provide any consistent depletion or enrichment trends.

These contrasting trends, especially for  $K_2O$ ,  $TiO_2$ , and  $SiO_2$ , prompted analysis of the geochemical nature of the protoliths across the length of the shear zone. Major element changes were analyzed separately within the banded amphibolite with cpx domain (protolith), starting at the westernmost transect (T5) toward the east (T8). By analyzing the protolith samples across each of these transects, we can determine how similar or different the chemistry of this domain is across strike, which is of vital importance for interpreting the isocon plots. The distance between each transect is approximate, determined from Google Earth, and spans a total of ~40km from west to east.

There are three datasets in this analysis for all elements: 1) the sample collected from the top of each transect and used in the isocon plots (dark green points connected with the line), 2) previous data collected by Castro et al., (1996) (orange points) and 3) the remaining samples from T1 and T2 collected with the others, but not used in the isocon plots (yellow dots). The reason for using the second and third data points is to determine how representative the chemistry of the first data set is.

From these plots (fig. 13) it is clear that there are contradicting trends in the protolith samples across transect, most prominently in  $K_2O$ ,  $SiO_2$ , and  $TiO_2$ . For reference, the mean MORB composition is added to each graph to compare the validity of each protolith (Gale et al., 2013). For example, T3 and T6 have a protolith that seems to be relatively enriched in  $K_2O$  compared to the average MORB, which explains why the rest of the samples of each transect are showing depletion trends in their isocon plots (figs. 16 top and 18 top). On the other hand, protolith samples in T2 and T8 fall within close range of the average MORB value and therefore the  $K_2O$  enrichment trends in each isocon (figs. 15 top and 19 top) are considered more reliable than the depletion trends of T3 and T6. Similarly when analyzing  $SiO_2$  across each transect we see that T3 and T8 have protoliths depleted in  $SiO_2$  compared to the mean MORB content, which explains why the isocon trends for these transects show  $SiO_2$  enrichment patterns in all samples compared to the protolith (figs. 16 top and 19 top). The protolith for T6 is depleted and T8 is enriched in  $TiO_2$  compared to the average MORB, which explains why the T6 isocon displayed strong enrichment trends and why T8 displayed strong depletion trends compared to their protoliths (figs 18 top and 19 top).

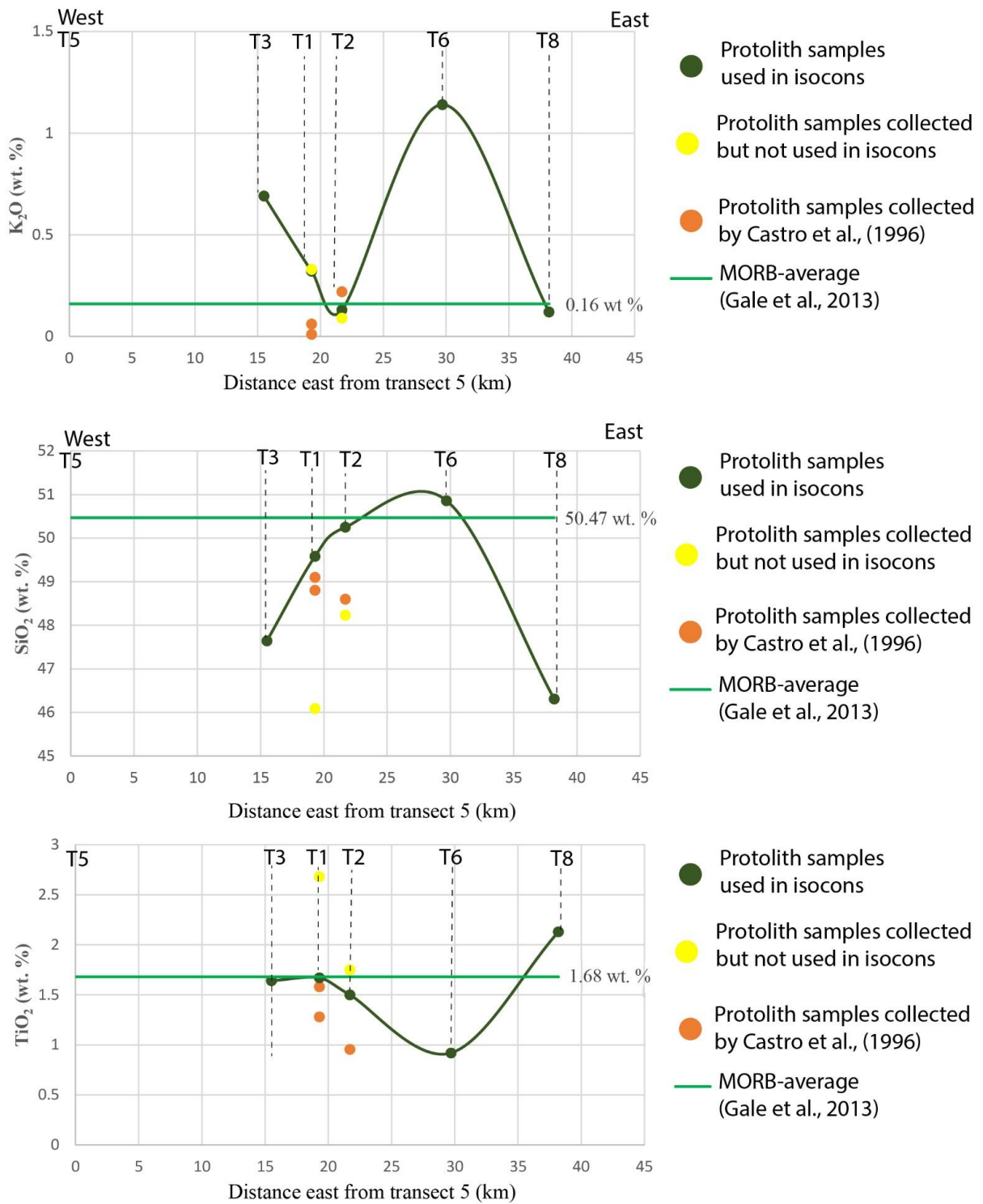


Figure 13. Plots showing element variation within the protolith samples across the length of the shear zone. Top:  $K_2O$  variation across transects. Middle:  $SiO_2$  variation across transects. Bottom:  $TiO_2$  variation across transects. Transect 5 does not have a protolith sample and is therefore excluded.

From this it is clear that the geochemical nature of the protolith is not consistent across the length of the shear zone and comparing the remaining samples in each transect to their local protolith may not give accurate geochemical trends. To obtain clearer results, each transect is compared to the same standardized protolith. Previous publications (Bard, 1969) have attributed the Acebuches amphibolite series to a tholeiitic ocean-basalt protolith (MORB), which prompted the comparison to MORB, as averaged over 422 samples (Gale et al., 2013) (figs. 14-19 middle). To compare each element correctly to this average MORB data, the  $\text{Fe}_2\text{O}_3$  values were converted to FeO (as published in Gale et al., 2013). This changes our isocon plots to produce more consistent geochemical trends across the length of the shear zone (figs 14-19 middle).

**Transect 1** (*fig. 14, middle*)

Transect 1 shows enrichment of  $\text{K}_2\text{O}$  and  $\text{Al}_2\text{O}_3$  with depletion of  $\text{SiO}_2$ .  $\text{MnO}$  and  $\text{TiO}_2$  show depletion trends within the MCS only.  $\text{P}_2\text{O}_5$ ,  $\text{Na}_2\text{O}$ ,  $\text{MgO}$ ,  $\text{FeO}$ , and  $\text{CaO}$  show varying trends of enrichment and depletion.

**Transect 2** (*fig. 15, middle*)

Transect 2 shows enrichment of  $\text{K}_2\text{O}$  and  $\text{Al}_2\text{O}_3$  with depletion of  $\text{SiO}_2$  and  $\text{TiO}_2$ .  $\text{P}_2\text{O}_5$ ,  $\text{Na}_2\text{O}$ ,  $\text{MnO}$ ,  $\text{MgO}$ ,  $\text{FeO}$ , and  $\text{CaO}$  show varying trends of enrichment

and depletion. MnO and Na<sub>2</sub>O may be considered depleted and enriched, respectively, however due to their proximity to the line this is not a strong trend.

**Transect 3** (*fig. 16, middle*)

The trends within transect 3 now contradict the original isocon trends produced when compared to the protolith. Instead of a strong K<sub>2</sub>O depletion, trends now display a strong enrichment that follows the trends of the other transects. This enrichment is accompanied with an enrichment of Al<sub>2</sub>O<sub>3</sub> with depletion of SiO<sub>2</sub> and CaO. P<sub>2</sub>O<sub>5</sub>, Na<sub>2</sub>O, MnO, MgO, FeO, and TiO<sub>2</sub> show varying trends of enrichment and depletion.

**Transect 5** (*fig. 17, middle*)

Transect 5 shows enrichment of K<sub>2</sub>O, FeO, and Na<sub>2</sub>O. P<sub>2</sub>O<sub>5</sub> also shows enrichment trends, however due to their proximity to the line this is not considered a strong trend. MgO, CaO, and SiO<sub>2</sub> show depletion trends. MnO, Al<sub>2</sub>O<sub>3</sub>, and TiO<sub>2</sub> show varying trends of enrichment and depletion.

**Transect 6** (*fig. 18, middle*)

Similar to previous transects, transect 6 shows strong enrichment of K<sub>2</sub>O with depletion of SiO<sub>2</sub>. P<sub>2</sub>O<sub>5</sub>, Al<sub>2</sub>O<sub>3</sub>, Na<sub>2</sub>O, MnO, MgO, FeO, CaO, and TiO<sub>2</sub> show varying trends of enrichment and depletion. When only considering the MCS

samples, CaO shows enrichment. The scattered pattern of these samples suggests significant alteration of samples.

**Transect 8** (*fig. 19, middle*)

Transect 8 shows enrichment of K<sub>2</sub>O and FeO and depletion of SiO<sub>2</sub> in most samples. MnO also shows depletion trends however due to their proximity to the line this is not considered a strong trend. CaO shows enrichment within MCS only. P<sub>2</sub>O<sub>5</sub>, Na<sub>2</sub>O, MgO, Al<sub>2</sub>O<sub>3</sub>, and TiO<sub>2</sub> show varying trends of enrichment and depletion.

The general trends within of each element across each transect within the shear zone, starting at the westernmost transect (T5) and moving east (T6) are summarized below. The table indicates E if the majority of the samples are showing enrichment, D if the majority of the elements are showing depletion and N/A if the samples show no discernable trend of enrichment of depletion.

Element	T5	T3	T1	T2	T6	T8
K <sub>2</sub> O	E	E	E	E	E	E
Al <sub>2</sub> O <sub>3</sub>	N/A	E	E	E	N/A	NA
SiO <sub>2</sub>	D	D	D	D	D	D
TiO <sub>2</sub>	N/A	N/A	D*	D	N/A	N/A
FeO	E	N/A	N/A	N/A	N/A	E
P <sub>2</sub> O <sub>5</sub>	N/A	N/A	N/A	N/A	N/A	N/A
Na <sub>2</sub> O	E	N/A	N/A	E	N/A	N/A
MnO	N/A	N/A	D*	D	N/A	D
MgO	D	D	N/A	N/A	D	N/A
CaO	D	D	N/A	N/A	E*	E*

*Table 2. Table showing enrichments/depletions of elements as compared to average MORB values across each transect.  
E=enriched  
D=depleted  
N/A=no trend  
\*in MCS samples only*

As you can see from Table 2 the most consistent trend across each transect is depletion of SiO<sub>2</sub> and enrichment of K<sub>2</sub>O.

The third method uses the average protolith in order to determine a representative protolith as discussed above. Five steps were performed to find the composition of the representative protolith: 1) All of the samples collected in the two upper banded amphibolite domains were grouped into an excel file. 2) The average of each element across all of the upper banded amphibolite samples was calculated, regardless of the location of the sample across the structure and regardless of whether they were folded or not. 3) A standard deviation (one standard deviation) calculation was performed in excel for each element. From this standard deviation value, upper and lower limits were put into place (upper limit=average element composition + standard deviation, lower limit= average element composition – standard deviation). 4) Any element values that were outside of these upper and lower limits were discarded. 5) Once all of the outlying samples were eliminated, a new average was calculated from the remaining values and deemed the representative composition. The average values for each element after the standard deviation correction do not differ from the average obtained prior to the standard deviation correction, except for K<sub>2</sub>O, in which the most enriched

(or contaminated) protoliths were omitted. The average of the protoliths before and after standard deviation removal are shown in Table 3.

	Na <sub>2</sub> O	MgO	Al <sub>2</sub> O <sub>3</sub>	SiO <sub>2</sub>	P <sub>2</sub> O <sub>5</sub>	K <sub>2</sub> O	CaO	TiO <sub>2</sub>	Fe <sub>2</sub> O <sub>3</sub>	MnO
Average 1 (wt. %)	3.18	7.20	14.97	49.44	0.21	0.26	10.27	1.63	10.85	0.18
# included in average 1	22	22	22	22	22	22	22	22	22	22
Standard deviation (wt. %)	0.63	0.87	0.84	1.28	0.07	0.28	1.28	0.36	1.44	0.03
Range top (wt. %)	3.81	8.07	15.80	50.71	0.28	0.54	11.55	2.00	12.29	0.21
Range bottom (wt. %)	2.55	6.32	14.13	48.16	0.13	0.02	8.99	1.27	9.41	0.15
# omitted	6	6	4	4	4	3	5	7	5	4
Average 2 (protolith) (wt. %)	3.03	7.03	14.96	49.46	0.21	0.16	10.12	1.56	10.79	0.18
# included in average 2	16	16	18	18	18	19	17	15	17	18

Table 3. Shows elemental averages before (Average 1) and after std dev. Correction (Average 2). For most elements these averages are similar, except for K<sub>2</sub>O which was reduced.

The average after the standard deviation removal were used for isocon plots (figs. 14 to 19 bottom). These trends show similar results to method two (MORB protolith):

**Transect 1** (fig. 14 bottom)

Transect 1 shows enrichment of K<sub>2</sub>O and Al<sub>2</sub>O<sub>3</sub> with depletion of SiO<sub>2</sub>. MnO and TiO<sub>2</sub> show depletion trends within the MCS only. P<sub>2</sub>O<sub>5</sub>, Na<sub>2</sub>O, MgO, FeO, CaO show varying trends of enrichment and depletion.

**Transect 2** (*fig. 15 bottom*)

Transect 2 shows enrichment of  $K_2O$ ,  $Al_2O_3$ , and  $CaO$  with depletion of  $TiO_2$  and  $Fe_2O_3$ .  $P_2O_5$ ,  $Na_2O$ ,  $MnO$ ,  $MgO$ , and  $SiO_2$  show varying trends of enrichment and depletion.

**Transect 3** (*fig. 16 bottom*)

The trends within transect 3 show  $K_2O$ ,  $Al_2O_3$ , and  $MnO$  enrichment with  $SiO_2$  depletion.  $P_2O_5$ ,  $Na_2O$ ,  $MgO$ ,  $CaO$ ,  $Fe_2O_3$ , and  $TiO_2$  show varying trends of enrichment and depletion.

**Transect 5** (*fig. 17 bottom*)

Transect 5 shows enrichment of  $Na_2O$ , and  $K_2O$  with a depletion of  $MgO$  and  $Al_2O_3$ .  $MnO$ ,  $CaO$ ,  $SiO_2$ ,  $Fe_2O_3$ ,  $P_2O_5$  and  $TiO_2$  show varying trends of enrichment and depletion.

**Transect 6** (*fig. 18 bottom*)

Transect 6 shows strong enrichment of  $K_2O$  with depletion of  $SiO_2$  and  $MgO$ .  $P_2O_5$ ,  $Al_2O_3$ ,  $Na_2O$ ,  $MnO$ ,  $MgO$ ,  $Fe_2O_3$ , and  $TiO_2$  show varying trends of enrichment and depletion. When only considering the MCS samples,  $CaO$  shows enrichment. The strong scattered pattern of these samples suggests significant alteration of samples.

**Transect 8** (fig. 19 bottom)

Transect 8 shows enrichment of  $K_2O$  and  $Fe_2O_3$  in most samples.  $CaO$  shows enrichment within MCS only.  $P_2O_5$ ,  $Na_2O$ ,  $MnO$ ,  $MgO$ ,  $Al_2O_3$ ,  $TiO_2$  and  $SiO_2$  show varying trends of enrichment and depletion.

The general trends for each element across each transect within the shear zone, starting at the most western transect (T5) and moving east (T6) are summarized below. The table indicates E if the majority of the samples are showing enrichment, D if the majority of the elements are showing depletion and N/A if the samples show no discernable trend of enrichment or depletion.

Element	T5	T3	T1	T2	T6	T8
$K_2O$	E	E	E	E	E	E
$Al_2O_3$	D	E	E	E	N/A	N/A
$SiO_2$	N/A	D	D	N/A	D	N/A
$TiO_2$	N/A	N/A	D*	D	N/A	N/A
$Fe_2O_3$	N/A	N/A	N/A	D	N/A	E
$P_2O_5$	N/A	N/A	N/A	N/A	N/A	N/A
$Na_2O$	E	N/A	N/A	N/A	N/A	N/A
$MnO$	N/A	E	D*	N/A	N/A	N/A
$MgO$	D	N/A	N/A	N/A	D	N/A
$CaO$	N/A	N/A	E	E	E*	E*

Table 4. Table showing enrichments/depletions of elements as compared to average protolith values across each transect.

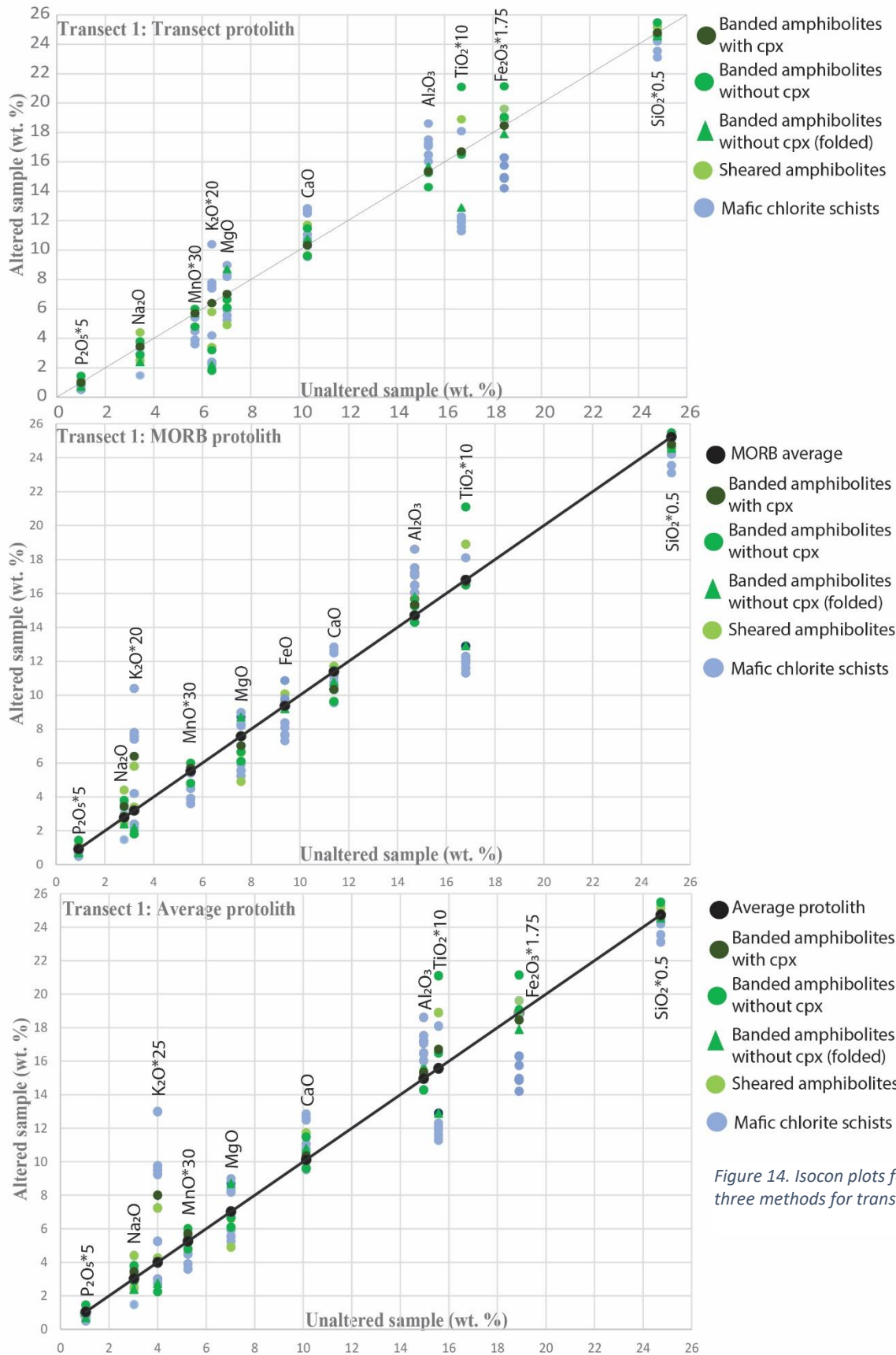
E=enriched

D=depleted

N/A=no trend

\*in MCS samples only

As you can see from Table 4 the most consistent trend across each transect is enrichment of  $K_2O$ , with a more moderate enrichment and depletion of  $Al_2O_3$  and  $SiO_2$ , respectively.



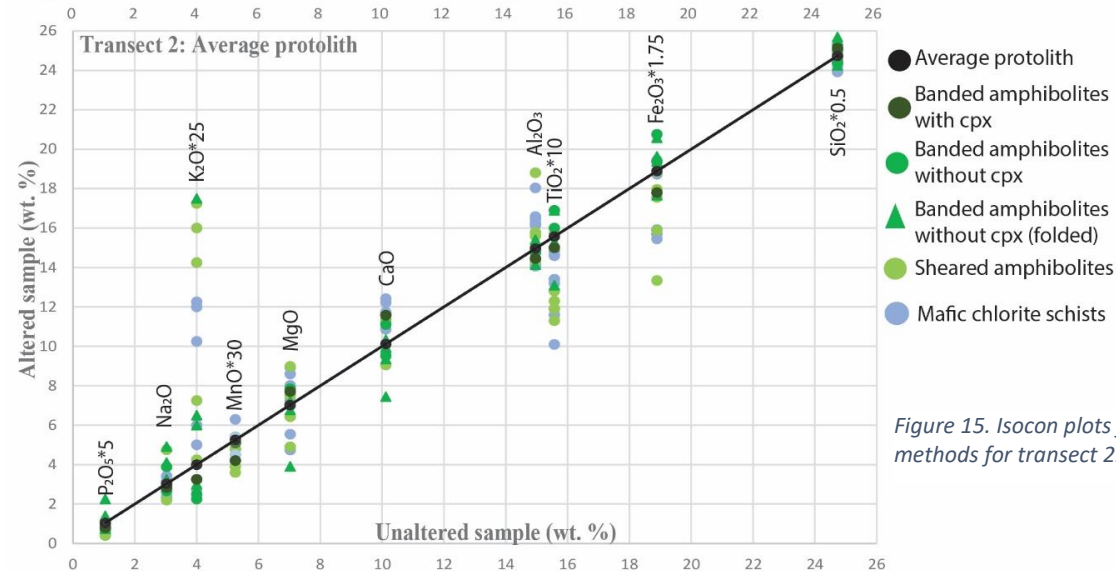
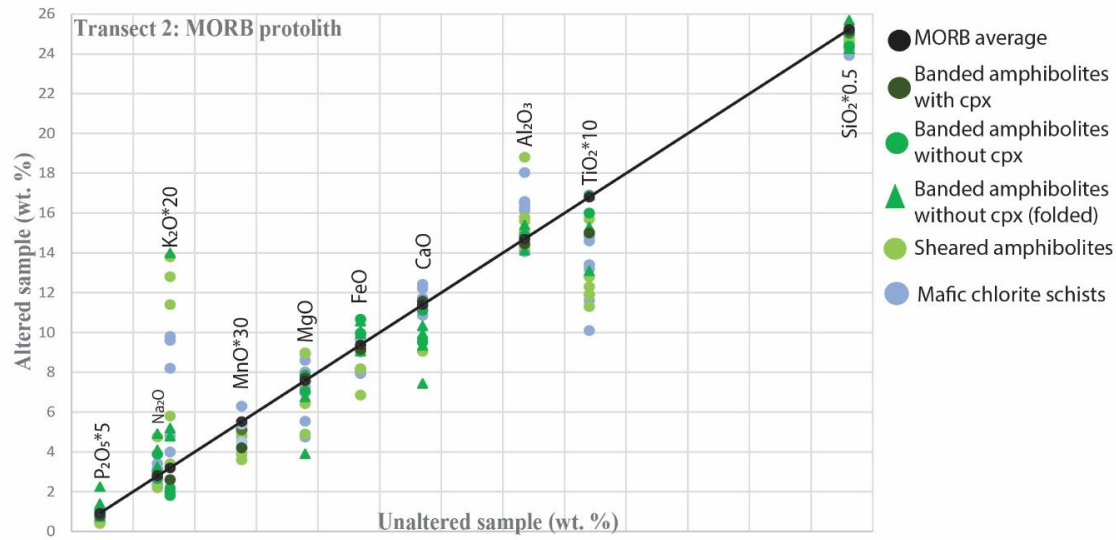
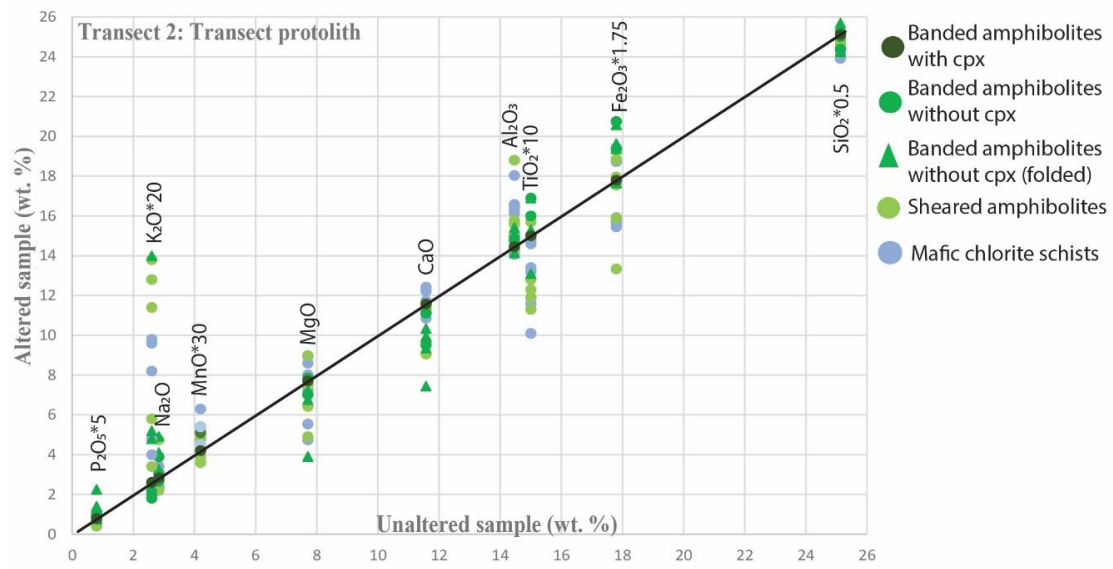


Figure 15. Isocon plots for three methods for transect 2.

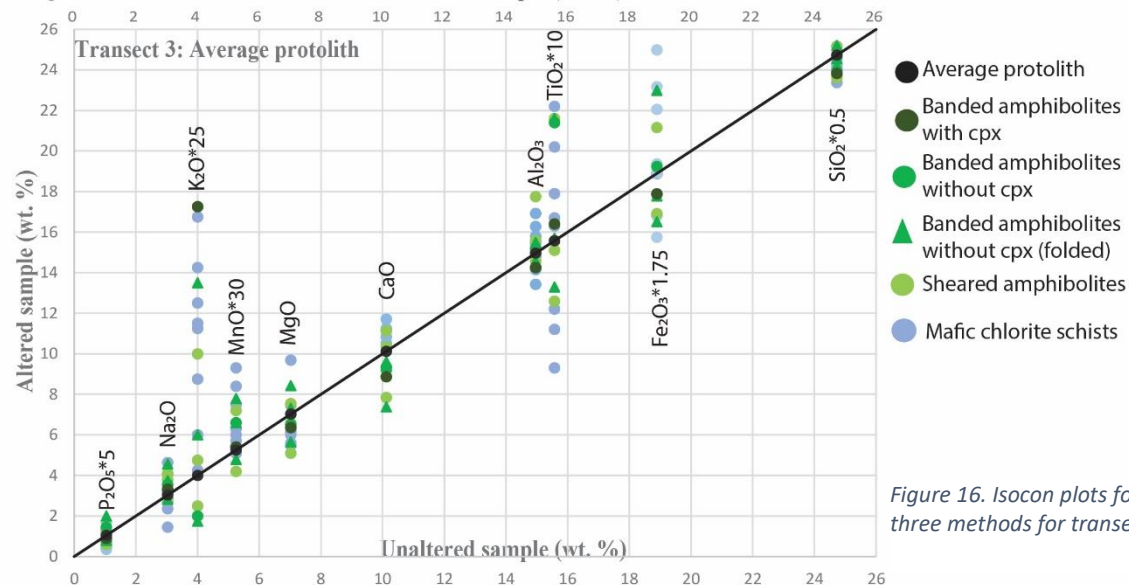
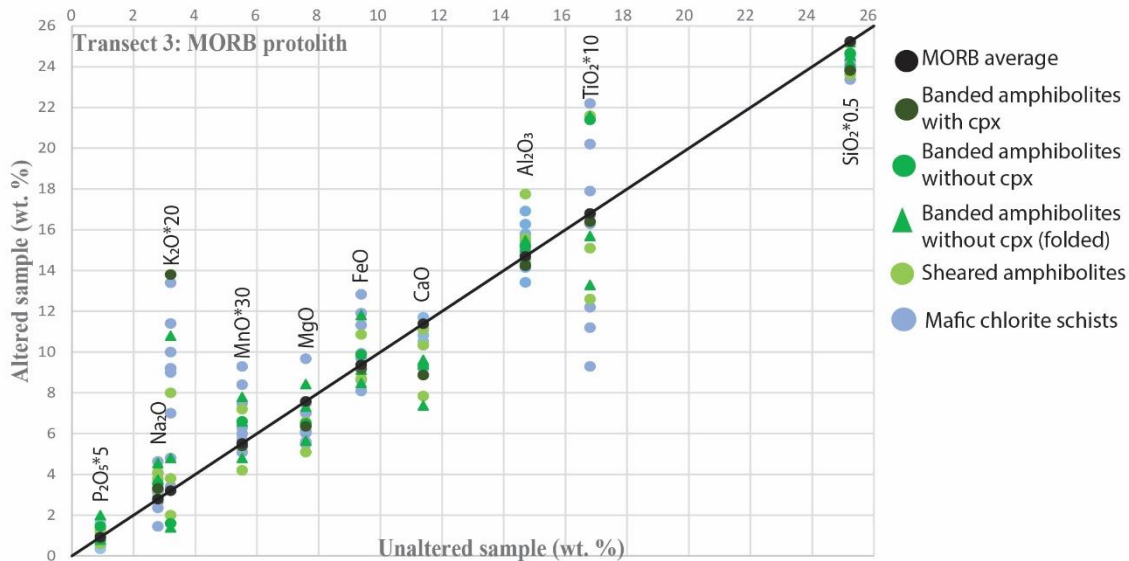
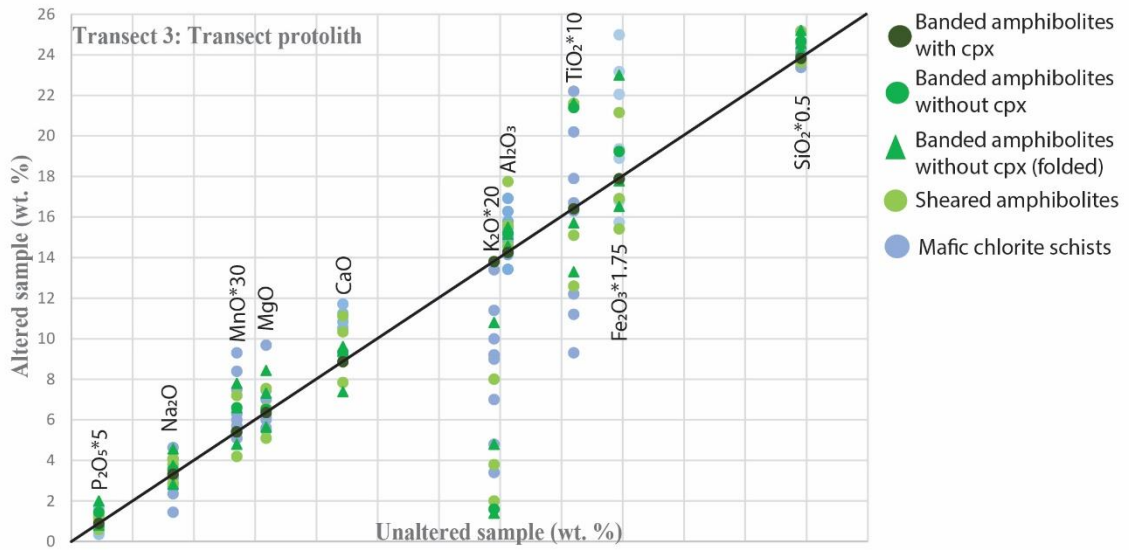


Figure 16. Isocon plots for three methods for transect 3.

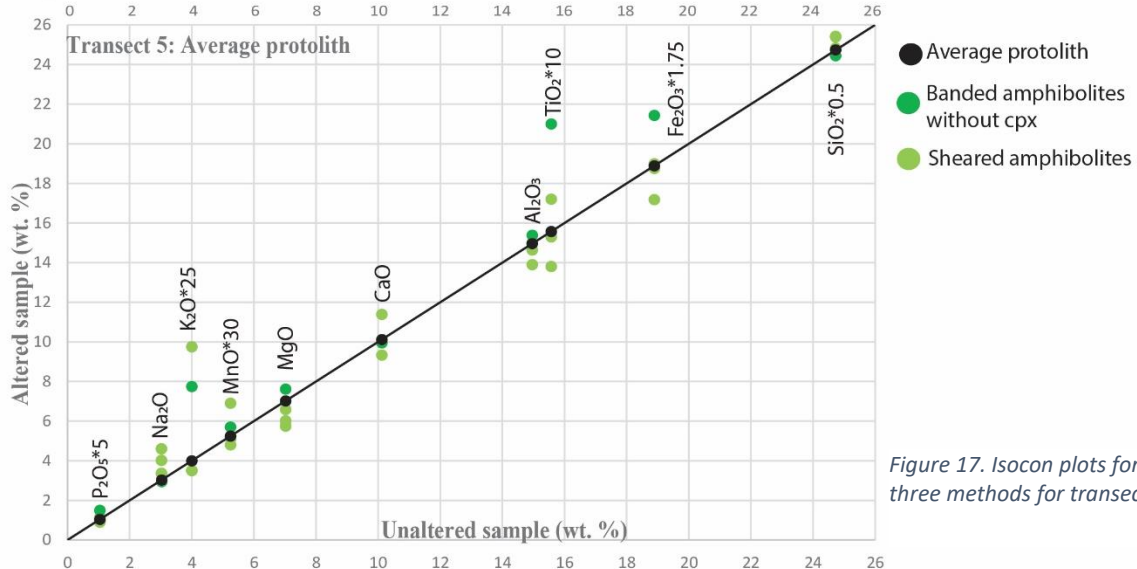
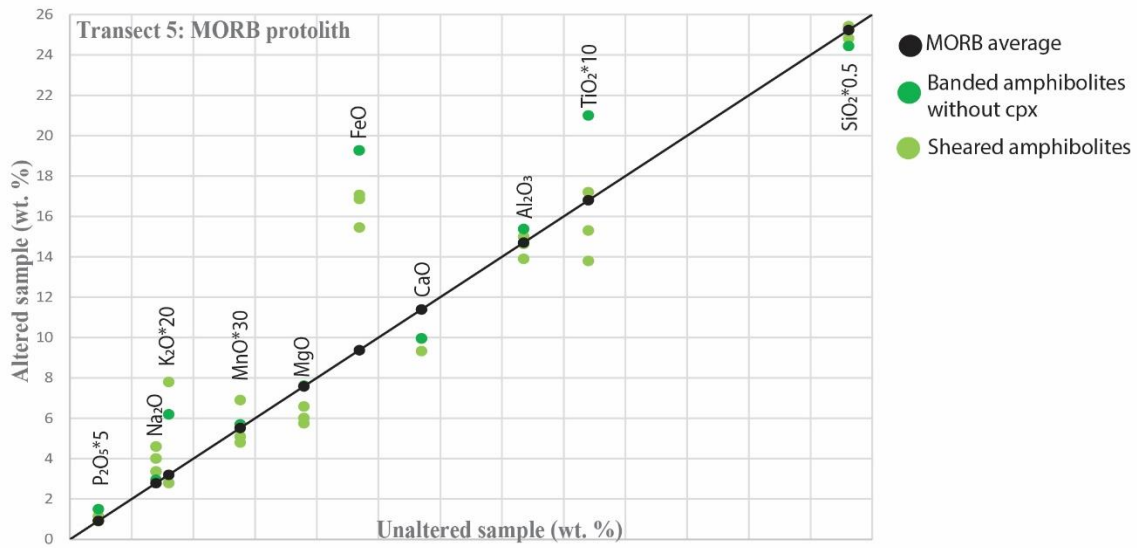
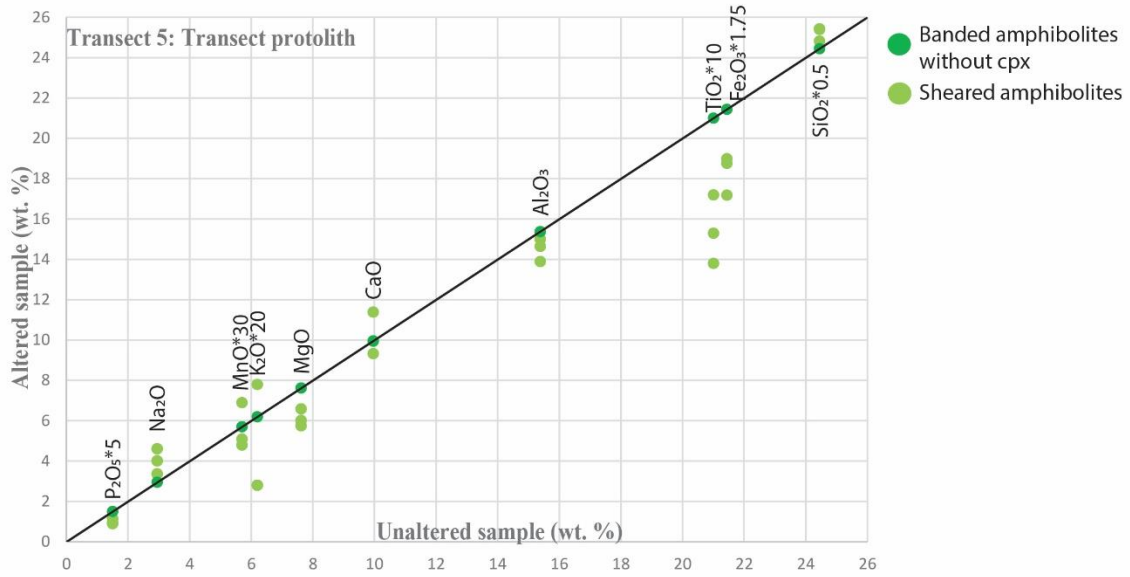


Figure 17. Isocon plots for three methods for transect 5.

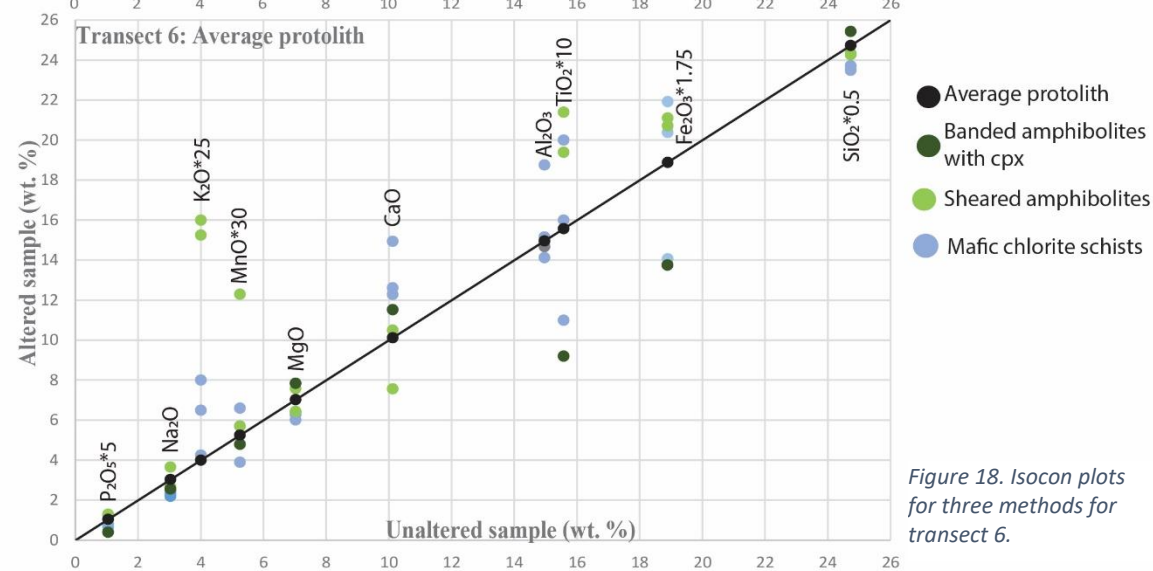
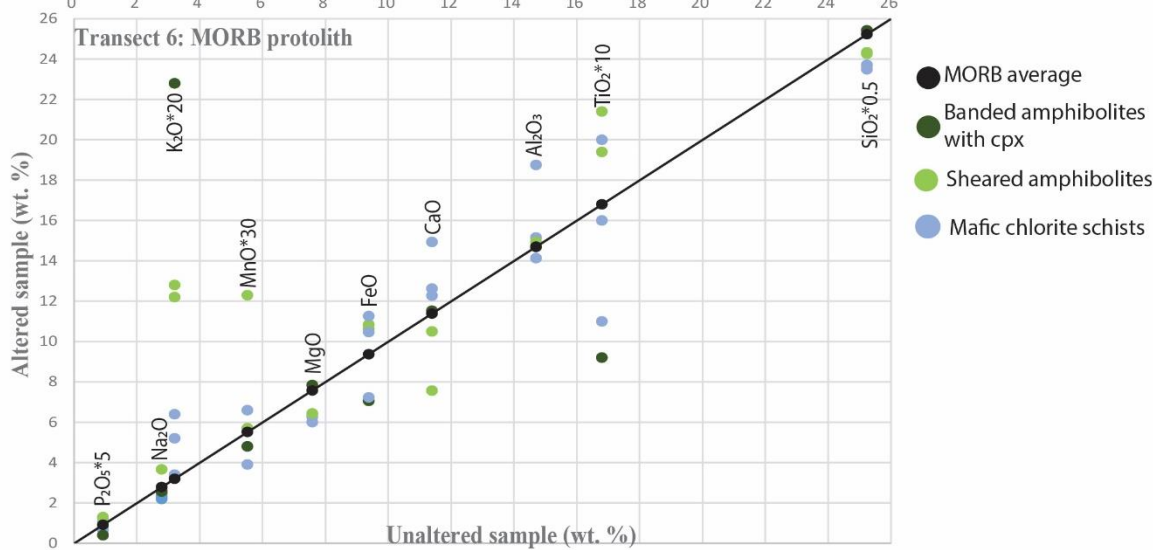
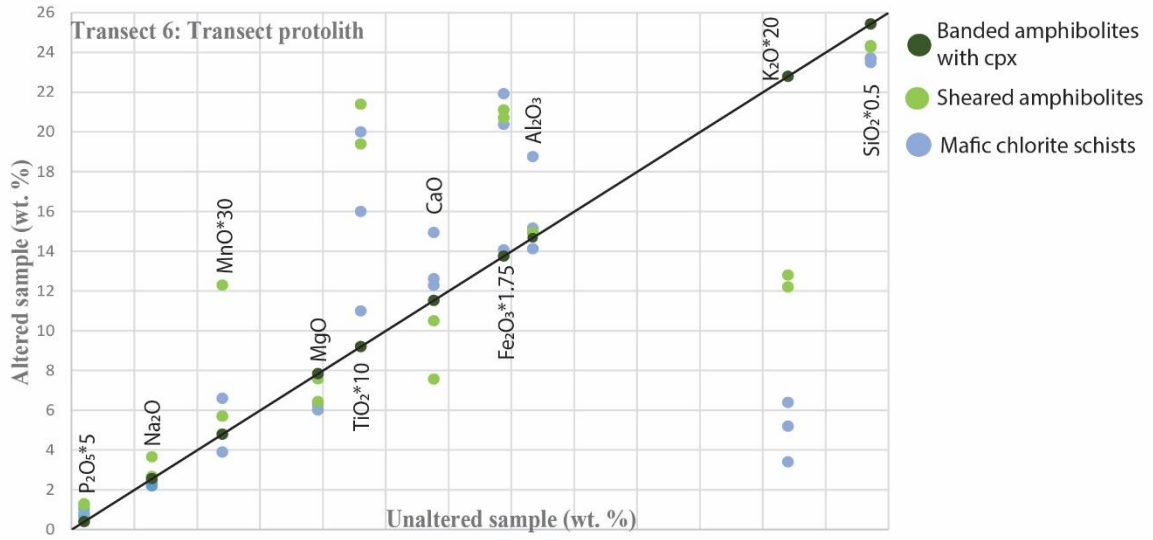


Figure 18. Isocon plots for three methods for transect 6.

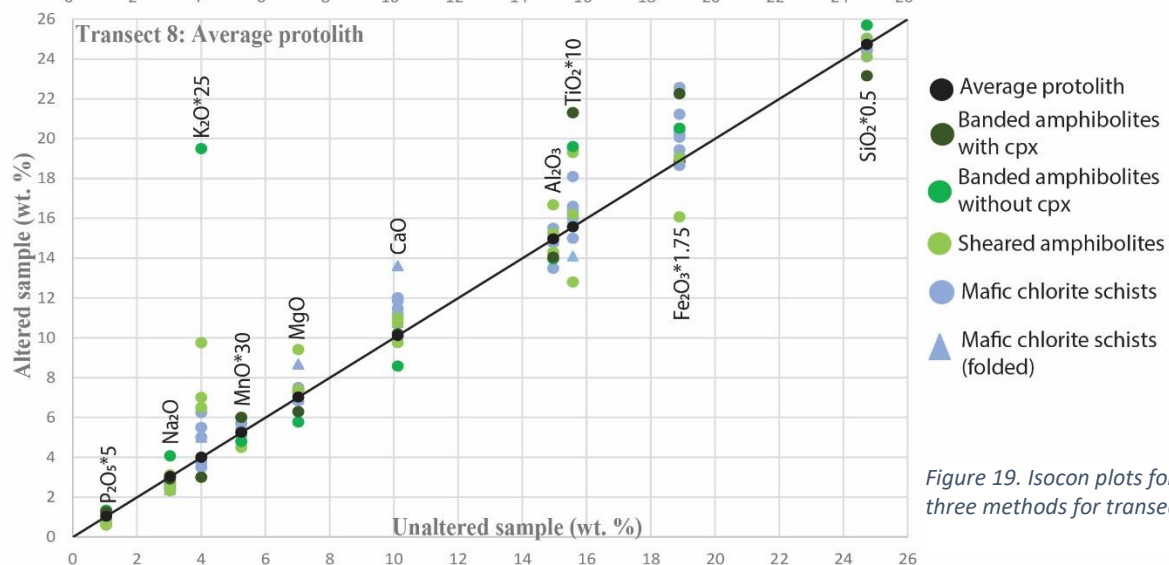
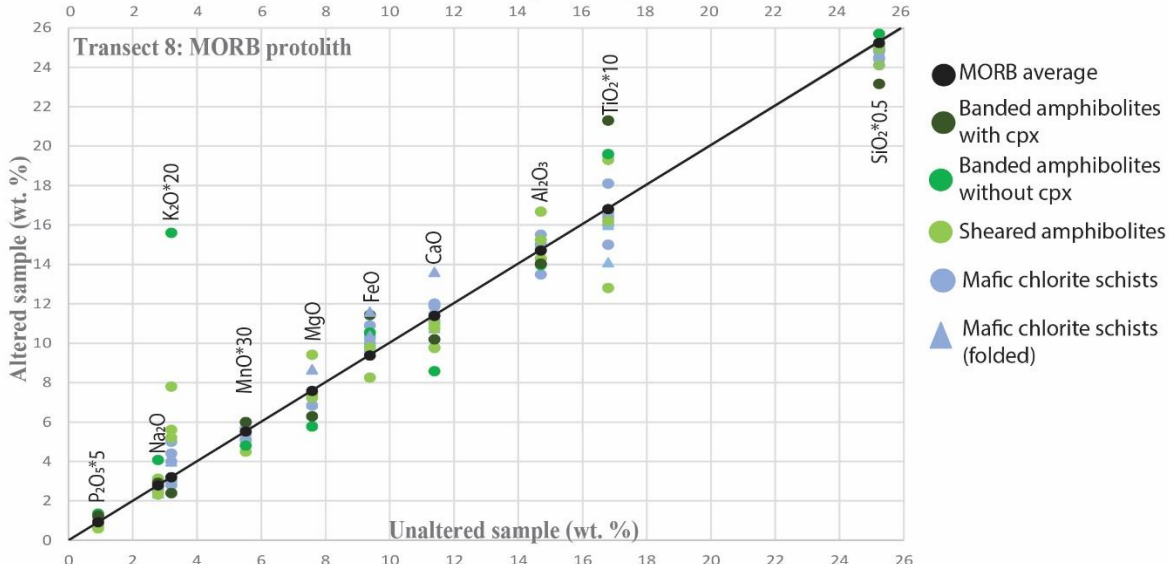
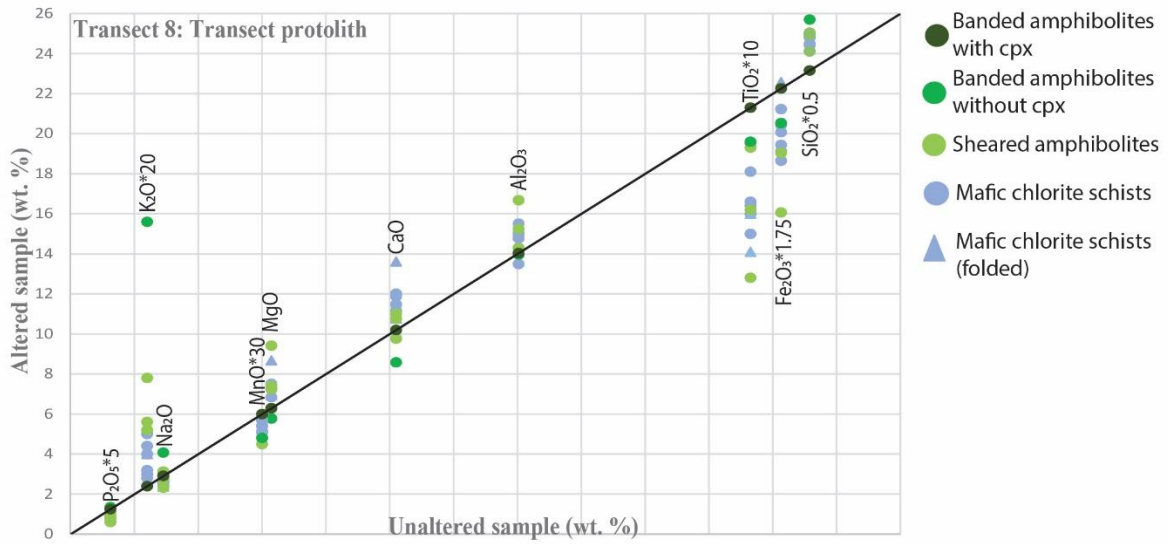


Figure 19. Isocon plots for three methods for transect 8.

## 5. DISCUSSION

### *5.1 Evaluating isocon methods*

For isocon analysis, three methods were used to compare samples to a “protolith.” Three different methods were attempted because in this case, it is not obvious which is the best protolith or unaltered sample for comparison. First, Method 1 compared samples to the furthest rock from the shear boundary within the upper amphibolite domain within each transect. Therefore, this “protolith” was a different rock for each isocon plot (each transect had a different “protolith”). Next, Method 2 compared the samples of each transect to a standardized protolith, the average MORB (Gale et al., 2013). MORB was selected in concordance with previous publications (Bard 1969, Bard and Moine 1979, Dupuy et al., 1979) that linked the Acebuches Metabasites with MORB-affinity. This MORB geochemistry published by Gale et al., (2013) uses FeO whereas the geochemistry in this study uses Fe<sub>2</sub>O<sub>3</sub>. Our Fe<sub>2</sub>O<sub>3</sub> values were converted to FeO for accurate comparison to the MORB geochemistry. Finally, Method 3 compared the samples to a calculated average composition of the upper D1-amphibolite domains. This average was calculated by using all of the concentrations of the D1 rocks except those outside the standard deviation.

In some cases, Method 1 produces opposite trends between transects (e.g.  $K_2O$  enrichment in transects 2 and 8 and depletion in transects 3 and 6) because of protolith variability. This method allowed recognition of the substantial differences between D1 “protolith” samples, particularly for  $K_2O$ . However, it does not offer a dependable way to evaluate shear zone related changes in composition. Methods 2 and 3 give more consistent results because all samples are compared to a standard “protolith.” Regardless of which is used, they show consistent trends across the length of the shear zone.

When only considering Methods 2 and 3, all transects show, most prominently, a strong enrichment in  $K_2O$  and moderate depletion of  $SiO_2$ . There may also be weak enrichment in  $Al_2O_3$ , which is apparent in transects 1, 2, and 3. When considering Method 3 only,  $CaO$  shows enrichment in MCS samples compared to the average protolith in all transects except one (T5). In method 2 the  $CaO$  content shows enrichment in MCS samples in transects 6 and 8, depletion in T3 and T5 and no trends in T1 and T2. Both of these methods show depletion of  $TiO_2$  in D2 samples across transects 1 and 2, which are both located in the central portion on the shear zone. Method 3 shows depletion of  $Fe_2O_3$  in transects 1 and 2 but also shows enrichment in transect 8. All other elements show variable trends.

There have been numerous studies performed on shear zones, all of which produce varying results in response to shearing of various protoliths. For example,

shear zones cutting granitic rocks in various localities show increasing, constant, or decreasing SiO<sub>2</sub> contents with increasing deformation (e.g Beach, 1976, Vocke et al, 1987, O'Hara, 1988, respectively). All other elements show similarly variable behavior from one shear zone to another. It is clear that geochemical changes in shear zones are not straight-forward, and that chemical variation within a shear zone is a product of varying protoliths, fluid composition and source (internal or external), and the P-T conditions under which shearing occurred. While many elements in this study vary across the shear zone, the strong K<sub>2</sub>O enrichment with moderate Al<sub>2</sub>O<sub>3</sub> enrichment and moderate SiO<sub>2</sub> depletion are consistent across all transects using methods 2 and 3. This consistency suggests similar fluid composition and fluid source, protolith, P-T conditions, and degree of fluid infiltration across the length of the shear zone.

In conclusion, the geochemical trends of the shear zone as shown by three methods of isocon analysis are as follows:

#### Method 1: Transect protoliths

- K<sub>2</sub>O: Increases for T2 and T8, decreases for T3, T6, other transects vary
- SiO<sub>2</sub>: Decreases for T1, T2, and T5, increases for T3, T6 and T8
- Al<sub>2</sub>O<sub>3</sub>: Increases in all transects, except T5
- TiO<sub>2</sub>: Decreases for T1, T2, T5, and T8, increases for T6, varies for T3

- MgO, CaO, Fe<sub>2</sub>O<sub>3</sub>, Na<sub>2</sub>O, MnO, P<sub>2</sub>O<sub>5</sub>: no clear trends

#### Method 2: MORB-average protolith

- K<sub>2</sub>O: Increases
- SiO<sub>2</sub>: Decreases
- Al<sub>2</sub>O<sub>3</sub>: Increases for T1, T2, T3, remaining transects shows no trend
- CaO: Increases for T6 and T8; remaining transects show no trend
- TiO<sub>2</sub>: Decrease in MCS in T1, T2
- MgO, Fe<sub>2</sub>O<sub>3</sub>, Na<sub>2</sub>O, MnO, P<sub>2</sub>O<sub>5</sub>: no clear trends

#### Method 3: Average protolith with standard deviation

- K<sub>2</sub>O: Increases
- SiO<sub>2</sub>: Decreases in 3, 1, and 6, remaining transects show no trend
- Al<sub>2</sub>O<sub>3</sub>: Increases in T1-T3, also increases, although less sharply, in the other transects
- CaO: Increases in all transects, except T3
- TiO<sub>2</sub>: Decrease in MCS in T1, T2
- Fe<sub>2</sub>O<sub>3</sub>: Decrease in T1 and T2, Increase in T8
- MgO, Na<sub>2</sub>O, MnO, P<sub>2</sub>O<sub>5</sub>: no clear trends

## *5.2 Elemental trends*

### *5.2.1 K<sub>2</sub>O*

There is a clear and consistent K<sub>2</sub>O enrichment across all transects of the shear zone. Due to the mobile nature of K<sub>2</sub>O and the unusual enrichment trends not typical of a MORB-derived rock, it is plausible that this K<sub>2</sub>O was transported into the shear zone during fluid infiltration from an external source. Due to the absence of potassium-rich minerals such as biotite or muscovite, it is likely the additional K<sub>2</sub>O is being incorporated into the amphibole and chlorite structures. K<sub>2</sub>O enrichment is consistent across the shear zone, but the degree of K<sub>2</sub>O enrichment varies. The enrichment of potassium across the entirety of the shear zone within all lithologies including those far from the shear zone as far as the upper D1-domains, suggests that fluid infiltration could have spanned across a wider area than originally thought. Minor epidote veins were seen in the D1 domains, which suggest that some very localized fluid infiltration occurred in these areas during D2, but does not explain the K<sub>2</sub>O. Considering the metabasites overthrust a sequence of metamorphosed sediments (accretionary prism of the PdL), it is possible that fluid-rock interaction with these PdL sediments produced the K<sub>2</sub>O and perhaps the Al<sub>2</sub>O<sub>3</sub> that was added to the metabasites.

K<sub>2</sub>O enrichment is particularly important when considering strain softening because K<sub>2</sub>O alteration is expected to increase production of micas, clays, and

chlorite. These phyllosilicate minerals retain water, and therefore the amount of K added partly controls the proportion of H<sub>2</sub>O retained within the rock (Tomkins et al., 2009). This could create a reinforcing feedback for fluid-rock interaction, in which the fluid promotes phyllosilicate production that in turn retains more water for phyllosilicate productions and softens rock, promoting strain localization.

Tomkins et al., (2009) suggests that the typical assemblage of mafic rocks that have not been subjected to K metasomatism is chlorite+plagioclase±quartz±actinolite but states that increasing K alteration promotes the growth of biotite and muscovite at the expense of chlorite. There is no formation of biotite or muscovite in the rocks within the SISZ, which is surprising due to the higher than average K<sub>2</sub>O value. This is most likely because typically potassium-rich phyllosilicates, such as muscovite, biotite, or phengite, have K<sub>2</sub>O values between ~8.01 and ~11.53 wt. % as reported from studies in Deer, Howie and Zussman (2013). While the SISZ samples are enriched in K<sub>2</sub>O compared to their MORB-protolith, they are not necessarily enriched enough for these potassium-dominated minerals to grow. It is more likely that the additional K<sub>2</sub>O was incorporated into the structures of the amphiboles that occur within the SISZ. The amphiboles are more specifically hornblendes, calcic amphiboles (Díaz-Azpiroz 2000). The upper amphibolite domains and the sheared amphibolites are dominated by magnesiohornblendes in which a combination of

edenite and pargasite substitution dominates (Díaz-Azpiroz 2000). The structure of magnesiohornblende does not easily incorporate K, however the edenite and pargasite substitutions replace Si with Al and incorporate Na in an otherwise vacant A-site. More specifically, edenite substitutions commonly replace one Si with an Al, while pargasite substitutions replace two Si for two Al, which is balanced partly by Al for (Mg, Fe) and Na in the A-site. Both of these substitutions introduce Na into the A site, however, it is common for K and Na to be interchangeable and therefore it is possible that the increasing K is being incorporated more readily into these A-sites over Na. This may explain the increase in both of these elements within the protolith domains as the amphibole readily took them in within its structure.

The amphiboles within Mafic Chlorite Schist domains are much more heterogeneous and actinolite, hornblende, edenite, pargasite, and hastingsite coexist (Díaz-Azpiroz 2000). Here, the most important substitution is pargasite, which is accompanied by minor edenite, tschermakite, Fe- and Ti-tschermakite substitutions. All of these amphiboles, except actinolite, are relicts of D1. Díaz-Azpiroz (2000) also documents sporadic potassium feldspar grains within the mafic chlorite schists, which may incorporate some  $K_2O$ ; however, it is not expected that any of these rare K-feldspar samples were sampled in this study.

While there are no obvious geochemical trends occurring for Na<sub>2</sub>O, the plagioclase chemistry seems to get more sodic as we move down the Acebuches structure toward the shear boundary (Díaz-Azpiroz 2000). This is due to the increased stability of Na-rich plagioclase at lower temperatures in the greenschist facies. The presence of sodic plagioclase, more specifically andesine rimmed by oligoclase, and the presence of minor albite in the MCS suggests the Na<sub>2</sub>O remains constantly bound within the plagioclase structure, allowing K to substitute easily in the typical Na-occupied A-site of the amphiboles.

#### 5.2.2 Al<sub>2</sub>O<sub>3</sub>:

Using method 1 we see enrichment trends for Al<sub>2</sub>O<sub>3</sub> in all transects, except for T5, which shows depletion. Method 2 shows enrichment in transects 1, 2, and 3, with varying trends in 5, 6, and 8. Method 3 shows enrichment in transect 1, and 2, with varying trends in the remaining transect. From this it is clear that there is a consistent enrichment in transects 1 and 2 using all three methods. The distance plots also show steady enrichment across domains 1-3 and a chaotic, spiked character of Al<sub>2</sub>O<sub>3</sub> within the MCS. This chaotic spiked geochemical pattern, most noticeable in transect 2 and 3, is a common indication of kilometer scale dissolution and transport (O'hara and Blackburn 1989, Goddard and Evans 1995).

The overall enrichment of  $\text{Al}_2\text{O}_3$  across the strain gradient within the transects could be because either 1) The immobile nature of  $\text{Al}_2\text{O}_3$  reveals a relative enrichment after loss of more mobile constituents toward the shear boundary or 2) The banded amphibolites from the top of the structure, that preserve the HT/LP D1 deformation, are depleted in aluminum compared to the rocks toward the shear contact. Aluminum is assumed to be immobile during fluid-rock interaction and therefore  $\text{Al}_2\text{O}_3$  is often used to determine the slope line for isocon plots (e.g. Grant 1986, Ferry 1987). Beitter et al., (2008) argue, however, that Al can be mobile within medium-high grade metamorphic rocks, and that sufficient amounts of Al can be transported in medium-to high grade metamorphic fluids. The fluid expulsions during the dehydration of these rocks during the D1 HT/LP metamorphism could have carried  $\text{Al}_2\text{O}_3$  out of the system. Bebout and Barton (1989) also record Al mobility on a local scale. Since we do not know the origin and composition of the fluid considered in this study, this remains uncertain.

### 5.2.3 $\text{SiO}_2$

The depletion of  $\text{SiO}_2$  in transects 3, 1, and 6 suggests fluid moving through the shear zone removed  $\text{SiO}_2$  from the system. If so, the incoming fluid would have been undersaturated in silica. The removal of Si may promote some of the edenite or pargasite substitutions, by prompting removal of Si in order for the Al to easily

replace Si. By promoting this substitution it may also be promoting the incorporation of K into the A site.

#### 5.2.4 *CaO*:

CaO shows varying patterns of enrichment and depletion, however, all mafic chlorite schists are enriched across all samples compared to the protolith in most transects (except T5) of the shear zone using method 3. Certain minerals may increase the CaO content within the MCS, such as epidote and the various calcic-amphiboles present. The Ca necessary for epidote formation was probably released from the An-rich plagioclase as they became more unstable at lower temperatures toward the shear zone.

#### 5.2.5 *TiO<sub>2</sub>*

TiO<sub>2</sub> shows depletion trends in the MCS domain in transects 1 and 2 across all three isocon methods. In the distance plot, transect 1 shows depletion of TiO<sub>2</sub> at the amphibolite/mafic chlorite schist transition boundary, and transect 2 shows a more gentle decrease with distance from the top of the structure. Due to the immobile nature of TiO<sub>2</sub>, it is frequently used as an immobile element for 1:1 lines on isocon plots (Goddard and Evans, 1995). Not only would we expect this element not to move into solution, but it is common to see a relative enrichment in TiO<sub>2</sub> within altered rocks due to the loss of more mobile elements from the system, which is not apparent across any of the transects.

Díaz-Azpiroz (2000) documented a titanite-present lithology that sometimes exists between the banded amphibolites without clinopyroxene and the sheared amphibolites. From highest to lowest grade within the banded amphibolites that preserve D2 deformation, he documents: banded amphibolites with clinopyroxene, banded amphibolites without titanite and without clinopyroxene, and banded amphibolites with titanite and without clinopyroxene. This minor lithology was not considered important before sampling, and therefore was not a rock domain used here. It may have been sampled within rock domain 2, banded amphibolites without pyroxene. If this is the case, the high content of titanium within titanite would produce plots in which the banded amphibolites are enriched compared to samples toward the shear zone boundary, which is observed in transect 1. A large spike of titanium within transects 1 and 2 occur in the banded amphibolites without clinopyroxenes, and therefore these samples may be this titanite rich lithology. Transect 8's protolith is the most enriched in titanium, which is related to the HT/LP metamorphic event that exceeded the titanite-out isograd and subsequent movement of titanium into ilmenite and magnetite grains (Díaz-Azpiroz, 2000). In this model, during the HT/LP metamorphic event, the titanite phase was reduced to form ilmenite.

(1) Oxidized mafic phase+ttn=reduced mafic phase+Ilm+O<sub>2</sub>.

This does not explain why T1 and T2 show depletion patterns compared to the MORB protoliths (figs 14 and 15 middle).

### ***5.3 Data limitations***

It is important to note certain limitations when it comes to the reliability of each transect's data. Starting at the western end of the shear zone, due to lack of outcrop, transect 5 contains limited samples and subsequently limited domains. Transect 5 only contains 4 samples from only two domains (banded amphibolite without clinopyroxene and sheared amphibolites). Since this transect contains neither the "protolith" nor the most deformed domain, mafic chlorite schists, the data from this transect is not considered strong nor reliable.

Transect 3 contains 17 samples, including samples from each of the four domains. For the most part, transect 3 has a continuous, gradational strain gradient (low to high) apart from a few appearances of sheared amphibolites that appear within the mafic chlorite schist domain.

Transects 1 and 2 are well exposed transects that allowed sufficient sampling across all four domains. Transect 1 offered a gradational, consistent strain gradient from low to high strain toward the shear zone. Transect 2, like transect 3, has a gradational strain gradient (low to high) apart from a few appearances of sheared amphibolites that appear within the mafic chlorite schist domain.

Transect 6 is a limited sample transect, with 6 samples covering 3 of the domains (minus the protolith). Transect 8 is a densely sampled transect that covers all four domains and offers a consistent strain gradient. However, it contains areas that are highly folded.

Each domain has a different grain size, which grades from coarse (2mm) in the banded amphibolites with clinopyroxene at the top of the structure, medium grained (1-2mm) in the banded amphibolites without clinopyroxene, <1mm in the sheared amphibolites and eventually very-fine grained in the mafic chlorite schists at the shear contact. Because of this difference in grain size, each domain requires a different powdered sample amount in order for the XRF results to be representative of the bulk composition of the rock. For the coarser-grained rocks at the top of the structure more grains are required in order for the powdered sample to be representative of the bulk. For example, certain elements (Ti, P) are tied to particular trace phases, such as apatite. If the trace phase is not included in the powdered sample, the abundances of the associated elements are decreased. Due to the large sample required for the coarse-grained rocks and the difficulty of obtaining a powdered sample due to the solid nature of the rock, certain discrepancies may be present in the data for such elements. The sheared amphibolite and mafic chlorite schist domains are fine-grained, and therefore there is more certainty associated with the representative-nature of the samples. When

the average of the upper banded amphibolite domains was calculated, it fell in very close range to the values of MORB-geochemistry, which suggests the samples obtained in the coarse-grained domains are sufficient.

#### ***5.4 Major element changes and metamorphic reactions, structural fabrics, and distance from shear zone***

The most obvious trends across the shear zone are enrichment in  $K_2O$ ,  $Al_2O_3$  and  $CaO$  with depletion in  $SiO_2$ . The next step is to consider where these changes occur with regards to the lithology of the shear zone.

$Al_2O_3$  is enriched in transects 1, 2, and 3. The distance graph (fig. 7a) for transect 1 indicates that this increase in  $Al_2O_3$  occurs right at the transition between sheared amphibolites and mafic chlorite schists. Transects 2 and 3 (figs. 8a and 9a) also suggest that the increase occurs at this boundary as they display relatively stable chemical trends, denoted by a relatively flat line, until the pattern changes to chaotic and spiked at the mafic chlorite schist boundary. This chaotic geochemical pattern is usually indicative of fluid-interaction and suggests that much of the  $Al_2O_3$  alteration occurs within this lithology.

$SiO_2$  is depleted across transects 1, 3, and 6. In transect 1 (fig. 7a) most of the  $SiO_2$  is lost after the mafic chlorite schist boundary, particularly 100m from the shear contact. Transect 3 (fig. 9a) shows a steady decrease in silica right after the

transition from the banded amphibolites of D1 and the sheared amphibolites of D2. There are a few spikes within the mafic chlorite schist domain, however, most of the silica-lows in the transect are confined to this domain. This suggests that SiO<sub>2</sub> depletion happened primarily in the lithologies that underwent retrograde metamorphism.

CaO is enriched across the easternmost transects 2, 6, and 8 (figs. 8a, 11a, 12a). This enrichment seems to take place at the transition between the D1 and D2 domains, the banded amphibolites with clinopyroxene and the sheared amphibolites. While the geochemical pattern for transects 2 and 8 are chaotic, they show an increase at the onset of the sheared amphibole domain and onwards. Transect 6 shows a clear, steady increase in CaO from the sheared amphibole boundary.

The plots for K<sub>2</sub>O are chaotic and do not appear to show a relationship between enrichment and lithology. It appears that there is no pattern to the K<sub>2</sub>O enrichment, which is random across all domains of the shear zone.

Most of the geochemical changes occur within the domains that underwent retrograde metamorphism, sheared amphibolite and to a greater extent, the mafic chlorite schists. Chlorite and epidote are both present exclusively in the sheared amphibolite and mafic chlorite schist domains, but mostly in the latter. The

retrograde reaction that dominated the mafic chlorite schists was probably:  
Hornblende + fluid → Chlorite + Actinolite + Epidote + Qtz. This fluid-assisted breakdown of hornblende weakened the rock, as the chain-silicate structure of hornblende is much stronger than the phyllosilicate and sorosilicate structures of chlorite and epidote, respectively. Sharp and Buseck (1988) demonstrated that retrograde growth of chlorite in place of amphibole is typically parallel or subparallel to the amphibole orientation. This suggests the growth of chlorite in the SISZ could have been parallel to strike of the shear zone, demonstrated by NW/SE aligned amphiboles. The alignment of chlorites in place of amphiboles could have created a much weaker rock and perhaps lead to strain softening and strain localization. This could be the reason the shear fabrics extend much more broadly into the Acebuches Metabasites relative to the neighboring Pulo do Lobo terrane.

The geochemical trends discussed above, apart from  $K_2O$ , seem to have occurred in these domains where epidote and chlorite were present, suggesting that the increased fluid flow in these areas facilitated in both the weakening of the rock and geochemical alteration.

### ***5.5 Fluid composition***

The geochemical alteration across the shear zone allows us to elucidate the nature of the fluid that moved through the shear zone during the D2 retrograde

metamorphism. The depletion of  $\text{SiO}_2$  across three transects suggests the fluid could have been silica undersaturated. The mobile nature of  $\text{K}_2\text{O}$  and the unexpected enrichment of it in rocks of MORB-affinity suggests the fluids that interacted with the shear zone brought the  $\text{K}_2\text{O}$  from elsewhere. The Acebuches metabasites overthrust the PdL terrane which is interpreted to be a metamorphosed accretionary prism, and therefore it is plausible that the schists of the PdL were a  $\text{K}_2\text{O}$  source. Interestingly, the mafic chlorite schists seem to be enriched in  $\text{CaO}$ , despite the plagioclase becoming more sodic toward the shear boundary.  $\text{CaO}$  is required for the formation of epidote. Moreover, transects 1 and 2, which are located in the center of the shear zone, display depletion trends in  $\text{Fe}_2\text{O}_3$  and  $\text{TiO}_2$  within their mafic chlorite schist domains.

### ***5.6 Fluid pathways***

The  $\text{K}_2\text{O}$ -rich nature of the fluid, along with the possibility that it was also enriched in  $\text{Al}_2\text{O}_3$  and  $\text{CaO}$ , suggest that it may have passed through the PdL terrane prior to interacting with the Acebuches Metabasites. To confirm this, geochemical samples across the PdL terrane would be needed to assess any  $\text{K}_2\text{O}$  depletions related to fluid-interaction. However, determining geochemical changes within the PdL would not be easy due to the heterogeneous nature of the rocks within this domain.

When considering the pathways of fluid flow within shear zones, it is useful to consider the Conduit-Barrier Fluid Flow model (Yonkee et al., 2003) (fig. 20). Typically, when a fluid of any origin moves through a shear zone, it does so in localized pathways. The positive feedback between fluid-flow, metamorphism, and strain softening leads to strain localization, which is often accompanied by the alignment of phyllosilicate minerals. This alignment of phyllosilicates creates a conduit for fluid flow to move in a manner which is parallel to the strike of the shear zone. On the other hand, this alignment of phyllosilicate minerals creates anisotropic impermeability to the rocks on either side of the shear zone and therefore the phyllosilicates act as a barrier for lateral fluid flow (cross-fault flow) (McCaig, 1987, Selverstone et al., 1991, Barton et al., 1995, Caine et al., 1996, Kisters et al., 2000, Barnes et al., 2004). This model is applicable to a variety of conditions including in the shallow crust (Bense and Person, 2006 and Boulton et al., 2016) and in deeper conditions (Yonkee et al., 2013 and Quilichini et al., 2015). By this model, we would expect to see the elemental changes confined to the SISZ, however, there is evidence that the fluid in the SISZ did not behave as localized to the shear zone as expected. The sporadic enrichment of  $K_2O$  across all domains of the shear zone, including the upper amphibolite domains, is evidence for cross-fault flow, which originates from the metamorphosed accretionary prism of the PdL terrane (fig. 20). Yonkee et al., (2003) also documents chemically

altered rocks outside of a shear zone, which he attributes to late fractures that create localized pathways for fluid to reach rocks outside of the shear zone. The greenschist facies metamorphism in the SISZ is associated with temperatures which are close to the brittle-ductile transition zone and therefore it is plausible that late, localized fractures created conduits for lateral fluid flow. This is evident from the seemingly “random” enrichment of particular protolith samples and not others, as well as epidote veins recorded in the upper banded amphibolite domains.

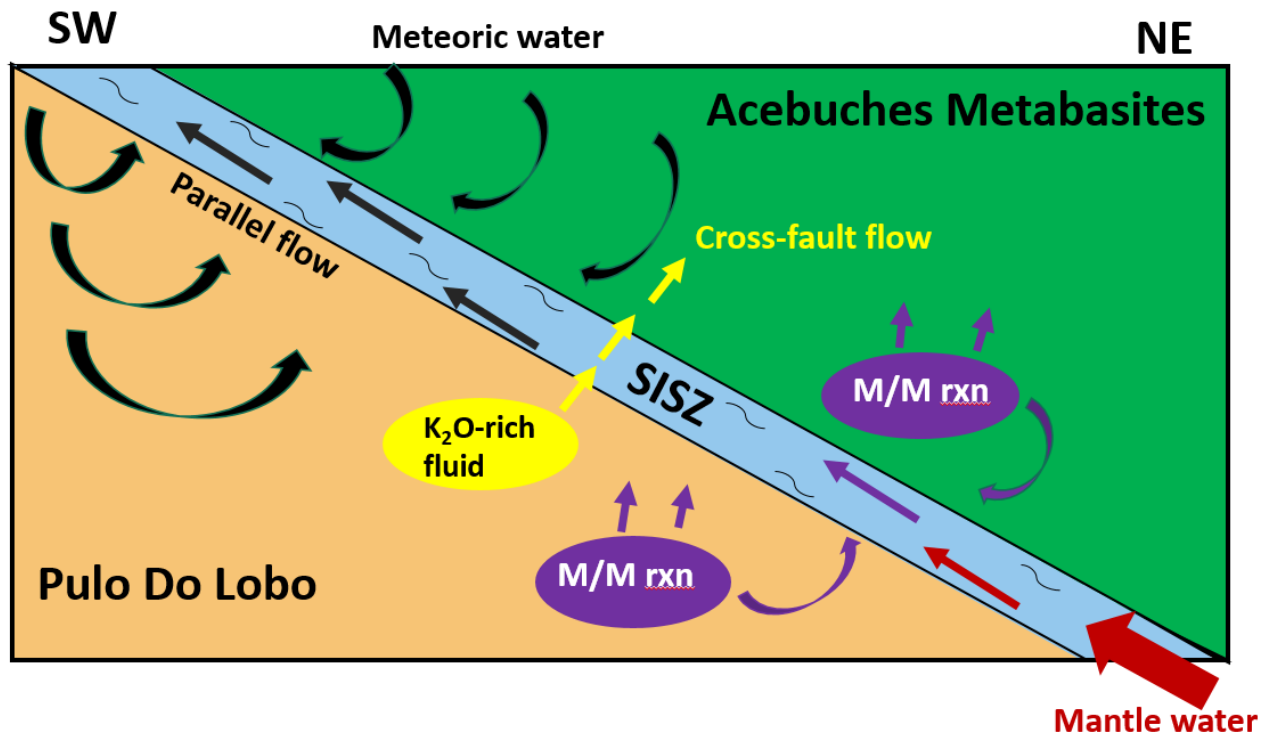


Figure 20. The Conduit-Barrier Fluid flow model. Alignment of phyllosilicates favors parallel fluid flow and limits cross-fault flow.

## 6. CONCLUSION

In summary:

1. The average protolith with standard deviation isocon method yields better and more consistent results than the other two isocon methods tested.
2. Using this method, the clearest geochemical trends across the shear zone are increases in  $K_2O$ ,  $Al_2O_3$ , and  $CaO$  with a decrease in  $SiO_2$ .

The most prominent geochemistry trends of the SISZ document an enrichment in  $K_2O$  with a more moderate increase in  $Al_2O_3$ , along with a moderate depletion of  $SiO_2$ . These enrichment and depletion trends are interpreted to be a consequence of fluid-rock interaction, which may have brought fluids rich in these elements from the underlying metamorphosed accretionary prism, onto which the Achebuches metabasites were thrust.

Because of the clear variation in major elements within “protoliths” across the length of the shear zone, the presumed localization of the fluid must be reconsidered. Other studies document fluid-rock interaction that is confined into shear bands due to a positive feedback between strain softening, strain localization, and subsequent development of favorable fluid pathways within shear zones (Yonkee et al., 2013). Due to the inconsistent protolith chemistry across the length of the shear zone, it is possible that the fluid did not behave as locally as the

Conduit-Barrier Fluid Flow model suggests but instead reached outer areas of the shear zone through localized fractures. However, fluid interaction near the shear zone boundary did play a role in strain-softening and partial strain localization caused by the interaction and subsequent breakdown of hornblende and plagioclase to produce chlorite and epidote, which are weaker minerals. This fluid infiltration and the associated textural softening and grain-size reduction probably enhanced strain accumulation and may explain why the shear fabrics extend more broadly into the metabasites compared to the PdL. While it is not known whether the fluid promoted shear development or the shear zone provided a more favorable conduit of flow, or whether it was an amalgamation of both, fluid interaction with this shear zone is evident.

## 7. FUTURE WORK

Future work would include extensive geochemical analysis of the Pulo Do Lobo terrane to try and constrain the source of the fluid that moved through the SISZ. The  $K_2O$  enrichment across the shear zone suggests that the metamorphosed accretionary prism (PdL) is a plausible source. If this is true, it is expected that geochemical analysis of the PdL would reveal a depletion of  $K_2O$  as it moved into a fluid that eventually moved through the SISZ.

Because of the complexity of shear zone geochemical characterization, future work should combine this major-element analysis with trace-element analysis and mass-balance calculations to understand the fluid-rock interaction in greater detail (Beinlich et al, 2010). The addition of K, a large-ion-lithophile element (LILE), to our rocks implies an external fluid source and therefore using trace elements would allow identification of other LILE and LREE additions to the system to better constrain the composition and source of the incoming fluid. This may help us understand whether the fluids came from the neighboring PdL terrain. Other studies use trace elements to understand fluid-rock interaction (e.g. You et al., 1996, John et al., 2008, Beinlich et al, 2010).

Mass balance and microprobe analysis allows a quantitative understanding of element mobility during fluid infiltration and metamorphic reactions. By

understanding the chemical composition of the minerals within each domain, it will allow for a better understanding of how the elements are moving within the shear zone and which minerals are incorporating which elements, such as  $K_2O$ . By determining volume loss, we can better understand the feedback system between fluid-rock interaction and element mobility, as volume loss leads to enhanced fluid infiltration (Straaten et al., 2008), which enhances element mobility. Possible volume loss also has implications for prior kinematic analyses (Fernandez et al., 2013) because differential volume loss affects the orientations of strain fabrics that are used to constrain kinematic models.

Other possibilities include isotope and electron-microprobe analysis to understand fluid-rock interaction in greater detail. For example, Losh (1997) uses grain-scale Sr isotopic variations in amphibolites to understand fluid origins and flow behavior of a retrograde fluid, such as composition/source of the external fluid and how many, or few, fluid influxes occurred. Similarly, variations in oxygen isotopes are commonly used to understand mass transfer and unravel the  $P$ - $T$ - $t$ -fluid evolution of the crust (Chamberlain and Conrad, 1993, John et al., 2008).

It would be advantageous to determine whether the fluids moving through the shear zone are meteoric, magmatic, or metamorphic in nature by analyzing fluid inclusions that become trapped during crystal plastic deformation. Fluid inclusions rich in  $CO_2$  represent immiscible fluids associated with metamorphism

whereas saline brines represent immiscible fluids associated with the crystallization of magma (Siebenaller et al., 2012). A meteoric fluid source is distinguished from these two by hydrogen isotope ( $\delta D$ ) values, where meteoritic fluid is characterized by lower  $\delta D$  values between -40 and -46‰ and metamorphic/magmatic fluids are characterized by  $\delta D$  values between -56‰ and -66 ‰ (Siebenaller et al., 2012).

## 8. REFERENCES

- Ault, A.K., Selverstone, J., 2008, Microtextural constraints on the interplay between fluid-rock reactions and deformation. *Contrib. Mineral Petrology*, 156, 501-515.
- Austrheim, H., 1986, Eclogitization of lower crustal granulites by fluid migration through shear zones. *Earth and Planetary Science Letters* 81, 221-232.
- Axen, G., J., 2001, High-temperature embrittlement of extensional Alpine mylonite zones in the midcrustal ductile-brittle transition. *Journal of Geophysical Research* 106, 4337-4348.
- Bard, J. P., 1969, Le metamorphisme regional progressif des Sierras d'Aracena en Andalousie occidentale (Espagne): sa place dans le segment hercynien sud-iberique. Theses, USTL Montpellier. 397p.
- Bard, J.P., Moine, B., 1979, Acebuches amphibolites in the Aracena Hercynian metamorphic belt (southwest Spain): Geochemical variations and basaltic affinities, *Lithos* 12, 271-282.
- Barnes, J. D., Selverstone, J., Sharp, Z. D., 2004, Interactions between serpentine devolatilization, metasomatism and strike-slip strain localization during deep-crustal shearing in the Eastern Alps. *Journal of Metamorphic Geology* 22(4), 283-300.
- Barton, C.A., Zoback, M.D., Moos, D., 1995, Fluid flow along potentially active faults in crystalline rock. *Geology*, 23, 683-686.
- Beach, A., 1976, The interrelations of fluid transport, deformation, geochemistry and heat flow in early Proterozoic shear zones in the Lewisian Complex, *Philos. Trans. R. Soc. London*, 280, 569-604.
- Beach, A., 1980, Retrogressive metamorphic processes in shear zones with special reference to the Lewisian complex. *Journal of Structural Geology*, 2, 257-263.
- Bebout, G.E., and Barton, M.D., 1989, Fluid flow and metasomatism in a subduction zone hydrothermal system: Catalina Schist terrane, California. *Geology*, 17, 976-980.
- Beinlich, A., Klemd, R., John T., Gao, J., 2010, Trace-element mobilization during Ca-metasomatism along a major fluid conduit: Eclogitization of blueschist as a consequence of fluid-rock interaction. *Geochimica et Cosmochimica Acta*, 74, 1982-1992.

- Beitter, T., Wagner, T., Markl, G., 2008, Formation of kyanite-quartz veins of the Alpe Sponda, Central Alps, and Switzerland: implications for Al transport during regional metamorphism. *Contribution to Mineralogy and Petrology*, 156, 689-707.
- Bense, V.F., and Person, M.A., 2006, Faults as conduit-barrier systems to fluid flow in siliciclastic sedimentary aquifers. *Water Resources Research*, 42.
- Boulton, C., Mensies, C.D., Toy, V., G., Townend, J., Sutherland, R., 2016, Geochemical and microstructural evidence for interseismic changes in fault zone permeability and strength, Alpine Fault, New Zealand. *Geochemistry, Geophysics, Geosystems*.
- Byers, H.L., McHenry, L.J., Grundl, T.J., 2016, Forty-nine major and trace element concentrations measured in soil reference materials NIST SRM 2586, 2587, 2709a, 2710a, 2711a using ICP-MS and Wavelength Dispersive XRF. *Geostandards and Geoanalytical Research*.
- Caine, J.S., Evans, J.P., Forster, C.B., 1996, Fault zone architecture and permeability structure. *Geology*, 24, 1025-1028.
- Carter, N.L., Kronenberg, A.K., Ross, J.V., Wiltschko, D.V., 1990, Control of fluids on deformation of rocks. In: Knipe, .R.J., Rutter, E.H. Eds., *Deformation Mechanisms, Rheology and Tectonics*. *Geol. Soc. Spec. Publ.* 54, 1–13.
- Castro, A., Fernández, C., de la Rosa, J. D., Moreno-Ventas, I., Rogers, G., 1996, Significance of MORB-derived amphiboles from the Aracena Metamorphic Belt, southwest Spain, *J. Petrol.* 37, 235–260.
- Castro, A., Fernandez, C., El-Hmidi, H., El-Biad, M., Diaz, M., Rosa, J.D., and Stuart, F., 1999, Age constraints to the relationships between magmatism, metamorphism and tectonism in the Aracena metamorphic belt, southern Spain, *Int.J.EarthSci.* 88, 26–37.
- Chamberlain, C.P., and Conrad, M.E., 1993, Oxygen-isotope zoning in garnet: A record of volatile transport. *Geochimica et Cosmochimica Acta*, 57, 2613-2629.
- Cox, S. F., 2002, Fluid flow in mid- to deep crustal shear systems: Experimental constraints, observations on exhumed high fluid flux shear systems, and implications for seismogenic processes. *Earth Planets Space* 54, 1121-1125.
- Crespo-Blanc, A., and Orozco, M., 1988, The southern Iberian shear zone: A major boundary in the Hercynian folded belt, *Tectonophysics*, 148, 221–227.
- Dahn, D. R. L., Braid, J. A., Murphy, J. B., Quesada, C., Dupuis, N., Mcfarlane, C. R. M., 2014, *Geochemistry of the Peramora Mélange and Pulo*

do Lobo schist: geochemical investigation and tectonic interpretation of mafic mélangé in the Pangean suture zone, Southern Iberia. *Int. J. Earth Sci.* 1415–1431.

- Deer, W.A., Howie, R.A., and Zussman, J., 2013, An introduction to rock forming minerals. The Mineralogical Society.
- Díaz Azpiroz, M., 2000, Evolucion tectono-metamorfica del dominio de alto grado de la banda metamorfica de Aracena. Tesis Doctoral, Univ. Huelva. Publicada en 2006 en: *Lab. Xeol. Laxe, Serie Nova Terra*, 36, 857 pages.
- Díaz Azpiroz, M., Lloyd, G. E., Fernández, C., 2007, Development of lattice preferred orientation in clinoamphiboles deformed under low-pressure metamorphic conditions. A SEM/EBSD study of metabasites from the Aracena metamorphic belt (SW Spain). *Journal of Structural Geology* 29, 629-645.
- Díaz-Azpiroz, M., Fernández, C., 2005, Kinematic analysis of the Southern Iberian shear zone and tectonic evolution of the Acebuches metabasites (SW Variscan Iberian Massif). *Tectonics* 24, TC3010.
- Díaz Azpiroz, M., Fernández, C., Castro, A., El-Biad, M, 2006, Tectonometamorphic evolution of the Aracena metamorphic belt (SW Spain) resulting from ridge-trench interaction during Variscan plate convergence." *Tectonics* 25, TC1001.
- Dupuy, C., Dostal, J., Bard, P., 1979, Trace element geochemistry of Paleozoic amphibolites from S.W. Spain. *Minerology and Petrology*, 29, 87-93.
- Fernández, C., Czeck D., Díaz-Azpiroz, M., 2013, Testing the model of oblique transpression with oblique extrusion in two natural cases: Steps and consequences. *Journal of Structural Geology*, 54, 85-102.
- Ferry, J.M., 1987, Metamorphic hydrology at 13-km depth and 400–500°C. *American Mineralogist*, 72, 39–58.
- Fyfe W. S., Price N. J., Thompson A. B, 1978, *Fluids in the Earth's Crust*. Elsevier, Amsterdam.
- Fyfe, W.S., Kerrich, R., 1985, Fluids and thrusting. *Chemical Geology* 49, 353-362.
- Gale, A., Dalton, C. A., Langmuir, C.H., Yongjun, S., Schilling J., 2013, The mean composition of ocean ridge basalts. *American Geophysical Union*, 14, 489-518.
- Gater, A. E., 1991, Shear zone control on mineral deposits in the State-line serpentinite, Pennsylvania Piedmont. *Ore Geology Reviews* 6.2-3, 171-184.

- Goddard, J.V., and Evans, J.P., 1995, Chemical changes and fluid-rock interaction in faults of crystalline thrust sheets, northwestern Wyoming, U.S.A. *Journal of Structural Geology*, 17, 533-547.
- Grant, J.A., 1986, The isocon diagram; a simple solution to Gresens' equation for metasomatic alteration. *Economic Geology*, 81, 1976-1982.
- Gutiérrez-Alonso, G., Murphy, J. B., Fernández-Suárez, J., Weil, A. B., Franco, M. P., Gonzalo, J. C., 2011, Lithospheric delamination in the core of Pangea: Sm-Nd insights from the Iberian mantle. *Geology* 39(2), 155-158.
- Harlov, D. E., and Austrheim, H., 2013, *Metasomatism and the chemical transformation of rock the role of fluids in terrestrial and extraterrestrial processes*. Heidelberg: Springer.
- Holness, M. B., 1997, *Lithological, Structural, and Deformation Controls on Fluid Flow during Regional Metamorphism. Deformation-Enhanced Fluid Transport in the Earth's Crust and Mantle*, Chapman & Hall, pp. 196–222.
- John, T., Klemd, R., Gao, J., Garbe-Schonberg, C.D., 2008, Trace-element mobilization in slabs due to non-steady-state fluid-rock interaction: Constraints from an eclogite-facies transport vein in blueschist (Tianshan, China). *Lithos*, 103, 1-24.
- Kerrich, R., Allison, I., Barnett, R. L., Moss, S., Starkey, J., 1980, Microstructural and chemical transformations accompanying deformation of granite in a shear zone at Miéville, Switzerland; with implications for stress corrosion cracking and superplastic flow. *Contrib. Mineralogy and Petrology*, 7, 221-242.
- Kisters, F.M.A., Kolb, J., Meyer, F. M., Hoernes, S., 2000, Hydrologic segmentation of high-temperature shear zone: structural, geochemical, and isotope evidence from auriferous mylonites of the Renco mine, Zimbabwe. *Journal of Structural Geology* 22, 811-829.
- Knipe R. J., and Wintsch R. P., 1985, *Heterogeneous Deformation, Foliation Development, and Metamorphic Processes in a Polyphase Mylonite. Metamorphic Reactions. Advances in Physical Geochemistry*, 2, 180-210.
- Kolb, J., Rogers, A., Meyer, F. M., Vennemann, T. W., 2004, Development of fluid conduits in the auriferous shear zones of the Hutti Gold Mine, India: evidence for spatially and temporally heterogeneous fluid flow. *Tectonophysics*, Vol. 378, 65-84.
- Kronenberg, A. K., Kirby, S. H., Pinkston, J., 1990, Basal slip and mechanical anisotropy of biotite. *Journal of Geophysical Research*, 95, 19257-19278.

- Losh, S., 1997, Stable isotope and modeling studies of fluid-rock interaction associated with the Snake Range and Mormon Peak detachment faults, Nevada. *Bulletin of the Geological Society of America*, 109, 300-323.
- Marquer, D., Baudin T., Peucat, J., Persoz, F., 1994, Rb-Sr mica ages in the Alpine shear zones of the Truzzo granite: Timing of the Tertiary alpine P-T-deformations in the Tambo nappe (Central Alps, Switzerland). *Ecology Geology Switzerland*, 87, 225-229.
- Marsh, J.H., Gerbi, C.C., Culshaw, N.G., Potter, J., Longstaffe, F.J., Johnson, S.E., 2011, Initiation and development of the Twelve Mile Bay shear zone: the low viscosity sole of granulite nappe. *Journal of Metamorphic Geology*, 29, 167-191.
- McCaig, A. M., 1984, Fluid interaction in some shear zones from the Pyrenees. *Journal of Metamorphic Geology*, 2, 129-141.
- McCaig, A. M., 1987, Deformation and fluid-rock interaction in metasomatic dilatant shear bands. *Tectonophysics*, 135, 121-132.
- McHenry, L.J., 2009, Element mobility during zeolitic argillic alteration of volcanic ash in a closed-basin lacustrine environment: Case study Olduvai Gorge, Tanzania. *Chemical Geology*, 540-552.
- Micklethwaite, S., Sheldon, H. A., Baker, T., 2010, Active fault and shear processes and their implications for mineral deposit formation and discovery. *Journal of Structural Geology* Vol. 32.2, 151-165.
- Mukherjee, K., and Gupta, P.K., 2008, Arbitrary scaling in ISOCON method for geochemical mass balance: An evaluation of the graphical approach. *Geochemical Journal*, 42, 247-253.
- Newman, J., Mitra, G., 1993, Lateral variations in mylonite zone thickness as influenced by fluid-rock interactions, Linville Falls fault, North Carolina. *Journal of Structural Geology* 15, 849-863.
- O'Hara, K., 1988, Fluid flow and volume loss during mylonitization: an origin for phyllonite in an overthrust setting, North Carolina U.S.A. *Tectonophysics*, 156, 21-36.
- O'Hara, K., and Blackburn, W.H., 1989, Volume-loss model for trace-element enrichments in mylonites. *Geology*, 17, 524-527.
- Onezime, J., Charvet, J., Faure, M., Chauvet, A., Panis, D, 2002, Structural evolution of the southernmost segment of the West European Variscides. The South Portuguese Zone (SW Iberia). *Journal of Structural Geology* 24, 451-468.
- Quilichini, A., Siebenaller, L., Nachlas, W.O., Teyssier, C., Vennemann, T.W., Heizler, M.T., Mulch, A., 2015, Infiltration of meteoric fluids in an extensional detachment shear zone (Kettle dome, WA, USA): How quartz

dynamic recrystallization relates to fluid-rock interaction. *Journal of Structural Geology*, 71, 71-85.

- Ramsay, J.G., Graham, R.H., 1970, Strain variation in shear belts. *Canadian Journal of Earth Science*, 7, 786-813.
- Secor, D. T., 1965, Role of Fluid Pressure in Jointing. *American Journal of Science* 262, 633-646.
- Selverstone, J., Morteani, G, Staude, J. M., 1991, Fluid channeling during ductile shearing: transformation of granodiorite into aluminous schist in the Tauern Window, eastern Alps. *Journal of Metamorphic Geology*, 9, 419–431.
- Sharp, T.G., and Buseck P.R., 1988, Prograde versus retrograde chlorite-amphibole intergrowths in calc-silicate rock. *American Mineralogist*, 73, 1292-1301.
- Sibson, R. H., Robert, F., Poulsen, K. H., 1988, High-angle reverse faults, fluid-pressure cycling, and mesothermal gold-quartz deposits. *Geology* 16(6), 551-555.
- Siebenaller, L., Boiron, M.C., Vanderhaeghe, O., Hibsich, C., Jessell, M.W., Andre-Mayer, A.S., France-Lanord, C., Photiades, A., 2012, Fluid record of rock exhumation across the brittle-ductile transition during formation of a Metamorphic Core Complex (Naxos Island, Cyclades, Greece). *Journal of Metamorphic Geology*, 21, 313-338.
- Sinha, A. K., Heitt, D.A., Rimstidt, D.J., 1986, Fluid interaction and element mobility in the development of ultramylonites. *Geology*, 14, 883-886.
- Straaten, F., Schenk, V., John, T., and Gao, J., 2008, Blueschist-facies rehydration of eclogites (Tian Shan, NW-China): Implications for fluid-rock interaction in the subduction channel. *Chemical Geology*, 255, 195-219.
- Tomkins, A.G., Weinberg, R.F., McFarlane, C.R.M., 2009, Preferential magma extraction from K- and metal-enriched source regions in the crust. *Mineralium Deposita*, 44, 171.
- Vocke, R.D., Hanson, G.N., Grunefelder, M., 1987, Rare earth element mobility in Roffna Gneiss, Switzerland. *Contributions to Mineralogy and Petrology*, 95, 145-154.
- Wawrzyniec, T., Selverstone, J., Axen, G. J., 1999. Correlations between fluid composition and deep-seated structural style in the footwall of the Simplon low-angle normal fault, Switzerland. *Geology* 27(8), 715-718.
- Webb, J.A., and Golding, S.D., 1998, Geochemical mass-balance and oxygen-isotope constraints on Silcrete Formation and its paleoclimatic Implications in Southern Australia. *Journal of Sedimentary Research*, 5, 981-993.

- Whitbread, M.A., and Moore, C.L., 2004, Two lithogeochemical approaches to the identification of alteration patterns at the Elura Zn-Pb-Ag deposit, Cobar, New South Wales, Australia: Use of Pearce Element Ratio Analysis and Isocon Analysis. *Geochemistry: Exploration, Environment, Analysis*, 4, 129-141.
- White, S. H., and Knipe, R. J., 1978, Transformation and reaction enhanced ductility in rocks. *J. Geol. Soc. London* **135**, 513–516.
- White S. H., Burrows, S.E., Carreras J., Humphreys F.J., Shaw, N., 1980, On mylonite in ductile shear zones. *Journal of Structural Geology*, 2, 175-187.
- Wintsch, R. P., Christoffersen, R., Kronenberg, A. K., 1995, Fluid-rock reaction weakening of fault zones. *Journal of Geophysical Research*, 100, 13021-13032.
- Wintsch, R. P., Yi, K., 2002, Dissolution and replacement creep: a significant deformation mechanism in mid-crustal rocks. *Journal of Structural Geology* 24, 1179–1193
- Yonkee, W.A., Parry, W.T., Bruhn, R.I., 2003, Relations between progressive deformation and fluid-rock interaction during shear zone growth in a basement-bored thrust sheet, Sevier Orogenic Belt, Utah. *American Journal of Science*, 303, 1-59.
- Yonkee, W. A., Czeck, D. M., Nachbor, A. C., Barszewski, C., Pantone, S., Balgord, E. A., & Johnson, K. R., 2013, Strain accumulation and fluid-rock interaction in a naturally deformed diamictite, Willard thrust system, Utah (USA): Implications for crustal rheology and strain softening. *Journal of Structural Geology* 50, 91–118.
- You, C.F., Castillo, P.R., Gieskes, J.M., Chan, L.H., Spivack, A.J., 1996, Trace element behavior in hydrothermal experiments: Implications for fluid processes at shallow depths in subduction zones. *Earth and Planetary Science Letters*, 140, 41-52.

## **APPENDICES**

Appendix 1: Geochemistry tables

T1	Distance from top of structure (m)	Domain	SiO <sub>2</sub> (wt. %)	TiO <sub>2</sub> (wt. %)	Al <sub>2</sub> O <sub>3</sub> (wt. %)	Fe <sub>2</sub> O <sub>3</sub> (wt. %)	MnO (wt. %)	MgO (wt. %)	CaO (wt. %)	Na <sub>2</sub> O (wt. %)	K <sub>2</sub> O (wt. %)	P <sub>2</sub> O <sub>5</sub> (wt. %)	LOI (wt. %)	Total (wt. %)
SI08	15.3	Banded amp. CPX	49.58	1.67	15.34	10.55	0.19	7.02	10.34	3.44	0.32	0.20	1.18	100.02
SI31	158.4	Banded amp. w/o CPX	49.30	1.65	15.25	10.89	0.20	6.66	11.48	2.88	0.16	0.19	0.81	99.58
SI32A	189.1	Banded amp. w/o CPX	50.96	2.11	14.29	12.08	0.16	6.10	9.61	3.80	0.09	0.29	0.49	100.07
SI32B	192	N/A	57.16	2.02	15.09	10.16	0.14	3.05	5.62	5.67	0.12	0.76	0.52	100.16
SI09	206.9	Banded amp. w/o CPX	49.10	1.29	15.69	10.23	0.19	8.71	10.79	2.39	0.11	0.14	0.78	99.54
SI10	221.1	Sheared amphibolite	49.09	1.67	15.32	10.83	0.16	6.62	11.72	2.51	0.17	0.23	0.77	99.24
SI33a	282.3	Sheared amphibolite	50.27	1.89	15.35	11.21	0.16	4.91	9.66	4.40	0.29	0.22	0.48	98.98
SI33b1	301.2	Mafic chlorite schist	49.26	1.81	16.04	10.77	0.18	5.93	10.58	3.64	0.37	0.22	0.70	99.65
SI33c	320.9	Mafic chlorite schist	48.93	1.23	16.50	9.00	0.15	8.30	11.07	2.97	0.12	0.12	0.98	99.46
SI33d	337.8	Mafic chlorite schist	47.09	1.21	17.21	8.12	0.13	5.55	10.75	2.95	0.39	0.16	1.19	94.88
SI33e	373.4	Mafic chlorite schist	50.47	1.16	17.52	8.49	0.13	5.25	12.49	3.36	0.38	0.16	0.86	100.41
SI11	378.8	Mafic chlorite schist	50.96	1.16	17.07	8.51	0.12	6.10	10.30	3.81	0.21	0.16	2.00	100.51
SI33f	390.2	Mafic chlorite schist	49.33	1.19	17.22	8.55	0.13	5.56	12.66	2.93	0.52	0.17	0.80	99.19
SI35	450.2	Mafic chlorite schist	48.41	1.13	16.45	9.32	0.15	8.19	12.85	2.46	0.11	0.10	1.12	100.41
SI12	508.4	Mafic chlorite schist	46.21	1.13	18.61	9.31	0.13	8.98	9.54	1.48	0.12	0.10	4.50	100.22

T2	Distance from top of structure (m)	Domain	SiO <sub>2</sub> (wt. %)	TiO <sub>2</sub> (wt. %)	Al <sub>2</sub> O <sub>3</sub> (wt. %)	Fe <sub>2</sub> O <sub>3</sub> (wt. %)	MnO (wt. %)	MgO (wt. %)	CaO (wt. %)	Na <sub>2</sub> O (wt. %)	K <sub>2</sub> O (wt. %)	P <sub>2</sub> O <sub>5</sub> (wt. %)	LOI (wt. %)	Total (wt. %)
SI15a	25.9	Banded amp. CPX	48.23	1.75	14.12	13.53	0.12	7.31	10.95	2.57	0.09	0.16	0.83	99.71
SI15b	30.0	Banded amp. CPX	50.25	1.50	14.46	10.17	0.14	7.71	11.57	2.83	0.13	0.16	0.66	99.78
SI16a	78.1	Banded amp. w/o CPX	50.02	1.69	14.88	11.06	0.18	7.05	9.51	3.89	0.09	0.22	0.69	99.40
SI20a	82.9	Banded amp. w/o CPX	48.78	1.60	14.75	11.86	0.15	7.85	11.10	2.66	0.10	0.20	0.73	99.90
SI20b	86.7	Banded amp. w/o CPX	51.38	1.31	15.41	10.09	0.18	6.77	9.94	3.26	0.12	0.28	0.93	99.81
SI21a	103.5	Banded amp. w/o CPX	51.04	1.53	14.14	11.22	0.17	7.22	9.35	4.10	0.24	0.18	0.52	99.82
SI21b	111.1	Banded amp. w/o CPX	52.39	2.74	14.61	11.76	0.18	3.91	7.44	4.92	0.26	0.45	0.69	99.50
SI21c	129.3	Banded amp. w/o CPX	48.49	1.69	15.04	11.07	0.17	7.18	10.34	3.00	0.70	0.15	1.85	99.80
SI21d	138.2	sheared amphibolite	49.26	1.19	15.59	10.03	0.16	7.50	11.35	2.77	0.29	0.16	1.28	99.69
SI22	159.5	sheared amphibolite	53.13	1.28	15.78	9.08	0.13	4.90	9.06	4.75	0.57	0.18	0.80	99.77
SI23	177.3	sheared amphibolite	49.03	1.57	15.05	10.26	0.16	7.53	11.32	3.01	0.69	0.16	1.06	99.98
SI24	192.8	Mafic chlorite schist	50.53	1.16	16.47	8.83	0.21	5.54	12.22	3.42	0.49	0.16	0.86	100.03
SI17b	229.1	Mafic chlorite schist	48.65	1.19	16.58	8.96	0.15	8.01	11.60	2.69	0.11	0.10	2.81	100.96
SI17c	240.5	Mafic chlorite schist	48.39	1.34	14.06	10.70	0.17	8.92	11.17	2.39	0.20	0.10	3.36	100.90
SI17d	254.0	Mafic chlorite schist	47.84	1.32	16.14	9.09	0.16	8.60	12.42	2.32	0.13	0.13	2.76	101.01
SI25	254.0	sheared amphibolite	49.62	1.13	18.80	7.62	0.12	6.43	9.68	2.93	0.64	0.18	3.79	101.08
SI18	282.5	sheared amphibolite	48.77	1.23	14.30	10.77	0.17	8.98	11.57	2.20	0.17	0.08	1.35	99.70
SI26	312.8	Mafic chlorite schist	48.87	1.48	18.04	9.10	0.16	4.74	11.73	3.15	0.48	0.18	1.59	99.63
SI27	318.3	Mafic chlorite schist	49.32	1.46	14.13	11.11	0.18	6.98	11.69	3.06	0.24	0.14	1.54	99.96
SI28	326.2	Mafic chlorite schist	49.89	1.01	16.26	8.97	0.14	7.26	10.86	3.03	0.41	0.09	1.33	99.39

T3	Distance from top of structure (m)	Domain	SiO <sub>2</sub> (wt. %)	TiO <sub>2</sub> (wt. %)	Al <sub>2</sub> O <sub>3</sub> (wt. %)	Fe <sub>2</sub> O <sub>3</sub> (wt. %)	MnO (wt. %)	MgO (wt. %)	CaO (wt. %)	Na <sub>2</sub> O (wt. %)	K <sub>2</sub> O (wt. %)	P <sub>2</sub> O <sub>5</sub> (wt. %)	LOI (wt. %)	Total (wt. %)
SI72	0	Banded amp. CPX	47.64	1.64	14.25	10.22	0.18	6.36	8.87	3.32	0.69	0.18	2.02	95.50
SI66	77.6	Banded amp. w/o CPX	49.35	2.14	15.21	10.99	0.22	6.51	9.34	3.55	0.08	0.29	0.77	98.59
SI67	94.6	Banded amp. w/o CPX	50.42	1.57	15.15	9.44	0.22	7.32	9.39	3.75	0.07	0.19	0.77	98.41
SI68	135.0	Banded amp. w/o CPX	49.13	2.16	14.58	13.14	0.16	5.65	7.38	4.56	0.24	0.40	0.94	98.47
SI69	205.7	Banded amp. w/o CPX	48.44	1.33	15.49	10.16	0.26	8.43	9.62	2.82	0.54	0.16	2.04	99.40
SI70	308.0	sheared amphibolite	50.30	1.51	15.59	9.66	0.24	7.55	7.84	4.09	0.10	0.23	1.02	98.24
SI71	434.4	sheared amphibolite	49.25	2.16	14.57	12.09	0.18	5.10	10.34	3.79	0.40	0.26	0.76	99.05
SI65	549.7	Mafic chlorite schist	47.69	2.02	14.79	12.60	0.19	5.49	11.91	2.85	0.17	0.22	1.60	100.06
SI64	607.0	Mafic chlorite schist	46.74	0.93	16.92	9.00	0.21	6.14	15.11	1.45	0.67	0.07	2.58	99.97
SI63	623.1	Mafic chlorite schist	47.85	2.85	13.42	14.28	0.31	6.02	9.14	3.24	0.45	0.34	1.41	99.49
SI62	652.2	Mafic chlorite schist	50.33	1.79	15.46	10.80	0.28	6.47	6.31	4.63	0.50	0.23	2.59	99.51
SI61	664.8	sheared amphibolite	47.24	1.26	17.75	8.81	0.14	6.57	11.12	2.86	0.19	0.12	1.39	97.56
SI60	682.6	Mafic chlorite schist	48.55	2.22	14.15	13.24	0.25	5.60	9.19	4.05	0.35	0.25	2.88	100.88
SI59	710.2	Mafic chlorite schist	49.08	1.67	15.12	11.06	0.18	7.00	11.25	3.12	0.24	0.15	1.14	100.12
SI58	712.4	Mafic chlorite schist	48.21	1.63	16.28	10.19	0.17	6.13	10.83	3.17	0.46	0.15	1.73	99.07
SI43	726.0	Mafic chlorite schist	47.54	1.22	15.79	9.60	0.20	7.47	11.71	2.67	0.46	0.11	2.08	98.98
SI42	746.1	Mafic chlorite schist	47.92	1.12	14.97	9.61	0.17	9.68	10.52	2.36	0.57	0.09	2.38	99.52

T5	Distance from top of structure (m)	Domain	SiO <sub>2</sub> (wt. %)	TiO <sub>2</sub> (wt. %)	Al <sub>2</sub> O <sub>3</sub> (wt. %)	Fe <sub>2</sub> O <sub>3</sub> (wt. %)	MnO (wt. %)	MgO (wt. %)	CaO (wt. %)	Na <sub>2</sub> O (wt. %)	K <sub>2</sub> O (wt. %)	P <sub>2</sub> O <sub>5</sub> (wt. %)	LOI (wt. %)	Total (wt. %)
SI40	75.6	Banded amp. w/o CPX	48.89	2.10	15.38	12.25	0.19	7.62	9.96	2.95	0.31	0.30	1.36	101.45
SI39	172	sheared amphibolite	49.66	1.38	13.90	9.82	0.23	6.02	11.39	3.36	0.39	0.19	0.79	97.25
SI36	274.1	sheared amphibolite	50.79	1.53	14.64	10.85	0.17	6.59	9.94	4.01	0.14	0.18	0.81	99.48
SI38	275.7	sheared amphibolite	50.86	1.72	15.00	10.72	0.16	5.75	9.33	4.60	0.14	0.23	0.85	99.77
T6	Distance from top of structure (m)	Domain	SiO <sub>2</sub> (wt. %)	TiO <sub>2</sub> (wt. %)	Al <sub>2</sub> O <sub>3</sub> (wt. %)	Fe <sub>2</sub> O <sub>3</sub> (wt. %)	MnO (wt. %)	MgO (wt. %)	CaO (wt. %)	Na <sub>2</sub> O (wt. %)	K <sub>2</sub> O (wt. %)	P <sub>2</sub> O <sub>5</sub> (wt. %)	LOI (wt. %)	Total (wt. %)
SI80	5	Banded amp. CPX	50.86	0.92	14.68	7.86	0.16	7.84	11.53	2.56	1.14	0.08	2.12	99.90
SI79	134.68	sheared amphibolite	48.54	1.94	14.95	12.06	0.41	7.58	7.57	3.66	0.61	0.25	1.94	99.66
SI81	306.15	sheared amphibolite	48.68	2.14	14.91	11.84	0.19	6.44	10.50	2.67	0.64	0.26	1.55	99.96
SI78	459.38	Mafic chlorite schist	47.36	1.10	18.76	8.04	0.13	6.01	14.94	2.47	0.32	0.13	0.94	100.30
SI73	498.4	Mafic chlorite schist	47.44	2.00	14.13	12.53	0.22	6.41	12.28	2.32	0.26	0.21	1.97	99.89
SI75	554.37	Mafic chlorite schist	46.99	1.60	15.16	11.65	0.19	6.27	12.62	2.20	0.17	0.16	2.15	99.30

T8	Distance from top of structure (m)	Domain	SiO <sub>2</sub> (wt. %)	TiO <sub>2</sub> (wt. %)	Al <sub>2</sub> O <sub>3</sub> (wt. %)	Fe <sub>2</sub> O <sub>3</sub> (wt. %)	MnO (wt. %)	MgO (wt. %)	CaO (wt. %)	Na <sub>2</sub> O (wt. %)	K <sub>2</sub> O (wt. %)	P <sub>2</sub> O <sub>5</sub> (wt. %)	LOI (wt. %)	Total (wt. %)
S157	57.11	Banded amp. CPX	46.31	2.13	14.04	12.72	0.20	6.29	10.20	2.91	0.12	0.25	0.95	96.24
S156	140.17	Banded amp. w/o CPX	51.40	1.96	13.96	11.73	0.16	5.77	8.58	4.07	0.78	0.27	1.45	100.27
S155	507.72	sheared amphibolite	49.83	1.93	14.29	11.73	0.20	7.25	9.76	3.12	0.26	0.19	2.22	100.94
S154	588.72	sheared amphibolite	48.22	1.28	16.68	9.18	0.15	9.41	10.75	2.32	0.39	0.12	2.22	100.83
S151	1006.59	sheared amphibolite	50.09	1.62	15.24	10.88	0.16	7.40	11.00	2.72	0.28	0.16	1.47	101.15
S150	1389.35	Mafic chlorite schist	49.99	1.60	14.98	10.66	0.18	7.23	12.01	2.43	0.15	0.14	1.48	100.98
S149b	1641.95	Mafic chlorite schist	49.59	1.66	14.30	11.47	0.17	7.31	11.87	2.62	0.16	0.16	1.96	101.40
S149a	1641.95	Mafic chlorite schist	49.83	1.50	14.78	11.11	0.19	7.31	11.16	2.97	0.14	0.14	1.53	100.81
S148	1710.56	Mafic chlorite schist	48.64	1.41	14.90	10.93	0.19	6.84	13.62	2.37	0.20	0.16	1.44	100.83
S147	1764.4	Mafic chlorite schist	48.74	1.60	15.30	11.67	0.18	7.50	10.77	2.65	0.15	0.19	2.03	100.91
S146	1825.7	Mafic chlorite schist	49.69	1.81	15.00	12.13	0.17	5.78	11.47	3.11	0.22	0.22	1.49	101.23
S145b	2052.66	Mafic chlorite schist	49.00	1.95	13.49	12.90	0.18	8.68	9.77	2.87	0.25	0.17	1.35	100.75
S145a	2149.01	Mafic chlorite schist	48.82	1.64	15.50	11.55	0.17	6.93	11.97	2.73	0.20	0.16	1.67	101.45